Title
Bubble Coalescence Dynamics and Supersaturation in Electrolytic Gas Evolution

Author
Stover, R.

Publication Date
1996-08-01

LBNL-39258
UC-1501

ERNEST ORLANDO LAWRENCE
BERKELEY NATIONAL LABORATORY

Bubble Coalescence Dynamics and Supersaturation in Electrolytic Gas Evolution

R.L. Stover
Energy and Environment Division

August 1996
Ph.D. Thesis

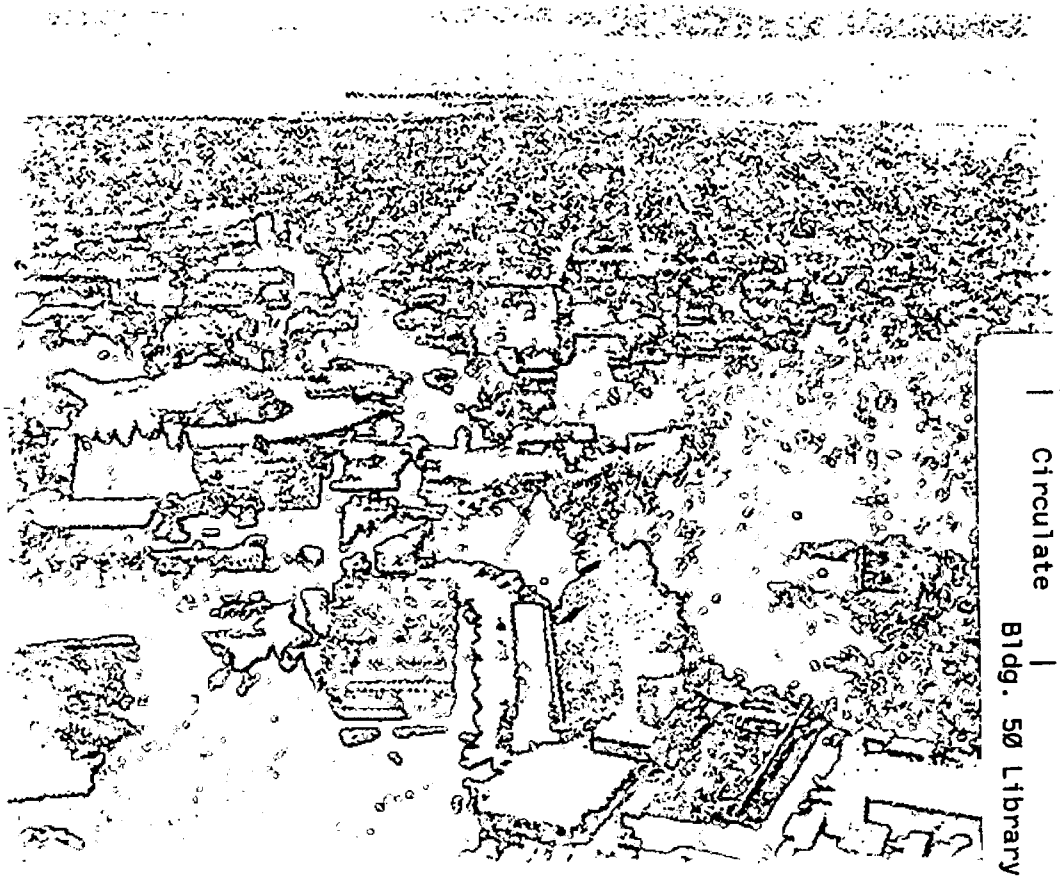

DISCLAIMER

LBNL-39258
UC-1501

BUBBLE COALESCENCE DYNAMICS AND SUPERSATURATION IN ELECTROLYTIC GAS EVOLUTION

by

Richard L. Stover
Ph.D. Thesis

Department of Chemical Engineering
University of California

and

Energy & Environment Division
Lawrence Berkeley National Laboratory
Berkeley, California 94720

August 1996

This work was supported by the Assistant Secretary for Energy Efficiency and Renewable Energy, Office of Transportation Technologies, Office of Advanced Automotive Technologies of the U.S. Department of Energy under Contract No. DE-AC03-76SF00098.

Abstract

Bubble Coalescence Dynamics and Supersaturation in Electrolytic Gas Evolution

by

Richard Lindsay Stover

Doctor of Philosophy in Chemical Engineering

University of California, Berkeley

Professor Morton M. Denn, Chair

1. Bubble coalescence on gas-evolving electrodes disturbs the fluid immediately adjacent to the surface, thereby significantly impacting mass transport to and from the electrode. Previous efforts to quantify coalescence phenomena have not been successful despite the application of high speed cinematography (up to 10^4 frames/s) because of the extremely short duration (< 1 ms) of such events. To overcome this difficulty, a new technique was developed to study the interfacial velocities and shape changes associated with the coalescence of two electrolytically generated bubbles, 50 to 600 micron in diameter. The optical technique devised and used here employs a linear photodiode array to detect bubble movement with a resolution of 10^{-6} s. The apparatus and procedures developed in this research permit the observation and measurement of electrolytic bubble

coalescence.

When two bubbles coalesce, the surface energy that is released produces interface velocities of 200 to 400 cm/s. The initial velocity of the interface is approximately proportional to the square root of the surface tension and inversely proportional to the square root of the bubble radius. Following the initial motion, large amplitude oblate-prolate oscillations occur at frequencies of 0.4 to 17 kHz. The period of the oscillations varies with the bubble radius raised to the 3/2 power and inversely with the square root of the surface tension. Viscous resistance to shear motion in the surrounding fluid dampens the oscillations in 0.3 to 10 ms. The rate of damping is proportional to the viscosity and inversely proportional to the square of the bubble radius.

2. Finite-element solutions of the free-surface, nonlinear Navier-Stokes equations are consistent with most of the experimental results. The differences between the computed and measured saddle point decelerations and periods suggest that the surface tension decreases during each experimental run. The surface tension did not change to as significant a degree during the experiments on larger bubbles. The simulations did not fully explain the experimental results for the initial velocity which indicates the complexity of the rupture of the liquid film. A more focussed analysis should be done to elucidate the phenomena that occur in the receding liquid film immediately following rupture. Both the simulations and the experiments showed that surface waves were superimposed on the initial and oscillatory motion of the bubbles. These small-amplitude motions locally reduce the surface energy during a coalescence event.

3. The accumulation of dissolved gas in the electrolyte adjacent to an electrode creates a concentration overpotential that lowers the energy efficiency of the electrochemical system. The concentrations of dissolved gas in aqueous electrolytes can exceed saturation even at low production rates because the diffusivity and solubility of the dissolved gas are low (about $10^{-5}cm^2/s$ and $10^{-7}mol/cm^3$, respectively). In this research, the dependence of gas supersaturation on current density is determined under conditions approaching zero convection and with a low density of bubble nucleation sites. These conditions minimize hydrodynamic and bubble nucleation variables and provide high degrees of supersaturation.

Supersaturations ranged from relative activities of 26 to 178, proportional to the square root of the applied current densities in the range of 0.4 to 72 mA/cm^2. The supersaturation values were consistently higher than those at a coarse electrode (rough surface) or at a vertically oriented non-recessed electrode. These results indicate that bubble nucleation and mass transfer in the bulk electrolyte are restricted by the electrode texture, orientation, and geometry. Even a highly polished surface provides sites for bubble nucleation that lower gas supersaturation. A simulation obtained by a model developed in this research showed that bubble departure does not reduce the dissolved gas concentration at an electrode surface to the extent assumed in the surface renewal model of Ibl. A proposed partial renewal model, which reflects the replacement of departing bubbles with supersaturated electrolyte, fits the experimental results.

Contents

Acknowledgments

It has been an honor and privilege to have been advised by the late Professor Charles Tobias throughout most of this work. Tobias taught in a way that made learning an ongoing, self-motivated process. The wisdom that he shared with me continues to have profound effects on me as a chemical engineer and as a person. Tobias is, in his words, my complete advisor.

Professor Denn has been involved in this work from the beginning. I have benefitted from and enjoyed his participation greatly. I thank Dr. Kinoshita for his input on cell design and Dr. Muller for his excellent advice on the optical design. Dr. Egan got this project off the ground before I arrived making it possible for me to get as far with it as I did in the time I had. Henry Chan built and later modified the photodetector. Robert Abbassi did nearly all the surface tension and viscosity tests that make up Appendix ID.

Gerd Matzen has been a fantastic labmate, easy going and always willing to listen or help. It was because of his encouragement that I initially considered taking up this project. I would also like to acknowledge the support of my classmates, especially Keith Karraker, Blaine Paxton, Doug Eames, Mark (the musician) Yanke, Marc (the engineer) Doyle, Bob Villwock, and Ben Rush. We survived, evolved, and grew together.

Major parts of my graduate education have occurred outside of Gilman Hall. Professor Richard Norgaard of Energy and Resources Group, Rabbi Steven Chester, and Rabbi Michael Lerner helped me gain a perspective on science and modern thinking. It is a perspective that does not deny the ecological insanity and the loss of community and

caring of our times. I have come to understand that the problems of this era are deeply rooted in the particular philosophies we have adopted, in the way we use science, in our economics, and in our "common sense". I have embraced the belief that things do not have to be the way they are. There is hope if we can learn to acknowledge and respect the sensitivity, mystery, and holiness of the world and all living beings, care for each other, and build family and community.

Finally, I am proud to acknowledge Isabel who has helped make me the happiest person I know. Because of her, I have realized that the way to balance chemical engineering and environmentalism, intellect and intuition, and security and liberation, is to let go and just be. This dissertation is dedicated to her.

This work was supported by the Assistant Secretary for Energy Efficiency and Renewable Energy, Office of Transportation Technologies, Office of Advanced Automotive Technologies of the U.S. Department of Energy under Contract No. DE-AC03-76SF00098.

PART 1. ELECTROLYTIC BUBBLE COALESCENCE DYNAMICS

Chapter 1. INTRODUCTION

A. Overview

Electrolytic gas evolution occurs in nearly all electrochemical synthesis processes as well as in the corrosion of metals in aqueous electrolyte. Chlorine gas, used to make (poly)vinyl chloride and many other compounds, is produced electrolytically. Carbon dioxide is evolved as the co-product in aluminum production. Hydrogen and oxygen can also be produced electrolytically and are often unwanted side products in rechargeable batteries.

The presence and coalescence of gas bubbles affects fluid motion, mass transfer, overpotential behavior, and ohmic resistance in electrochemical systems. Bubble motion and coalescence are important in other chemical engineering processes as well, such as absorption, flotation and boiling, for example. In addition to providing information useful for engineering design of processes for these applications, the study of bubble coalescence can provide insights into the properties of the liquid-gas interface.

Prior work has addressed the liquid film that thins between two approaching bubbles[1-11], interfacial motion after liquid film rupture by applying analytical treatments[12-17], and the qualitative impact of bubble coalescence on macroscopic fluid motion and mass transfer[18-22]. Efforts to observe and quantify coalescence phenomena in electrolytic systems have not been successful, despite the application of high-speed cinematography (up to 10^4 frames/s) because of the extremely short duration (millisecond range) of such events[23] and

the small size of the gas bubbles (20 to 1000 μm diameter). By using a novel experimental technique, Egan and Tobias[24] were able to observe interfacial motion during bubble coalescence at sampling rates of up to 10^6 samples/s. They achieved these rates by observing motion in only one dimension using a linear photodiode array with a digital output and self-triggering capability. However, their results were limited to bubble diameters greater than 500 μm by optical resolution and detector sensitivity.

In the present study, the experimental method established by Egan and Tobias has been refined and used to quantify the interfacial velocities and shape changes associated with the coalescence of electrolytic gas bubbles. Equal-size pairs of H_2-H_2, H_2-O_2 or O_2-O_2 bubbles (50- to 600-μm diameter) are generated on the tips of aligned, opposing platinum microelectrodes. The position of the interface formed between two coalescing bubbles is recorded as a function of time. Bubble size, electrolyte viscosity and surface tension are varied independently. The results are in agreement with a physical model that involves a full description of the interface shape. The accomplishments of this research include the development of an apparatus capable of accurate, high-speed measurement of a bubble-coalescence event, the quantitative observation of the interface velocities and shape changes that constitute coalescence, and the determination of how coalescence behavior depends on system properties.

B. Prior Work

Investigations of interfacial forces and dynamics have revealed mechanisms important to thin-liquid-film stability and rupture. The results have been applied to bubble

coalescence research to elucidate the likelihood that a given contact will result in coalescence, to understand the mechanism by which the liquid film between two bubbles becomes thinner, and to characterize the fluid motion and the resulting mass transfer rates in the vicinity of coalescing bubbles.

Liquid film thinning and rupture - Bubbles can come close enough together to coalesce by growing into each other on an electrode surface or by being forced together by the motion of the surrounding liquid. For the latter, external body forces, rate of approach, and type and degree of surface deformation are key issues. The work of Chi and Leal[1], for example, focuses on the hydrodynamics of approach and the conditions under which the interfaces form the dimpled structure frequently seen experimentally in the study of coalescing drops.

Marrucci and co-workers[2,3] postulated that the rest time preceding the coalescence of gas bubbles in aqueous solutions depended on the concentration and nature of species in the film and the solution. The mechanism they proposed to corroborate their experimental results consisted of two parts. The first was a very rapid stretching of the film between the bubbles that resulted in a film concentration that differed from the bulk solution concentration. The thickness of the film was calculated based on the balance of electrostatic and van der Waal's forces between the bubbles. Below a limiting value of a dimensionless concentration parameter, and generally for very dilute solutions, the quasi-equilibrium film did not exist and coalescence was instantaneous. The second part was the relatively slow thinning of the quasi-equilibrium film. Diffusion at the border of the film

controlled the thinning rate.

Further experimental studies of the stability of thin aqueous films formed between bubbles as a function of solution composition were conducted by Lessard and Zieminski[4], Sagert and Quinn[5], Oolman and Blanch[6], Prince and Blanch[7], and Craig, Ninham and Pashley[8]. In these studies, pairs of bubbles generated on adjacent nozzles either coalesced or detached without coalescing. Based on the observation of multiple events, the coalescence probability was determined. These researchers found that the likelihood of coalescence depended on the type and concentration of surface active species and salts. Surface active species lowered the coalescence probability by creating a disjoining pressure between the bubble surfaces and/or by stabilizing the interfaces. Most electrolytes screened electrostatic repulsion and thereby reduced the disjoining pressure, but high concentrations of certain salts reduced the probability of coalescence through a mechanism that is unexplained.

The instability and rupture of the thin film between two bubbles acts as the termination point for the film thinning process. Linear[9] and nonlinear[10] stability theories have been proposed to describe the breakdown of thin films. The experiments and analyses such as those described by DeVries[11] are important for fundamental studies of planar films and foams. Once the film becomes unstable, the times for instability growth are typically so short relative to thinning times that rupture is frequently considered to be instantaneous.

Analytical coalescence studies - Dupré[12] considered the growth of a hole in the

film and postulated that the kinetic energy of the receding film could be equated to the surface energy of the film just before rupture. Culick[13] derived an alternative formula based on conservation of momentum that differed from the result of Dupré by a smaller numerical coefficient but indicated the same dependence of hole expansion velocity on surface tension, liquid density, and initial film thickness. An experimental study of the bursting of foam films by McEntee and Mysels[14] recorded lower velocities than those predicted by Culick. They observed the formation of a rim at the edge of the hole and attributed the departure from the predicted velocity to the gas-phase resistance to the motion of the rim. The results obtained by McEntee and Mysels were in good agreement with an empirical equation that considered the density and viscosity of the gas.

For bubble coalescence, the results for planar films are only useful over a small initial part of the interfacial motion because the remainder of the event is not well described by planar analysis. Charles and Mason[15] developed an extension of the hole expansion theory by Dupré for bubble coalescence by assuming that the liquid film recedes along parabolic trajectories. Charles and Mason ignored acceleration of the interface from its initially static configuration, viscous forces in the surrounding fluid, and the dependence of the shape of the interface on the dynamics of coalescence. However, their theory did corroborate the observed velocity decay as the hole opened.

A full description of the free surface shape of an oscillating inviscid liquid drop was provided by Patzek, Brenner, Basaran, and Scriven[16] that included drop shapes, pressure distributions, particle paths, and evolution with time of kinetic and surface energies. Their results were compared to the predictions of linear and second-order

perturbation theories. Basaran[17] later considered the role of the viscosity in an oscillating liquid drop and showed that damping during the first oscillation period increased as the initial drop deformation increased. Thereafter, the damping rate decreased and was time-independent.

Impact of coalescence - After the liquid film ruptures, the surface energy of the newly formed bubble decreases with the reduction in the curvature and surface area, and the energy is imparted to the surrounding liquid as motion and eventually heat. When bubbles coalesce on or near an electrode surface, fresh electrolyte flows to the electrode from the bulk. This stirring increases mass transfer to (or from) the surface.

Putt[18] demonstrated that the coalescence of adjacent bubbles was an important mechanism for bubble growth on electrode surfaces by employing a special time-lapse photographic technique. He concluded that the size of the bubbles on the surface and their number density were related because of coalescence. When the bubbles grew to a close-packed arrangement, coalescence between bubbles took place, resulting in fewer but larger bubbles. He also showed that the coalescence of rising bubbles in the turbulent stream well above the site of generation could be considerable. The degree of coalescence in an electrolyte was primarily a function of the gas generation rate, as related to the velocity field in the electrolyte.

Sides and Tobias[19] identified different types of coalescence using high-speed cinematography. The first type of coalescence involved small bubbles which were in contact with the electrode surface. The small bubbles appeared to touch and immediately

coalesce in much less than 100 μs. In the second mode of coalescence, bubbles of medium size, about 40 μm in diameter, established themselves as central collectors and received the smaller bubbles that were nucleating and growing around them. The radial movement of bubbles was symmetric 360° around the stationary collector bubble. In the third mode of coalescence, large bubbles (>100 μm) slid along the electrode and scavenged smaller bubbles in their path.

Janssen and Hoogland[20] measured the thickness, δ, of the mass-transfer boundary layer at a gas evolving electrode as a function of applied current density, i. For oxygen evolved in 1M KOH, they found a sharp change in the slope of plots for log δ versus log i, with a higher slope (greater mass transfer) obtained at >30 mA/cm^2. They correlated the deviation with the onset of frequent bubble coalescence on the electrode surface at current densities >30 mA/cm^2. In their photographic studies[21], they observed that bubbles formed by coalescence vibrated very strongly and jumped away from the electrode surface.

Dees[22] used a segmented electrode to measure the local mass-transfer enhancement caused by a single bubble coalescence event. Increases in the mass-transfer rate of more than an order of magnitude over the free convection mass-transfer rate were observed because coalescence mixed the surrounding electrolyte.

Bubble coalescence transients - The nature of the events immediately preceding bubble coalescence and the importance of coalescence in electrolytic and other processes has been established as shown in the preceding review of prior work. However, the interfacial velocities and shape changes that comprise coalescence events have been

difficult to quantify. Sides and Tobias[23] attempted to observe bubble coalescence by cinematography at 10,000 frames/s. Two 200-μm diameter bubbles appeared to touch for a duration of time that included many photographic frames as the liquid between them thinned and finally ruptured. The bubbles coalesced so quickly that the film rupture and the change from two bubbles to one occurred in a time much less than the recording of two frames, that is, in less than 100 μs. The new bubble was compressed along the axis of coalescence by the fluid rushing into the space behind the coalescing bubbles. The new bubble went through a series of oblate/prolate-spheroidal oscillations for several frames before becoming spherical.

The first successful experimental measurement of the interfacial velocities during the coalescence of gas bubbles was presented by Egan and Tobias[24]. Measurements of the initial motion of the interface formed by two coalescing electrolytically generated hydrogen bubbles (500- to 1000-μm diameter) showed that the position of the interface along the coalescence plane varied with the square-root of time, in agreement with the model of Charles and Mason[25]. However, the magnitudes of the velocities were substantially lower than the predicted values. The results of Egan and Tobias were restricted to bubble diameters greater than 500 μm because of optical resolution and detector sensitivity limitations. Based on the velocities they measured, the authors concluded that coalescence on an electrode surface enhances local mixing and disturbs the surface boundary layer of electrodes. In addition, the induced fluid motion would likely propel the coalesced bubble pair away from the electrode surface and increase the likelihood that nearby bubbles are dislodged from the surface, creating further mixing and

boundary-layer disturbances.

In the present study, the experimental method established by Egan and Tobias was improved to quantify the interfacial velocities and shape changes associated with the coalescence of electrolytic bubbles of equal size. The phenomena studied include the initial motion of the interface formed by two gas bubbles and the oblate/prolate spheroidal oscillations that follow. The results are corroborated with a physical model that includes a full description of the interface shape.

References

1. Chi, B.K. and Leal, L.G., J. Fluid Mech., **201**, 123 (1989).
2. Marrucci, G., Nicodemo, L. and Acierno, D., International Symposium on Research in Co-current Gas-Liquid Flow, Waterloo, Canada 1968.
3. Marrucci, G., Chem. Eng. Sci., **24**, 975 (1969).
4. Lessard, R.R. and Zieminski, S.A., Ind. Eng. Chem. Fundam., **10**, 260 (1971).
5. Sagert, N.H. and Quinn, M.J., Chem. Eng. Sci., **33**, 1087 (1978).
6. Oolman, T.O. and Blanch, H.W., Chem. Eng. Commun., **43**, 237 (1986).
7. Prince, M.J. and Blanch, H.W., A.I.C.H.E. Journal, **36**, 1425 (1990).
8. Craig, V.S.J., Ninham B.W., and Pashley, R.M., J. Phys. Chem., **97**, 10192 (1993).
9. Chen, J.-D., J. Coll. Interface Sci., **98**, 329 (1984).
10. Prevost, M. and Gallez, D., J. Chem. Phys., **84**, 4043 (1986).
11. DeVries, A.J., Recueil, 77, 383 (1958).
12. Dupré, A., Ann. Chim. Phys., 14, 194 (1864).
13. Culick, F.E.C., J. Appl. Phys., **31**, 1128 (1960).

14. McEntee, W.R. and Mysels, K.J., J. Phys. Chem., **73**, 3018 (1969).

15. Charles, G.E. and Mason, S.G., J. Coll. Sci., **15**, 236 (1960).

16. Patzek, T.W., Brenner, R.E., Jr., Basaran, O.A., and Scriven, L.E., J. Comp. Phys., **97**, 489 (1991).

17. Basaran, O.A., J. Fluid Mech., **241**, 169 (1992).

18. Putt, R., M.S. Thesis, University of California, Berkeley, 1975.

19. Sides, P. and Tobias, C.W., J. Electrochem. Soc., **132**, 583 (1985).

20. Janssen, L.J.J. and Hoogland, J.G., Electrochim. Acta, **18**, 543 (1973).

21. Janssen, L.J.J. and Hoogland, J.G., Electrochim. Acta, **15**, 1013 (1970).

22. Dees, D., Ph.D. Thesis, University of California, Berkeley, 1983.

23. Sides, P. and Tobias, C.W., J. Electrochem. Soc., **132**, 583 (1985).

24. Egan, E.W. and Tobias, C.W., J. Electrochem. Soc., **141**, 1118 (1994).

25. Charles, G.E. and Mason, S.G., J. Coll. Sci., **15**, 236 (1960).

Chapter 2. EXPERIMENTAL

A. Overview

The apparatus and techniques developed in this research detect the position of a moving bubble interface as a function of time. H_2-H_2, H_2-O_2 or O_2-O_2 bubble pairs (0.005- to 0.1-cm diameter) were generated electrolytically on the tips of aligned, opposing microelectrodes. The bubbles were positioned relative to each other and the detector. A magnified image of the bubble shadows was projected onto an optical detector. The detector, which consisted of a 1-D photodiode array and associated data acquisition system, recorded the position of the interface as a function of time. The bubble size, electrolyte viscosity, and surface tension were varied independently. The four major components of the system, the laser projection apparatus, the electrolytic cell, the video microscope, and the detector, and the procedures for setting up and running the experiments will be described.

B. Apparatus

Operating Principles – The observation technique utilizes the fact that the gas bubbles reflect and/or diffusively refract light. Therefore, when illuminated from behind, bubbles generate shadows. Sides[1] used this principle to study bubble dynamics by cinematographic methods to photograph bubbles as dark circles with dimly lit centers and thin, bright edges; an example is shown in figure 2-1. The bright edges are a superposition of background illumination and slightly refracted light passing just along the bubble interfaces. The bright edge and the adjacent shadow provide a sharp contrast in light

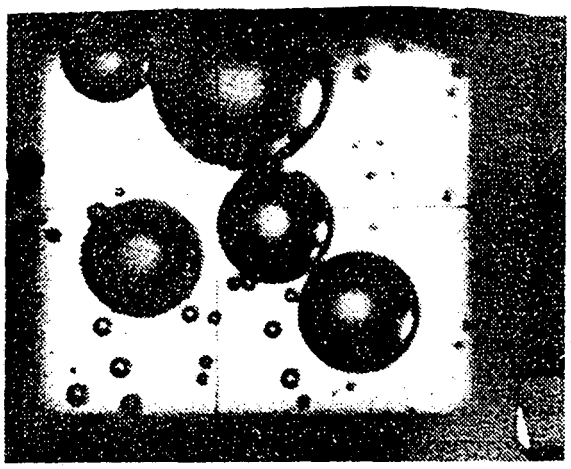

XBB 800-11782A

Figure 2-1. Back-lighted bubbles from Sides[1].

intensity that can be used to detect the location of the surface of a bubble. To measure the intensity of laser light near the bubble surface, a beam profilometer was constructed and used in this study. A detailed description of this apparatus is given in Appendix IA.

Laser Projection Optics – The laser projection apparatus constructed for this research creates an image consisting of the shadow of two coalescing bubbles which is projected onto a photodiode array (detector). A schematic of the optics is shown in figure 2-2. The Lexel model 75 argon ion laser emits up to 80 mW of 488 nm laser light as measured with a Coherent 2000 power/energy meter. The beam expander, which consists of 12.5- and 50-mm focal length spherical lenses, collimates the beam and expands it by a factor of 3.8. The diameter of the expanded beam is 3.2 mm as measured with the beam profilometer. The beam expander is followed by the beam sheet lens, a 25.4-mm focal

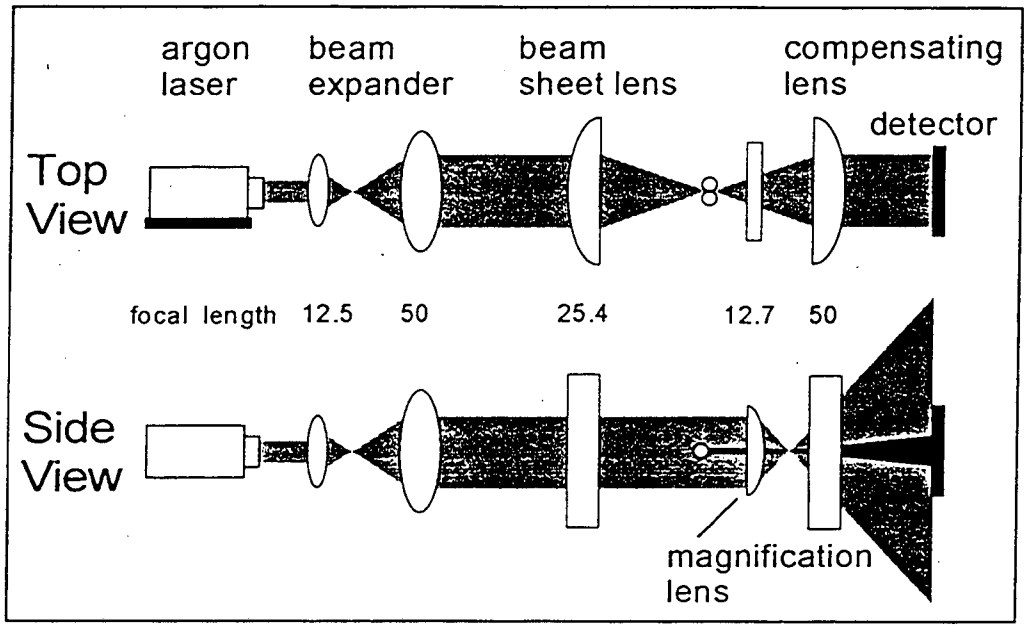

Figure 2-2. Schematic of Laser Projection Optics. Focal lengths shown (in mm) are those of lenses used for 150- and 375-μm diameter bubble experiments.

coalescence of two 600-μm diameter bubbles) without reducing the laser intensity below depth of focus. A horizontally oriented, 12.7-mm focal length cylindrical lens magnifies the image of the coalescing bubbles in the vertical direction. The final lens in the sequence, the 50-mm focal length compensating lens, collects the light diverging from the beam sheet lens and projects it onto the detector. All lenses used are achromatic and were supplied by Melles Griot[2]. The detector is described below. Lens selection and optical setup procedures are described in detail in Appendix IB.

Electrolytic Cell – The electrolytic cell used in this research is shown in the photograph in figure 2-3 and in the schematic in figure 2-4. The 20-ml electrolytic cell was constructed with 0.32-cm thick plexiglass walls joined together using methylene chloride

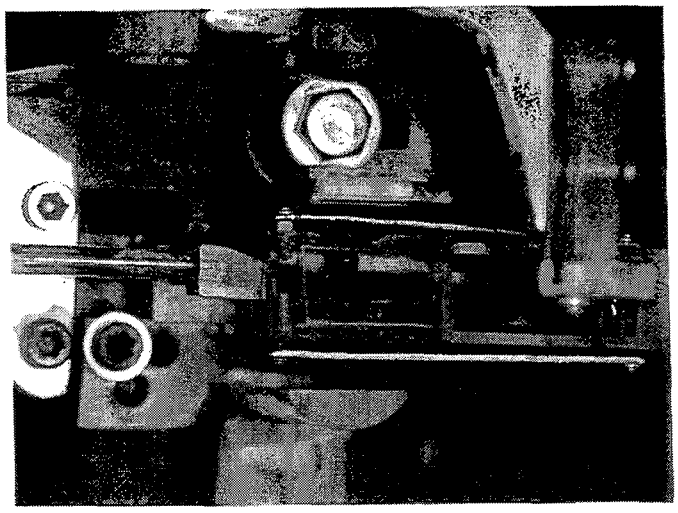

XBL 9411-6867

Figure 2-3. Top view of Electrolytic Cell.

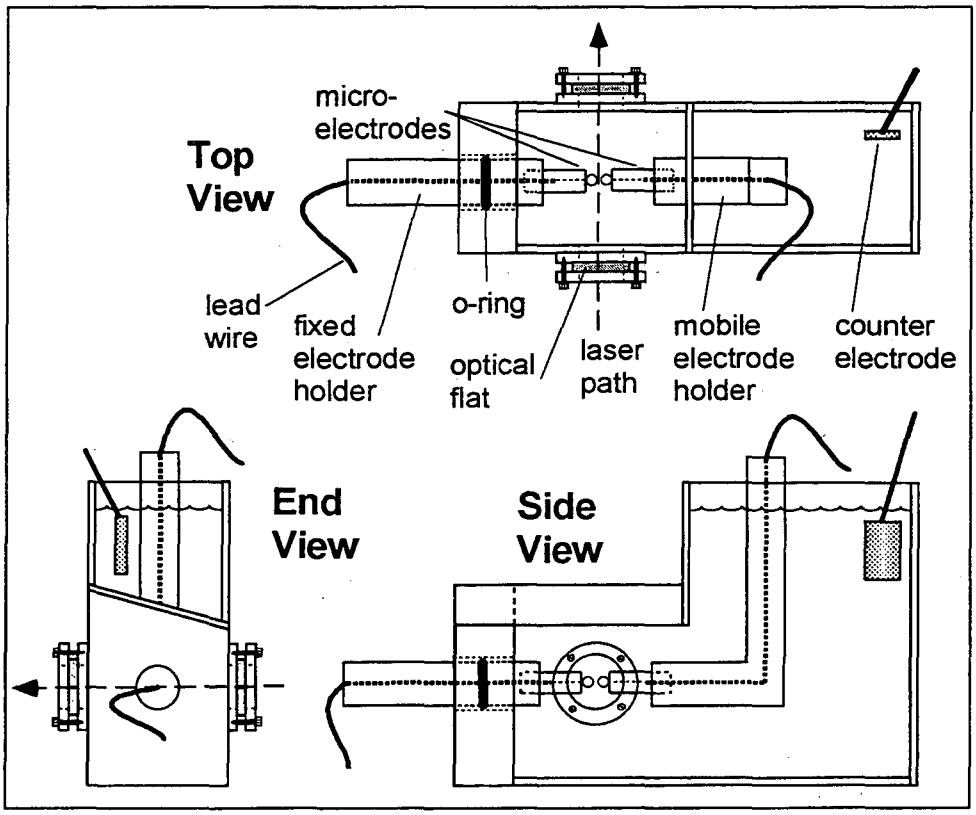

Figure 2-4. Schematic of Electrolytic Cell (not to scale).

with 10% acetic acid. To minimize optical distortion along the laser path, 0.32-cm thick, 1-cm diameter glass optical flats are pressed against open ports drilled in the plexiglass cell walls. To permit the magnification lens to approach the microelectrodes closely, the distance from the microelectrodes to the second optic flat along the laser path is 1.0 cm. The microelectrodes consist of 127-μm diameter platinum wires that are thermally sealed inside 0.3-cm diameter soft glass tubes. Insulated copper wires contact the platinum wires by conducting epoxy and connect the microelectrodes to the current source. The microelectrode faces were polished to a mirror finish using 0.25-μm Metadi diamond polishing compounds and a Beuhler metallurgical polishing wheel. The acrylic resin electrode holders, one fixed and one movable relative to the cell, fit tightly around the microelectrodes. A 1-cm^2 platinum sheet welded to a 0.1-cm diameter platinum wire was used as a counter electrode. Details of the cell construction are given in Appendix Ic.

Current was supplied to the electrodes with a Princeton Applied Research (PAR) 173 potentiostat operated in galvanostatic mode to generate bubbles. For the generation of hydrogen bubbles, the cathodic current was divided between the microelectrodes with an adjustable potentiometer while the sheet electrode served as the anode. For the generation of oxygen bubbles, the anodic current was divided between the microelectrodes. To generate one oxygen and one hydrogen bubble, one microelectrode was used as the positive electrode, the other as the negative electrode and the platinum sheet was not required. By adjusting the total current to the cell using the potentiostat and the relative current to each electrode using the potentiometer, two equal-sized bubbles were grown at approximately the same slow rate, with the time from nucleation to

coalescence typically about 5 to 10 min. The bubbles remained attached to the electrodes until they were detached by the violent motion of the interface during the coalescence event.

Video Microscope – Bubble evolution was observed through the top of the cell with the microscope shown in figure 2-5. To accommodate microscopic observations, the acrylic resin above the microelectrodes is angled so bubbles that detach from the electrodes do not obstruct the field of view. In addition, the maximum distance from the microelectrodes to the angled top is 1.2 cm to permit the close approach of the 8x magnification microscope objective to the electrodes. Lighting for the microscope is supplied from beneath the cell with a fiber optic cable aimed into the microscope objective. Depending on the microscope objective and eyepiece chosen for a given experiment, magnifications of 100 to 750 are possible. A Javelin video camera is pointed down into the microscope objective. Video monitoring and recording is accomplished with a Sony U-Matic recorder.

Detection System – The detector was designed to sense the rapid transition from light to dark produced by the passage of a bubble interface through a laser sheet. The prototype for this detector was described by Egan and Tobias.[3] Modifications were made to the prototype to increase the signal-to-noise ratio. The detector device was designed around a Hamamatsu[4] S4114 series high-speed linear photodiode array which consists of sixteen 0.09-cm elements on 0.1-cm centers capable of responding to a light-to-dark

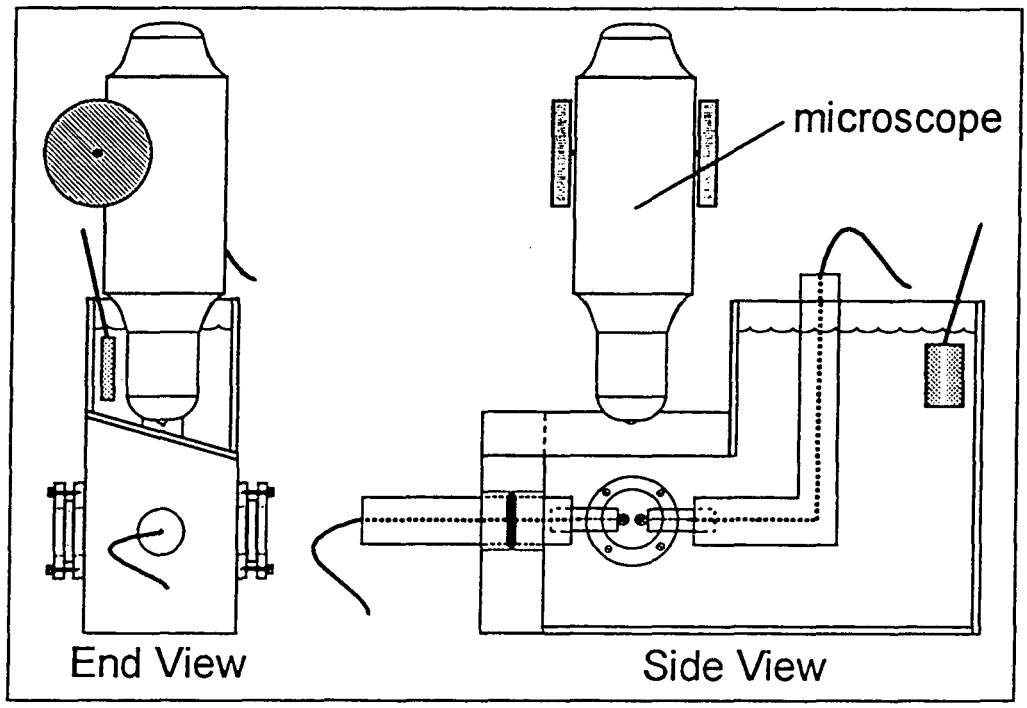

Figure 2-5. Schematic of electrolytic cell with microscope (not to scale).

transition in less than 50 ns. The 16 elements are connected in parallel through 16 high-speed video amplifiers to boost the weak diode output by 50 times to over 4.0 V. Each detector element output is adjusted by a resistor to eliminate any offset bias. The amplified signals then go through four Maxxim four-channel high-speed comparators that convert the analog into digital signals by referring to adjustable reference voltages. The binary signals are stored in the 4-kB on-board memory (256 time steps over 16 channels). The data from each new time step overwrite the oldest record. The data-acquisition logic is equipped with a self-triggering capability, and the storage sequence is initiated by the coalescence event. When the shadow passes one of the two center elements, the logic signals a computer (IBM-PC) to download the data to disk storage and to reset the trigger. The data are displayed on the PC monitor as 256 rows (time steps), with a pound

sign (#) signifying the on condition and a period (.) signifying the off condition. An example of the raw data is shown in figure 2-6. With this triggering protocol, the detector system is able to record the location of the interface as a function of time both before and during a coalescence event. The detector circuitry includes a 1-MHZ crystal oscillator and a 100-increment dwell setting which permits sampling rates from 10 to 1000 kHz, or 10,000 to 1 million 16-element samples per second.

To test the detector response, a rotating beam chopper was used to generate a constant velocity of 200 cm/s, which is approximately the velocity of a coalescence transient. It was found that each element responded equally and that the overall velocity, measured as the slope of the position versus time data, equaled the known velocity of the chopper blade.

Electrolyte Preparation – The electrolyte used in most of the experiments was

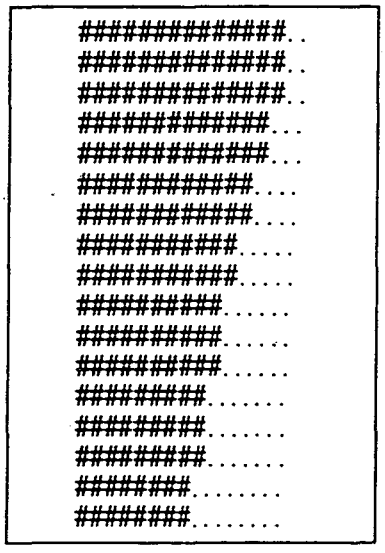

Figure 2-6. Raw Detector Data.

aqueous 1M H_2SO_4. To test the effect of pH, some experiments were conducted in aqueous 2M KOH. The electrolyte was prepared by combining volumetrically measured amounts of deionized water and weighed amounts of reagent grade chemicals. The water was purified with a Barnstead NANO Pure system to a resistivity of at least 15 megaohm-cm. The kinematic viscosity was increased by use of dextran T40 polysaccharide and the surface tension was lowered by adding 2-hexanol. The viscosity was measured with a capillary viscometer to the nearest 0.05 cSt. A variable shear rate viscometer was used to confirm that the dextran-acid solutions were Newtonian up to shear rates of 100 s^{-1}. Surface tensions were checked with a Wilhelmy plate apparatus to the nearest 3 dynes-cm^{-1}. Details of the electrolyte preparation and testing procedures are listed in Appendix ID. Used electrolyte was tested to determine if the viscosity or surface tension changed during the coalescence experiments. No significant changes were observed.

C. Experimental Procedure

The overall experimental procedure included setting up the cell and the optics, positioning the bubbles, evolving pairs of bubbles, fine tuning their positions and recording the dynamics of coalescence.

Cell Setup – The dimension of the coalescence event (approximately the diameter of one bubble) and the size of the image (slightly less than 1.6 cm, the size of the photodiode array) were known, so the required magnification was determined by taking their ratio,

$$magnification = \frac{i}{o} \tag{1}$$

where o ≡ object distance, and
i ≡ image distance

as illustrated in figure 2-7. The cell, the detector, and the magnification lens were

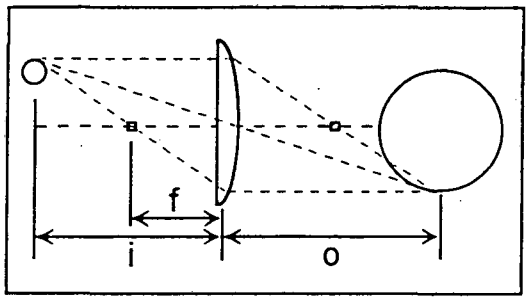

Figure 2-7. Lens equation variables.

positioned according to the following equation:

$$\frac{1}{f} = \frac{1}{i} + \frac{1}{o} \tag{2}$$

Here, f is the lens focal length.

Bubbles pairs of equal size were used in all experiments. To set the bubble size for a given experiment, the relative positions of the microelectrodes were adjusted. The distance between the electrode faces was set to twice the desired bubble diameter[a]. Gap distances were determined to within 2% of the total gap width, as observed on the video monitor. Details of the procedure for positioning the lenses and the microelectrodes are

[a] The thickness of the liquid film that separated the bubble immediately before coalescence was negligible compared with the bubble diameters.

given in Appendix IB.

Coalescence Data Collection – Gas bubbles were generated by electrolysis of the water at a rate controlled by the current applied by the galvanostat. For hydrogen bubbles, a current of approximately 30 μA was applied for a few minutes to grow the bubbles until they came close to contacting each other. During this time, the potentiometer was adjusted to control the relative current to each electrode to ensure that the bubbles were of equal size. Growth continued for another few minutes at a current of approximately 3 μA until light from the fiber optic source no longer passed between the bubbles into the microscope. Since the shadows of the bubbles became visible on the face of the detector once they had grown into the laser light sheet, final positioning of the bubbles relative to the detector was confirmed by observing the image itself. Growth up to coalescence was accomplished by applying a trickle current of less than 1 μA for about thirty seconds. During this final growth period, no positioning adjustments were made and no contact was made with the optics table. Hence, conditions were maintained to ensure that coalescence occurred in an essentially stagnant medium. Coalescence automatically triggered the detector circuitry.

For most of the experimental conditions used, two sets of data were collected: one at a low sampling rate to capture the long-time behavior and another at a high sampling rate of 1×10^6 samples per second to capture the initial motion of the interface. Typically, data from 15 to 20 bubble pairs were collected at each dwell setting. After a given bubble pair coalesced, the electrolytic cell was moved vertically so that the subsequent

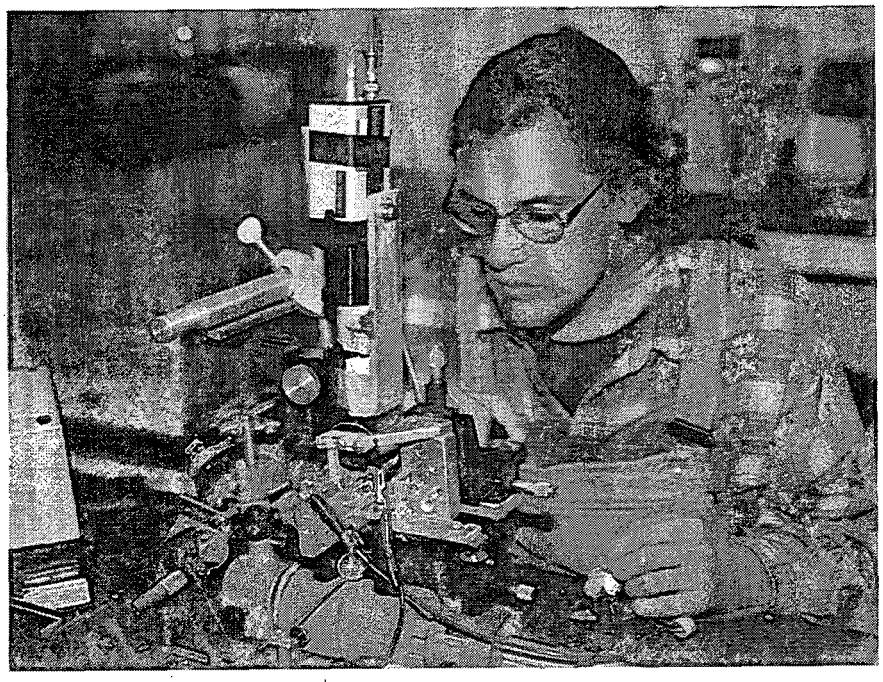

XBC 9411-6866

Figure 2-8. Apparatus adjustment before coalescence data collection. The electrolytic cell, laser optics, video microscope, and author are shown.

coalescence event would be recorded by a different set of photodiode elements. By rastering the shadows of consecutive bubble pairs up and down the array in this way and a averaging the results, smooth position versus time curves were obtained.

The laser projection apparatus records the position of the interface at one selected bubble cross section as a function of time during coalescence. The plane of coalescence between two bubbles was the cross section of greatest interest because the velocities and displacements at this position were the largest. By taking data along a series of cross sections over many coalescence events, it was possible to create a composite image of the cross section of the bubble interface.

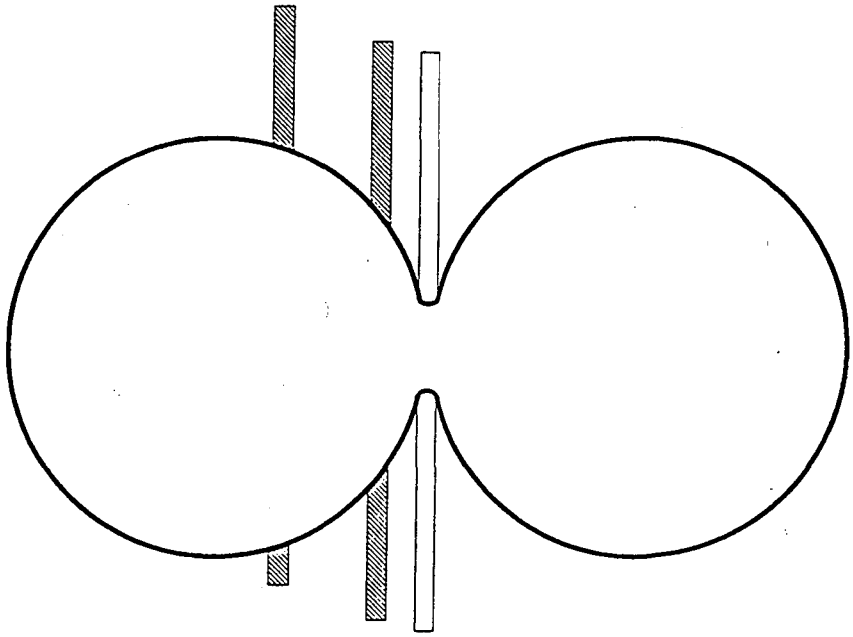

Figure 2-9. Laser beam sheet positioning along bubble cross section. The shaded beam sheet (center of schematic) is positioned in the cusp to detect saddle point motion. The striped beam sheets are positioned to detect motion at other locations along the cross section of the interface.

References

1. Sides, Paul J. "Bubble Dynamics at Gas-Evolving Electrodes", PhD Thesis, Department of Chemical Engineering, University of California, Berkeley, CA, December 1980.

2. Melles Griot Inc., 1770 Kettering Street, Irvine CA 92714 (U.S.A.).

3. Egan, E.W., and C.W. Tobias, "Measurement of Interfacial Re-equilibration during Hydrogen Bubble Coalescence", *J. Electrochem. Soc.*, **141**, 1118 (1994).

4. Hamamatsu Photonics K.K., Solid State Division, 1126-1 Ichino-cho, Hamamatsu City, 435 (Japan).

Chapter 3. RESULTS

A. General Form of Results

The experimental data give the position of the gas-liquid interface at the saddle point of two bubbles of equal size coalescing in aqueous electrolyte as a function of time (refer to figure 2-9). The motion of the lower saddle point of two coalescing 375-μm bubbles is shown in figure 3-1. In figure 3-1, zero on the time axis corresponds to the first time step during which motion was detected. The axis denoting the saddle-point position indicates the distance the saddle point has moved from the mutual axis upon which the two bubbles were aligned. The data shown in figure 3-1 are an average of the results of 40 different bubble pairs, 20 pairs at a high sampling rate of $1x10^6$ time steps per second for the first 60 μs and 20 pairs at a lower sampling rate of about $9.1x10^4$ steps per second.

Once coalescence begins, the saddle point moves radially away from the axis of the two bubbles as the cusp of the resultant bubble opens. The surface energy decreases as the curvature and surface area of the cusp decrease and the energy is imparted into the surrounding liquid. Since the volume of liquid moved increases as the cusp opens, the interface decelerates as shown on the expanded time scale in figure 3-1(b). The initial velocity of the saddle point is the slope of the position versus time data extrapolated to the position axis. The first eight data points were fit with a least squares regression line to determine the slope. Figure 3-1(b) shows that the saddle point of 375-μm bubbles in 1M H_2SO_4 has an initial velocity of 360 cm/s.

The interface moves past the position corresponding to the equilibrium edge of the resultant bubble, 236 μm, indicated with an arrow on the position axis in figure 3-1(a).

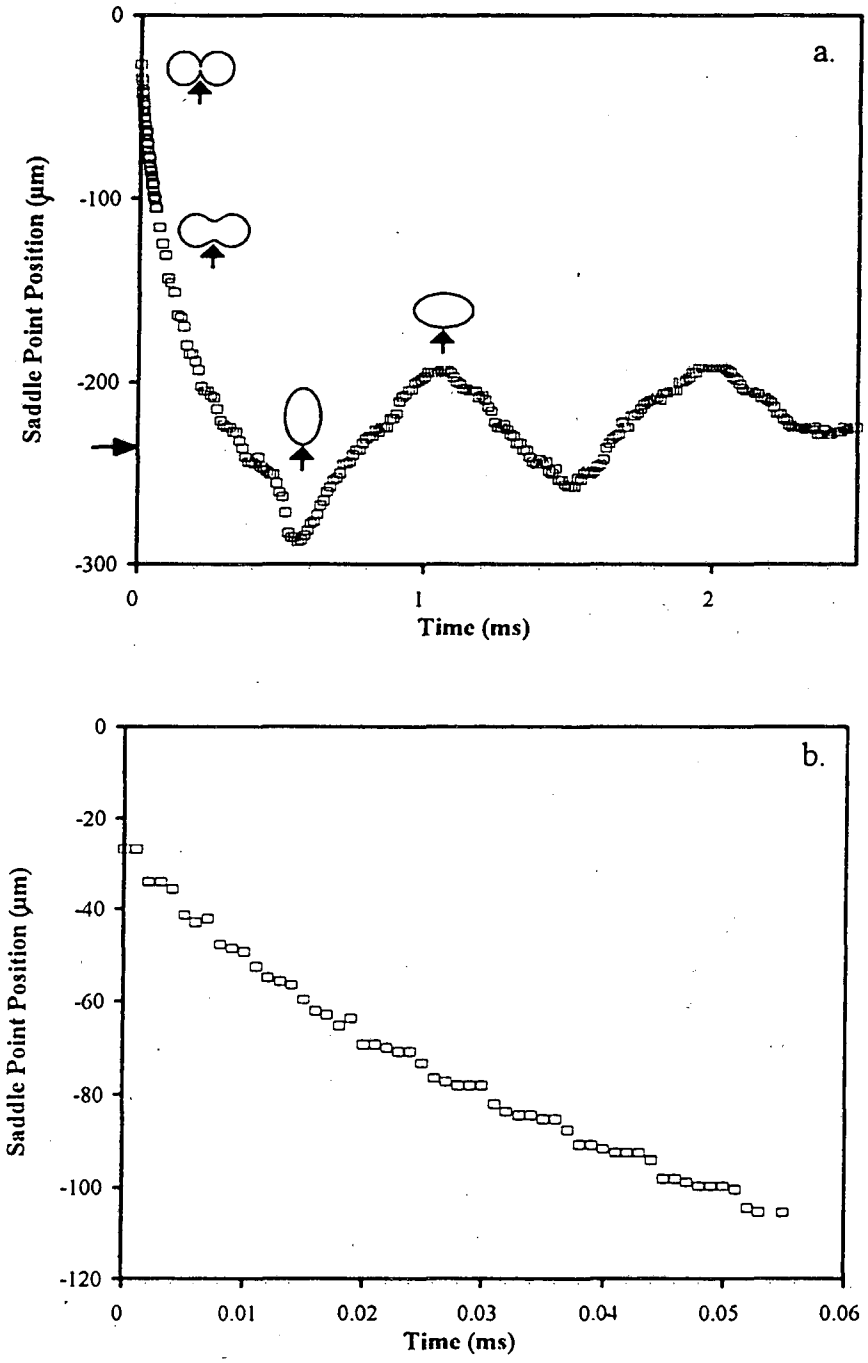

Figure 3-1. Saddle point position versus time for 375-μm diameter bubbles in 1M H_2SO_4. (a) The location of the saddle point on the cross section of two coalescing bubbles is indicated on the inset schematics. The position that corresponds to the equilibrium edge position of the resultant bubble, 236 μm, is indicated on the position axis. (b) Expanded scale for short time.

When the resultant bubble reaches its maximum prolate spheroidal deformation, the saddle point stops and begins moving back toward the alignment axis. The interface oscillates above and below the equilibrium position as the bubble translates between prolate and oblate spheroidal shapes. The time between the amplitude peaks in figure 3-1(a), the oscillation period, is 0.94 ms. The time constant of the exponential rate at which the oscillation amplitude decreases, the damping rate, is 0.54 ms^{-1}.

Small amplitude interfacial movements, superimposed on the initial and oscillatory motion of the saddle point, can be identified. At about 0.40 ms in figure 3-1(a), the saddle point appears to decelerate sharply, then accelerate at about 0.45 ms. Qualitatively similar though diminished deceleration and acceleration occur at about 0.8 ms. These small amplitude movements are indications of surface waves.

The bubbles detach from the electrodes on which they are grown after coalescence begins and the resultant bubble rises in the gravitational field. The net upward slope of the oscillations in figure 3-1(a) indicates buoyant motion. A comparison of the motion of the upper and lower saddle points of coalescing 260-μm bubbles is made by inverting the lower saddle point curve in figure 3-2. Buoyant motion clearly has no influence on the measured initial saddle-point velocity of 260-μm bubbles. Since buoyant motion occurs over a relatively large time scale, the initial motion and first few oscillations of the cusp are axisymmetric. The lower saddle point will be used throughout the remainder of this study.

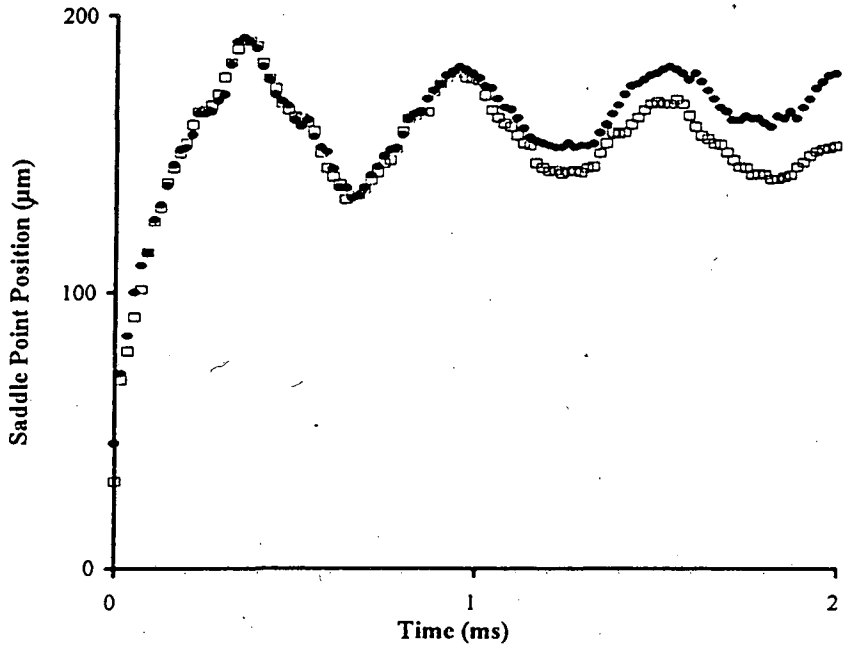

Figure 3-2. Comparison of 260-μm diameter bubble upper and lower saddle-point motion. Upper saddle-point (●) and lower saddle-point (□) data are plotted on a positive position axis to show the influence of buoyancy on detached resultant bubbles.

Accuracy - The initial velocity of the saddle point and the period and damping rate of its oscillations were determined using curves like that in figure 3-1. The accuracy of the measurements, therefore, depended on the precision with which values were read from the curves. Oscillation period was read to the nearest 0.05 ms or to within the nearest 3% for the largest bubbles examined in the experiments and 20% for the smallest. The damping rate was determined to the nearest 0.01 ms^{-1} for the largest bubbles and to the nearest 0.2 ms^{-1} for the smallest bubbles, corresponding to 2 and 8% precision, respectively. The initial velocity was measured to the nearest 25 cm/s for all bubble sizes, or to within 6 to 13% over the range of bubble sizes examined.

Errors in the position and time measurement by the photodetector were negligible

compared to the errors associated with reading the saddle-point curves. However, small random variations in the saddle-point position stemming from the discrete binary output of the photodiode elements gave the curves a rough appearance.

Two coalescence experiments using 375-μm hydrogen bubbles grown in 1M H_2SO_4 were set up and conducted on different days using different electrolyte batches. The results are compared in figure 3-3. Each curve in figure 3-3 is a composite of 40 bubble pairs. The results of the two experimental runs are almost identical.

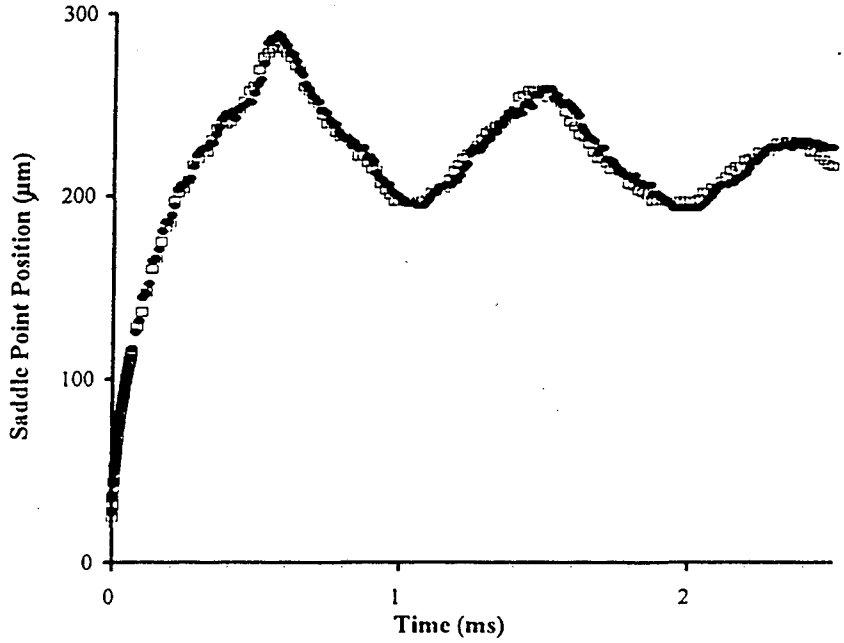

Figure 3-3. Experimental reproducibility. Two experiments with 375-μm hydrogen bubbles grown in 1M H_2SO_4 using different experimental set ups and electrolyte batches.

B. Bubble Size, Electrolyte Viscosity, Surface Tension Results

The influences of bubble size, electrolyte viscosity, surface tension, gas type, and pH on bubble coalescence were examined. The variables were changed independently.

Hydrogen bubble pairs with diameters of 50, 150, 375, and 600 μm were evolved in 1M H_2SO_4. Saddle point data are shown in figure 3-4, where it can be seen that the oscillation period increases and damping decreases with increasing bubble size. Large bubbles have higher initial saddle-point velocities than small bubbles as demonstrated in figure 3-4(b), but, the differences are small.

The kinematic viscosity of 1M H_2SO_4 electrolyte was raised to 3.0 and 5.0 cSt by adding dextran [$(C_6H_{10}O_5)_x$, 40,000 molecular weight] to a concentration of 6 wt% and 10 wt%, respectively. The coalescence of 375-μm bubbles in 5 cSt electrolyte and in 1M H_2SO_4 with a kinematic viscosity of 1.1 cSt are compared in figure 3-5. Increasing the viscosity increases the damping rate and slightly reduces the initial velocity of the saddle point without affecting the oscillation period. These results suggest that damping is controlled by viscous resistance to shear motion in the fluid surrounding the oscillating bubble. The bubble-size experiments, which indicated a higher damping rate for small bubbles than for large bubbles in equally viscous electrolyte, support the conclusion that damping is controlled by viscous resistance. The initial velocities derived from the data in figure 3-5(b) indicate that there is very little effect of viscous resistance in the surrounding fluid as the cusp begins to open.

The surface tension of 1M H_2SO_4 was reduced to 49 and 25 dyne/cm with the addition of 2-hexanol to concentrations of 0.001 and 0.07 M, respectively. The results are

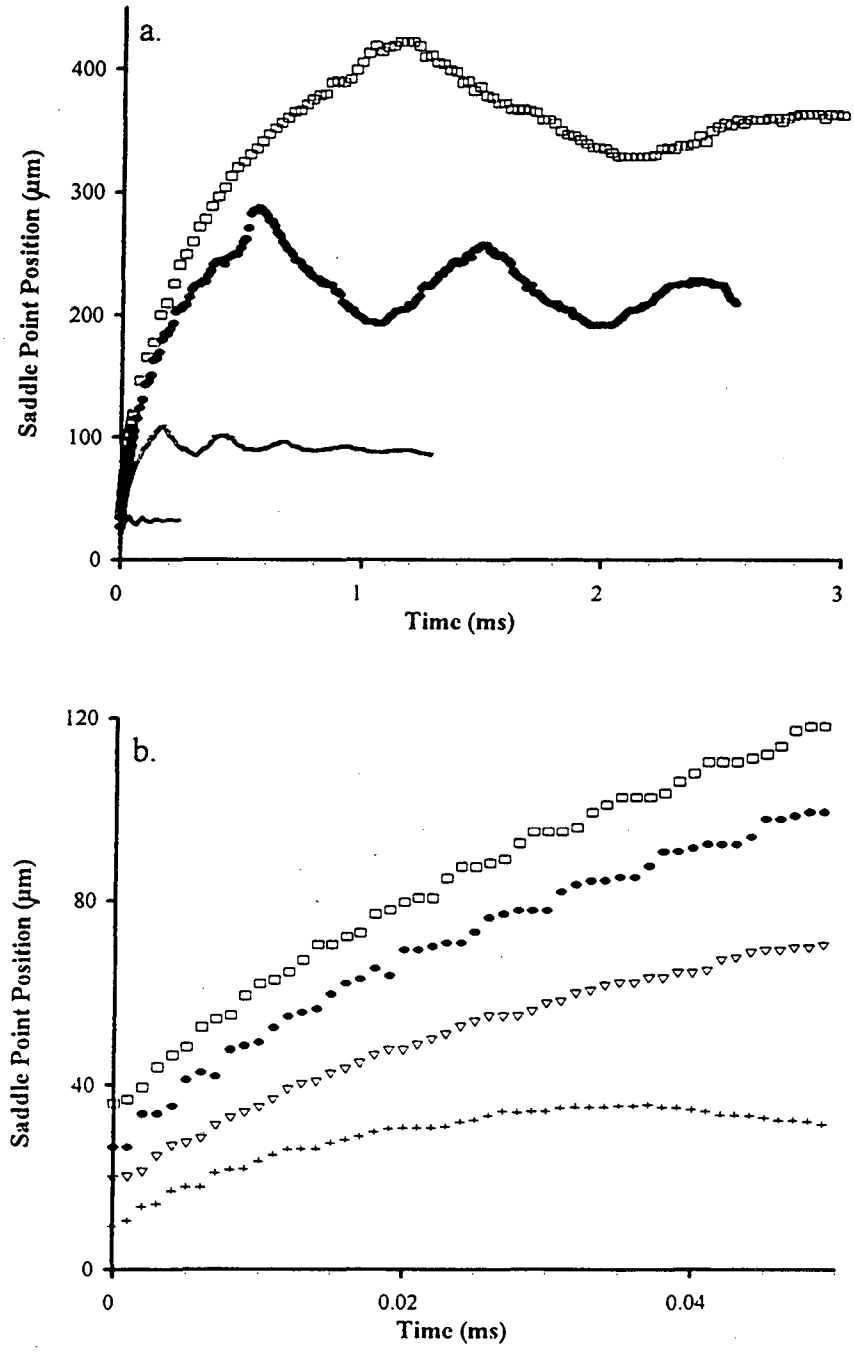

Figure 3-4. Bubble size. (a) Lower saddle-point position versus time for 600- (□), 375- (•), 150- (▽), and 50-μm (+) diameter hydrogen bubbles coalescing in 1M H_2SO_4. (b) Expanded scale for short time.

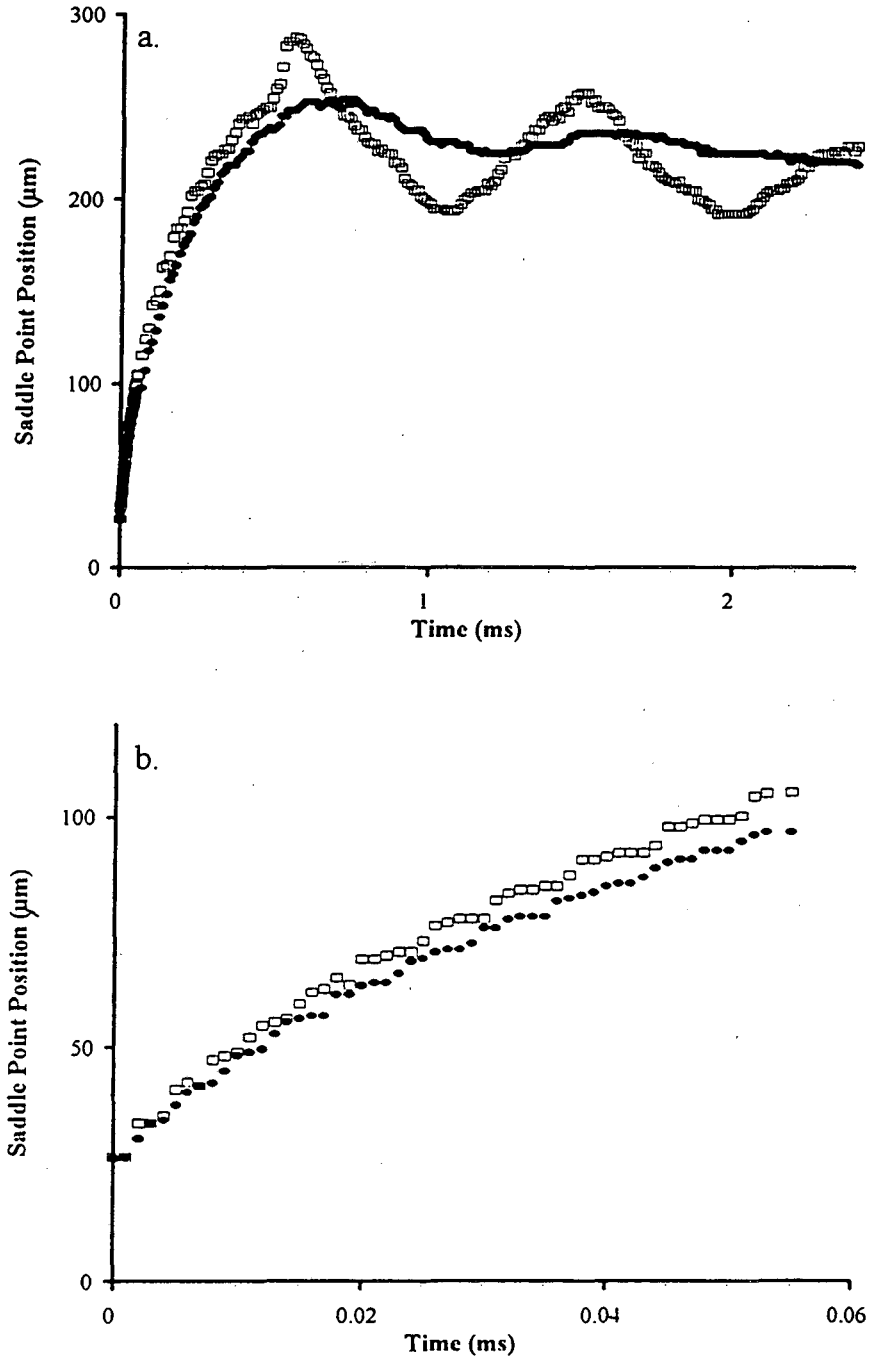

Figure 3-5. Kinematic viscosity. (a) Saddle point motion of 375-μm bubbles coalescing in 1M H_2SO_4 with 10 wt% dextran (●, ν = 5 cSt) and without dextran (□, ν = 1.1 cSt). (b) Expanded scale for short time.

presented in figure 3-6 and show that the oscillation period increased dramatically with the addition of alcohol. The response of the gas bubbles to surface deformation is slower at the lower surface tension, resulting in a longer period. Surface tension apparently has no effect on damping. The initial velocity results indicate only a slight dependence on surface tension.

C. Gas Type and pH Results

Oxygen bubbles were generated by applying a positive current to one or both of the microelectrodes. The coalescence of 375-μm diameter hydrogen bubbles is compared with that of two oxygen bubbles and with that of a hydrogen and an oxygen bubble in figure 3-7. The saddle-point initial velocity, oscillation damping rate, and oscillation period were the same within experimental uncertainty. This result indicates that coalescence does not depend on gas type.

Oxygen bubbles were generated in 1M H_2SO_4 and 2M KOH to examine the effects of electrolyte pH on bubble coalescence. The results for the coalescence of 253-μm diameter bubbles are shown in figure 3-8. Despite the slightly higher surface tension and kinematic viscosity of 2M KOH, the results in figure 3-8 demonstrate no measurable difference between coalescence events as a function of pH.

Numerical values of the initial saddle-point velocity, oscillation period, and oscillation damping rate for the bubble size, electrolyte viscosity, and surface tension experiments are listed in table 3-1. Hydrogen bubble pairs were used for all experiments in table 3-1. The curves for the motion of the saddle point from which these data were

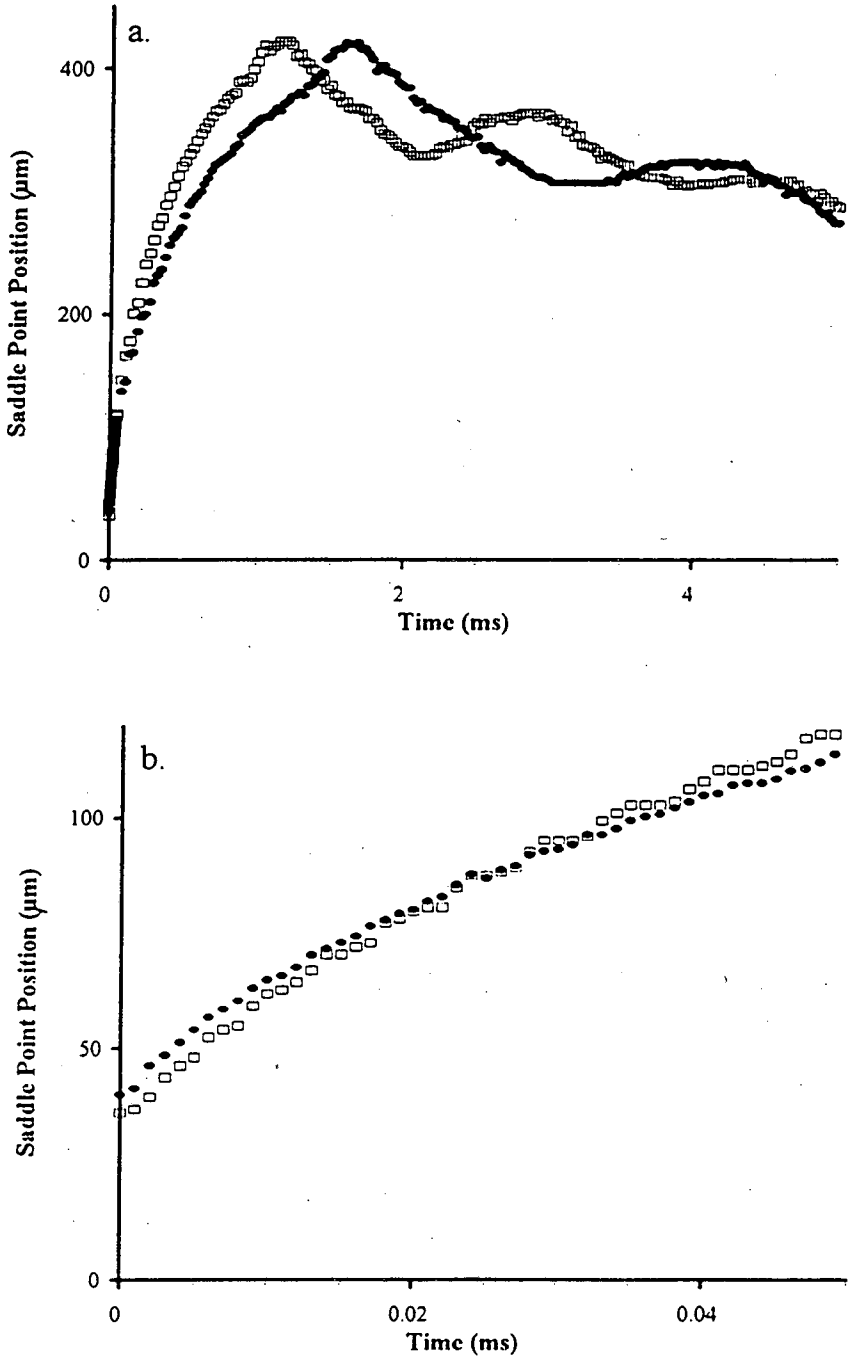

Figure 3-6. Surface tension, 600-μm bubbles. (a) Saddle point motion of hydrogen bubbles in 1M H_2SO_4 with 0.07M 2-hexanol (●, σ = 25 dyne/cm) and without alcohol (□, σ = 73 dyne/cm). (b) Expanded scale for short time.

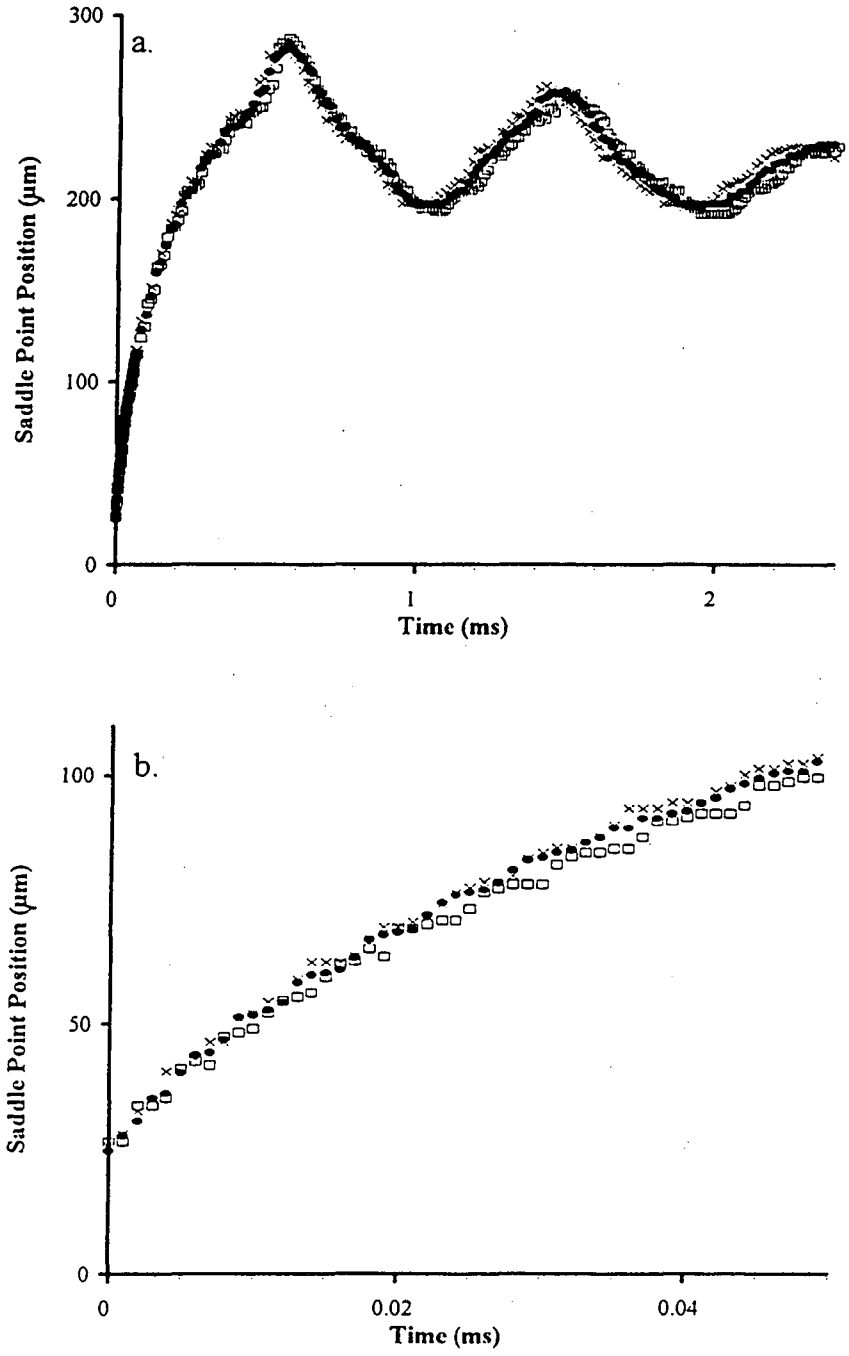

Figure 3-7. Gas type, 375-μm bubbles. (a) Saddle point motion of coalescing hydrogen-hydrogen (□), hydrogen-oxygen (●) and oxygen-oxygen (×) bubbles in 1M H_2SO_4. (b) Expanded scale for short time.

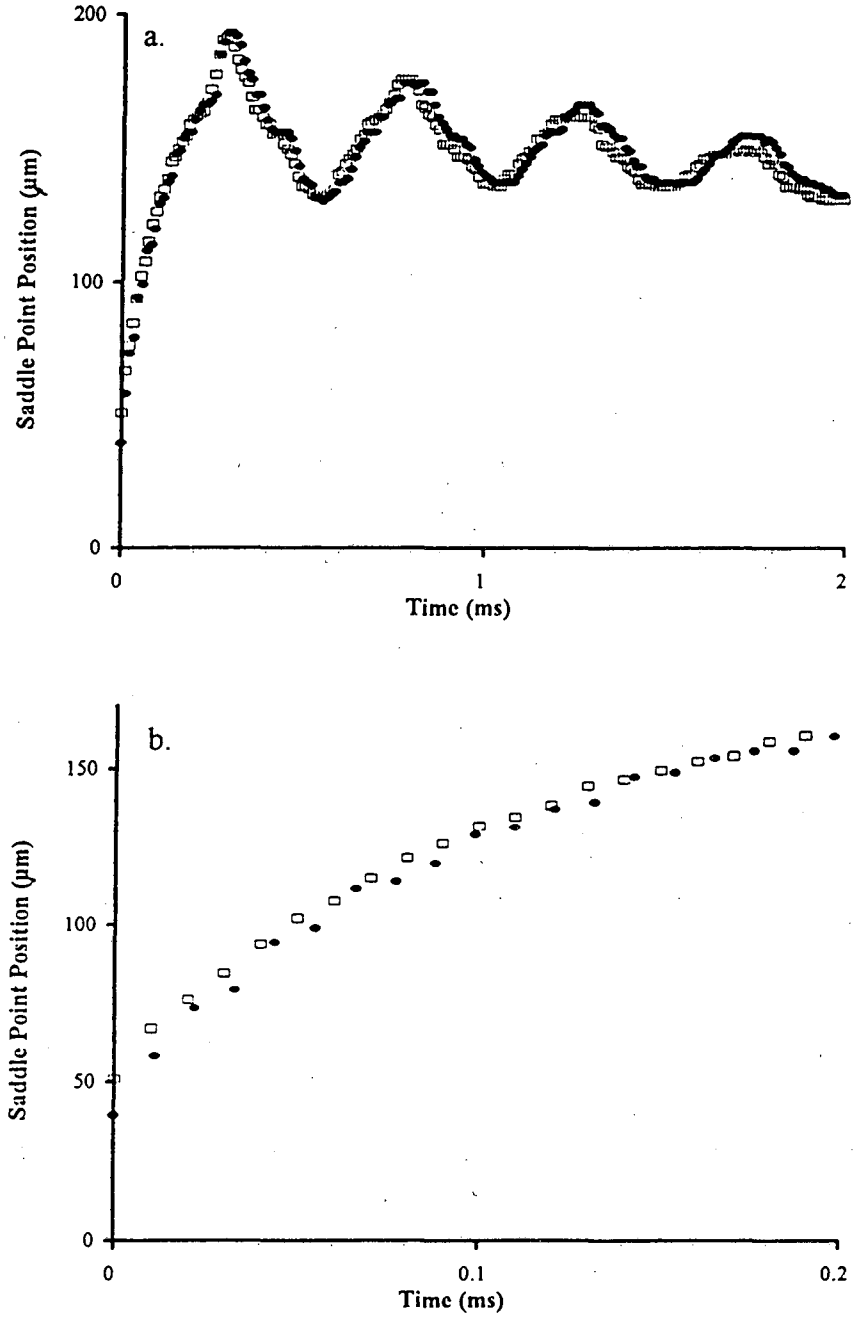

Figure 3-8. pH. (a) Lower saddle-point motion of 253-μm oxygen bubbles in 1M H_2SO_4 (□, σ = 73 dyne/cm, ν = 1.1 cSt) and in 2M KOH (●, σ = 76 dyne/cm, ν = 1.13 cSt). (b) Expanded scale for short time.

obtained are in the figures cited or in Appendix IIA. Numerical values from the gas type and pH experiments are listed in table 3-2.

Table 3-1. Results of size, viscosity, and surface tension experiments.

EXPERIMENTAL VARIABLES			MEASURED RESPONSES		
single bubble diameter (um)	surface tension (dyne/cm)	kinematic viscosity (cSt)	initial velocity (cm/s)	damping rate (1/ms)	period (ms)
600	73	1.1	342 +/- 25	0.40 +/- 0.02	1.78 +/- 0.02
600	49	1.1	331	0.6 +/- 0.2	1.90 +/- 0.02
600	25	1.1	321	0.40 +/- 0.02	2.70 +/- 0.02
600	73	3.0	316	0.53 +/- 0.02	1.88 +/- 0.02
600	73	5.0	400	0.70 +/- 0.02	1.89 +/- 0.02
375	73	1.1	360	0.54 +/- 0.05	0.94 +/- 0.02
375	49	1.1	308	1.1 +/- 0.5	0.97 +/- 0.02
375	25	1.1	336	0.9 +/- 0.2	1.34 +/- 0.02
375	73	3.0	315	1.14 +/- 0.05	0.92 +/- 0.02
375	73	5.0	284	1.97 +/- 0.05	0.98 +/- 0.02
150	73	1.1	250	2.8 +/- 0.2	0.252 +/- 0.005
150	49	1.1	140	6 +/- 2	0.284 +/- 0.005
150	25	1.1	210	3.6 +/- 0.2	0.408 +/- 0.005
150	73	3.0	212	13 +/- 4	0.25 +/- 0.01
150	73	5.0	195	20 +/- 4	0.25 +/- 0.01
50	73	1.1	187	14 +/- 2	0.057 +/- 0.002

Table 3-2. Results of gas type and pH experiments.

EXPERIMENTAL VARIABLES				MEASURED RESPONSES		
system	single bubble diameter (um)	surface tension (dyne/cm)	kinematic viscosity (cSt)	initial velocity (cm/s)	damping rate (1/ms)	period (ms)
H_2 - H_2 in 1M H_2SO_4	375	73	1.1	360 +/- 25	0.54 +/- 0.05	0.94 +/- 0.02
H_2 - O_2	375	73	1.1	350	0.52	0.91
O_2 - O_2	375	73	1.1	356	0.53	0.90
O_2 - O_2 in 1M H_2SO_4	253	73	1.07	158	0.90	0.24
2M KOH	253	76	1.13	170	0.90	0.25

D. Comparison to Literature Results

The results of this work are compared with those of Egan and Tobias[1] in figure 3-9. Their interface positions and the initial velocities (slopes) are both lower than those obtained in this work for similar bubble sizes in the same electrolyte. These differences are probably attributable to differences in experimental procedures. First, in the present work, the location of the mutual axis of the two bubbles (the zero point of the position axis) was recorded. Egan and Tobias considered only displacement, so the location of their zero point is arbitrary. Second, in the present work, the beam sheet was placed on the coalescence plane with high precision under microscopic observation. The placement of the beam sheet by Egan and Tobias was less precise because it was done visually. Since the saddle point has the highest velocity of any position along the resultant bubble cross-section, imprecision in beam sheet placement would reduce the measured velocities. The velocity observed by Egan and Tobias is lower than the saddle-point velocity since they obtained an average of the interface velocities in the region of the saddle point.

E. Interface Profile Results

A two-dimensional representation of the cross-section of two coalescing bubbles was generated by recording interface motion as a function of time at a number of axial positions (refer to figure 2-9). Data were collected at eleven locations on one side of the saddle point of coalescing 600-μm bubbles and mirrored to provide symmetric images of a portion of the resultant bubble interface. Although the range of axial positions examined was limited to those in the region of the saddle point, the sequence of frames shown in

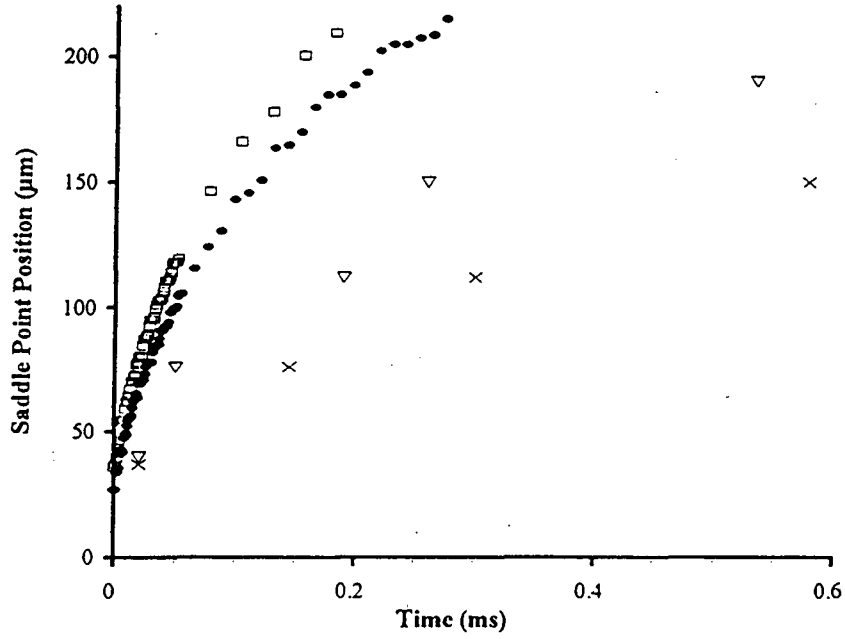

Figure 3-9. Comparison to literature results. Saddle point motion of 375 μm (•) and 600 μm (□) diameter bubbles compared to 500 μm (×) and 625 μm (▽) diameter bubble results of Egan and Tobias.

Figure 3-10 reveals phenomena that affect the entire interface. Surface waves, especially visible in the second frame in the sequence, start as interfacial deformations near the saddle point at the onset of coalescence. The motion generated by the traveling waves is superimposed on the events discussed thus far, namely, the opening of the cusp and the oblate-prolate spheroidal oscillations that follow. Despite the relatively small amplitude of the traveling waves, their impact on the motion of the saddle-point was noted as a deceleration followed by a sharp acceleration just before the interface reached its first maximum prolate deformation.

References

1. Egan, E.W. and Tobias, C.W., J. Electrochem. Soc., **141**, 1118 (1994).

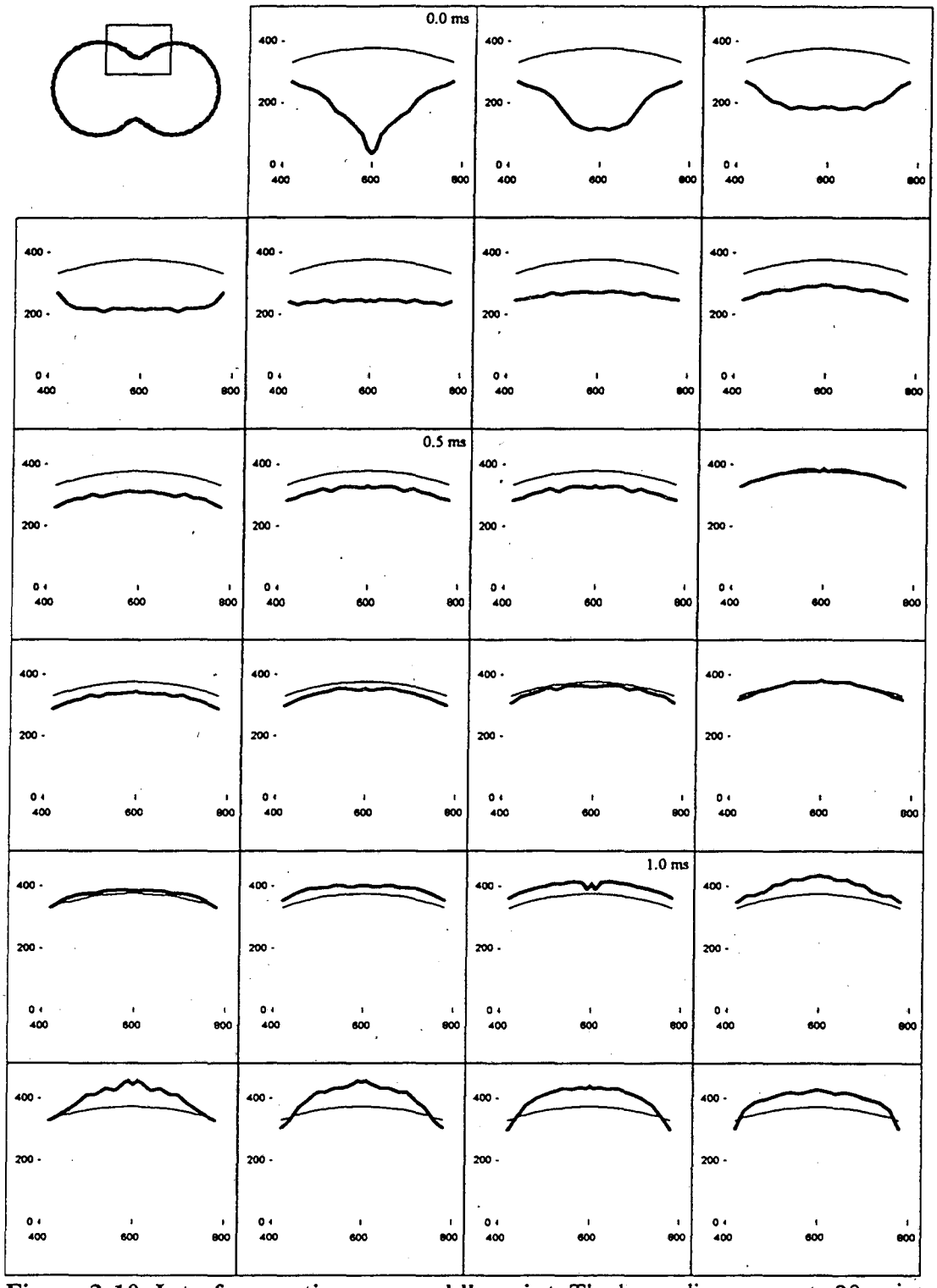

Figure 3-10. Interface motion near saddle point. The heavy line connects 20 points collected at approximately 0.063 ms/frame along the interface of coalescing 600-μm bubbles. The thin line indicates the equilibrium position of the resultant bubble interface.

Chapter 4. SCALING ANALYSIS

Because the shape of the resultant bubble and the dynamics it produces depend on each other, quantitative analysis of coalescence requires complex numerical computation. However, by making simplifying assumptions about the geometry and constituent forces, the problem can be reduced and analyzed to determine how the measured responses scale with the system parameters.

A. Initial Motion

For analysis of the initial motion of the saddle-point, it is assumed that all the surface energy given up by the liquid film that initially separates the bubbles is transfered to the kinetic energy of the receding liquid. A schematic of the saddle-point region of the system is shown in figure 4-1. Assuming an initially flat film and ignoring viscous effects and acceleration, the edge of a punctured hole in the film will propagate outward from the

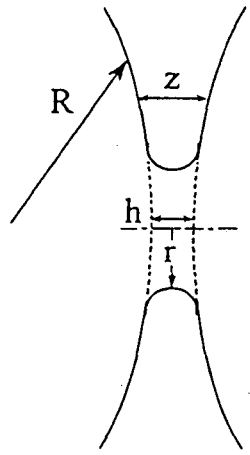

Figure 4-1. Initial motion analysis. This schematic shows a portion of two bubbles shortly after the liquid film that initially separates them has ruptured.

point of puncture driven by surface tension. An energy balance on the film at time t = 0, ignoring viscous dissipation, gives the following equation:

$$\tfrac{1}{2}\pi r^2 h \rho V_o^2 + 2\pi(4R^2 - r^2)\sigma = constant \qquad (1)$$

where r(t) ≡ radius of the hole that forms in the liquid film,
ρ ≡ liquid density
V_o ≡ initial velocity of the edge of the hole,
R ≡ single bubble radius,
σ ≡ surface tension, and
h ≡ thickness.

This equation is satisfied for any r provided

$$V_o = \sqrt{\frac{4\sigma}{\rho h}} \qquad (2)$$

Equation (2) predicts that a hole in a flat film should recede with an initial velocity that depends on the square root of the ratio of surface tension to initial film thickness. The initial bubble radius does not appear in the equation but might be expected to influence h. This result was presented by Dupré in 1864[1]. Culick modified this result by taking into account the acceleration of the initially stagnant liquid in the film[2], obtaining:

$$V_o = \sqrt{\frac{2\sigma}{\rho h}} \qquad (3)$$

This result differs from that of Dupré by a factor of √2. Both Dupré and Culick ignore dissipation, so the velocities predicted by equations (2) and (3) are expected to be higher

than the actual initial velocities. However, the purposes of this analysis, equation (3) will be used.

Charles and Mason applied the result from Dupré to a liquid drop coalescing with a planar liquid interface.[3] They assumed that the spherical film could be approximated by a parabola of radius R and applied the following expression for the receding film thickness, z:

$$z = h' + \frac{r^2}{2R} \tag{4}$$

Here, h′ is the thickness of the parabolic-planar film. By substituting z from equation (4) for the film thickness in equation (2), Charles and Mason obtained the following expression for the velocity, V, when the hole radius is r:

$$\frac{1}{V^2} = \frac{1}{V_o^2} + \left(\frac{\rho_1 + \rho_2}{8\sigma R}\right) r^2 \tag{5}$$

Here, ρ_1 and ρ_2 are the densities of the two phases.

Egan and Tobias modified the analysis by Charles and Mason to account for expansion of a hole in the thin film between two spherical bubbles[4]. By neglecting the gas-phase density contribution and replacing the planar interface with a second spherical interface (an additional factor of two), they obtained the following equation for the hole velocity:

$$\frac{1}{V^2} = \frac{1}{V_o^2} + \left(\frac{\rho}{4\sigma R}\right) r^2 \tag{6}$$

Egan and Tobias solved equation (6) for V to obtain

$$V = \frac{V_o}{\left(1 + \frac{\rho V_o^2 r^2}{4\sigma R}\right)^{\frac{1}{2}}} \tag{7}$$

Equation (7) can be modified to take into account the acceleration of the film by using the modification by Culick to the Dupré equation giving the final result for the hole velocity:

$$V = \frac{dr}{dt} = \frac{V_o}{\left(1 + \frac{\rho V_o^2 r^2}{2\sigma R}\right)^{\frac{1}{2}}} \tag{8}$$

Equation (8) predicts that high surface tension creates high velocity, that thin films permit high velocity, and that velocity decreases as the hole opens. The equation contains one parameter, either the initial velocity or, through equation (3), the initial film thickness. Equation (8) uses equation (3), which is rigorously valid only at t=0, so it should not be expected to be valid at finite times.

Equation (8) was numerically integrated using the initial velocity measured in the experiments. The calculations are plotted with the measured initial saddle-point motion of 150-μm hydrogen bubbles coalescing in 1M H_2SO_4 in figure 4-2. Equation (8) does not match the measured saddle-point velocity very well, nor does it correctly predict the rapid deceleration of the saddle-point observed with 150-μm bubbles. Comparisons with data from other experiments gave similar results.

These observations suggest that the assumptions made in the derivation of

equation (8) are invalid. The key assumptions in the derivation were the neglect of viscous forces and that the film recedes along parabolic trajectories. The experiments indicated only a weak dependence of initial velocity on kinematic viscosity. The surface deformations in the interface profile, however, demonstrate that the film does not recede along parabolic curves. These results indicate that the receding film thickens much more rapidly than predicted by equation (4). The initial motion is, unfortunately, too complex to lend itself to a simplified scaling analysis.

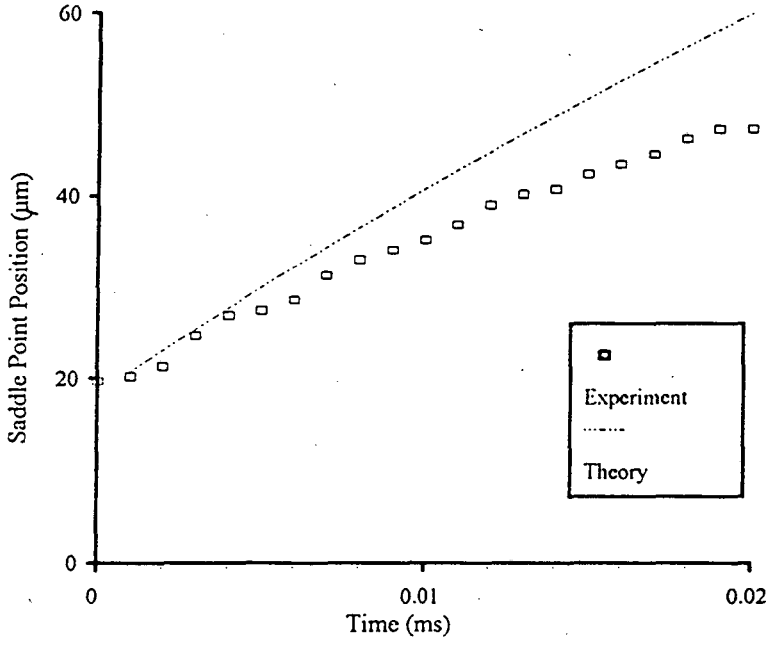

Figure 4-2. Initial saddle-point motion, modified Egan and Tobias theory compared to experiment. Coalescence of 150-μm bubbles in 1M H_2SO_4 is plotted with equation (8).

B. Oscillations

If the oscillating bubble is a slightly deformed sphere, as in figure 4-3, then surface tension acts as a restoring force, the surrounding fluid acts as a mass, and viscosity damps

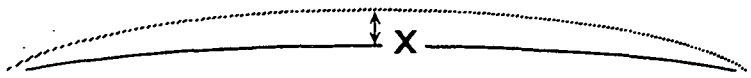

Figure 4-3. Oscillation analysis. The oscillating interface is modeled as a portion of a sphere deformed by a distance x.

the motion. The one-dimensional motion of the interface can be modelled as a damped harmonic oscillator.[5] The general equation for a damped harmonic oscillator is the force balance:

$$m\frac{d^2x}{dt^2} + c\frac{dx}{dt} + kx = 0 \qquad (9)$$

where m ≡ mass of liquid,
x ≡ displacement distance defined in figure 4-3,
t ≡ time,
c ≡ friction coefficient, and
k ≡ spring constant.

Applied to a moving interface, the mass is proportional to the bubble volume and the liquid density, the friction is proportional to the bubble cross sectional area and the liquid viscosity, and the restoring force is proportional to the bubble cross sectional area, the change in curvature, and the surface tension. Substituting these parameters into equation (9), the following equation is obtained:

$$A'\rho R^3\frac{d^2x}{dt^2} + B'\rho\nu R\frac{dx}{dt} + C'\sigma x = 0 \qquad (10)$$

where A', B', C' ≡ unspecified dimensionless geometric parameters
R ≡ resultant bubble equilibrium radius
ν ≡ kinematic viscosity
σ ≡ surface tension

The solution of equation (10) is

$$x = A \exp\left(\frac{-B\nu t}{R^2}\right) \sin\left(C\sqrt{\frac{\sigma}{\rho R^3}}\, t\right) \qquad (11)$$

where A ≡ experimentally measured oscillation amplitude (a function of R) and
B, C ≡ dimensionless combinations of A', B', and C'

The periodic term in equation (11) applies in the limit of Ohnesorge number $(\mu/\sqrt{\rho R\sigma}) \ll 1$ where μ is the viscosity. Since the coalescence experiments were conducted over an Ohnesorge number range of 0.006 to 0.06, viscosity is not expected to affect the oscillation period. In fact, the oscillation period did not vary significantly despite a five-fold change in kinematic viscosity. The model predicts that smaller bubbles and higher viscosities should lead to faster damping and this dependence agrees with the experimental results. The model indicates that a low surface tension or a large bubble size should lead to a lower frequency or a longer period which also agrees with the results.

A quantitative comparison between the scaling derived from the model and the experimental results is made in figures 4-4 through 4-7. The three parameters in equation (11) were fit to the experimental saddle-point for 375-μm bubbles coalescing in 1.1-cSt, 73-dyne/cm 1M H_2SO_4 in figure 4-4 using A = 56 μm, B=26, and C=5.67.

The data in figures 4-5 through 4-7, for which bubble size, electrolyte kinematic viscosity, and surface tension were changed from the conditions in figure 4-4, were fit

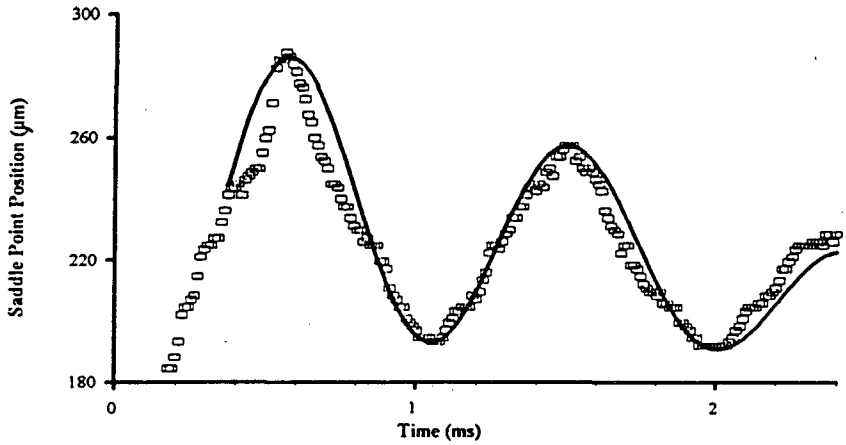

Figure 4-4. Oscillation analysis, parameter fitting. Saddle-point oscillations of 375-μm bubbles coalescing in 1.1-cSt kinematic viscosity, 73-dyne/cm surface tension electrolyte. Experimental data have been fit with equation (11) with three adjustable parameters.

with equation (11) without adjusting the parameters determined in figure 4-4.

Figure 4-5 shows that the damped harmonic oscillator model [equation (11)] predicts a lower damping rate than observed in the experiments, while, in figure 4-6, a higher damping rate is predicted than observed. According to figure 4-5, damping is less dependent on bubble size than the inverse square relationship in equation (11). If the exponent of the radius in the model is adjusted from 2 until the equation fits the experimental results (graph not shown), a value of 1.88 is obtained. A similar adjustment to the exponent of the kinematic viscosity gives a value of 0.8 rather than 1 as predicted by the oscillator equation for the data in figure 4-6.

Figure 4-5 also shows that the period depends on the bubble radius to a lesser degree than the 3/2 power predicted in equation (11). By adjusting the exponent until a good fit was obtained, the dependence of the period on the bubble radius was found to be

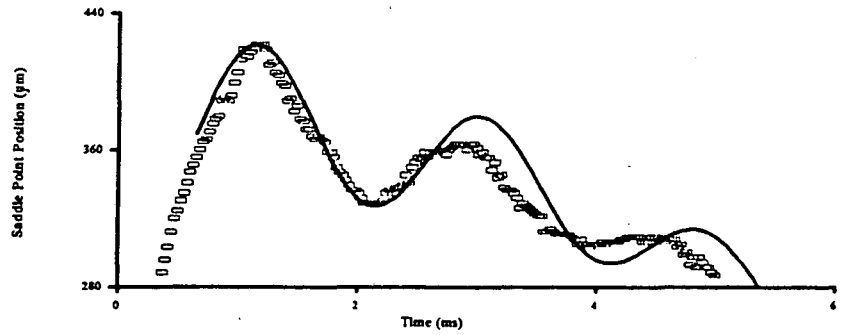

Figure 4-5. Oscillation analysis, bubble size change. Saddle-point oscillations of 600-µm bubbles coalescing in 1.1-cSt kinematic viscosity, 73-dyne/cm surface tension electrolyte. Experimental data are compared to equation (11) using the parameters derived in figure 4-4.

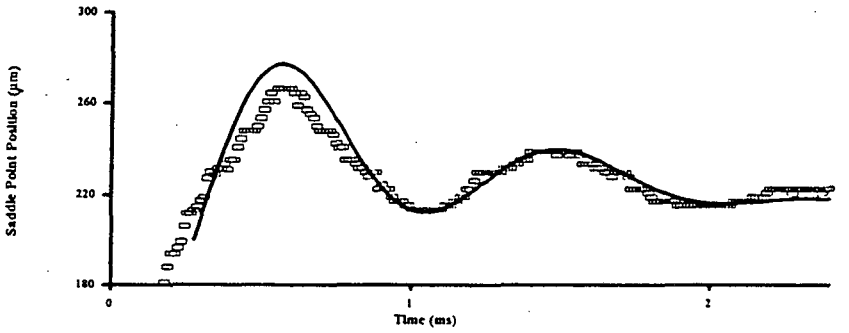

Figure 4-6. Oscillation analysis, viscosity change. Saddle-point oscillations of 375-µm bubbles coalescing in 3.0-cSt kinematic viscosity, 73-dyne/cm surface tension electrolyte. Experimental data are compared to equation (11) using the parameters derived in figure 4-4.

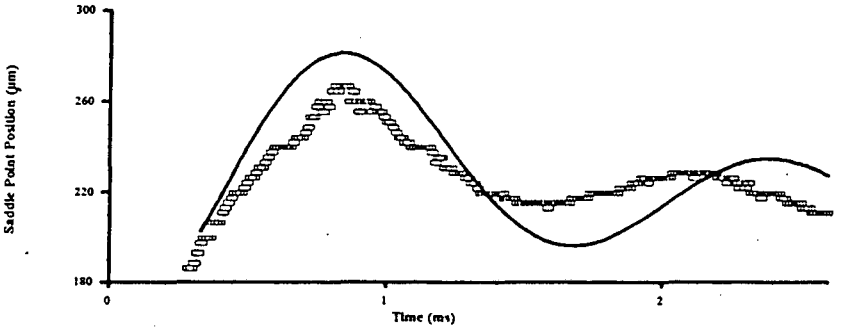

Figure 4-7. Oscillation analysis, surface tension change. Saddle-point oscillations of 375-µm bubbles coalescing in 1.1-cSt kinematic viscosity, 25-dyne/cm surface tension electrolyte. Experimental data are compared to equation (11) using the parameters derived in figure 4-4.

1.49. A similar calculation using the data in figure 4-7 showed that the experimental period varied with the 0.55 power of surface tension.

These calculations show that, with the exception of the dependence of damping on the electrolyte viscosity, bubble oscillation roughly scales with the system parameters as predicted by the equation that describes damped harmonic motion. The period of the oscillations varies with the bubble radius raised to the 3/2 power and inversely with the square root of the surface tension. Viscous resistance damps the oscillations at a rate proportional to the viscosity and inversely proportional to the square of the bubble radius.

References

1. Dupré, A., Ann. Chim. Phys., **4**, 194 (1864).
2. Culick, F.E.C., J. Appl. Phys., **31**, 1128 (1960).
3. Charles, G.E., and Mason, S.G., *The Coalescence of Liquid Drops with Flat Liquid/Liquid Interfaces*, Journal of Colloid Science, **15**, 236 (1960).
4. Egan, E.W. and Tobias, C.W., J. Electrochem. Soc., **141**, 1118 (1994).
5. Denn, M.M., Process Fluid Mechanics, Prentice-Hall, p.98, 1980.

Chapter 5. NUMERICAL ANALYSIS

A. Problem Specification

The scaling analysis revealed the constituent forces important to bubble coalescence; it did not, however, elucidate the evolving geometry of the resultant bubble. The Navier-Stokes equations with free surface boundary conditions provide a mathematical description of coalescence without decoupling the interface geometry and fluid dynamics and without requiring any adjustable parameters. The equations cannot be solved analytically but approximate solutions can be generated numerically.

The dimensionless Navier-Stokes equations that describe axisymmetric-surface-tension-driven flow are:

$$\frac{\partial u_r}{\partial t} + u_r\frac{\partial u_r}{\partial r} + u_z\frac{\partial u_r}{\partial z} = -\frac{\partial P}{\partial r} + Oh\left[\frac{\partial}{\partial r}\left(\frac{1}{r}\frac{\partial}{\partial r}(ru_r)\right) + \frac{\partial^2 u_r}{\partial z^2}\right] \quad (1)$$

$$\frac{\partial u_z}{\partial t} + u_r\frac{\partial u_z}{\partial r} + u_z\frac{\partial u_z}{\partial z} = -\frac{\partial P}{\partial z} + Oh\left[\frac{1}{r}\frac{\partial}{\partial r}\left(r\frac{\partial u_z}{\partial r}\right) + \frac{\partial^2 u_z}{\partial z^2}\right] + Bo \quad (2)$$

$$\frac{1}{r}\frac{\partial}{\partial r}(ru_r) + \frac{\partial}{\partial z}(u_z) = 0 \quad (3)$$

where t ≡ time
r ≡ radial coordinate
z ≡ axial coordinate
R ≡ resultant bubble radius
u_r ≡ radial velocity
u_z ≡ axial velocity
P ≡ pressure
Oh ≡ Ohnesorge number[1] ≡ $\mu/\sqrt{\rho R\sigma}$
Bo ≡ Bond number[2] ≡ $\rho g R^2/\sigma$

Time has been scaled by $\sqrt{\rho R/\sigma}$ and length by R. These equations, statements of the

conservation of momentum and mass, apply to both the liquid and gas phases. However, gas-phase contributions are assumed to be negligible. Axial symmetry has been assumed. Mass transfer across the interface has been implicitly neglected. Oh varied from 0.006 to 0.06 in the experiments, indicating that surface and inertial forces dominated the viscous forces. Bo varied from 0.0001 to 0.1, indicating that surface forces dominated the gravitational forces. Since Bo was small, gravity was ignored in the analysis and the mutual axis of the two bubbles was used as the axis of symmetry. The three equations contain three unknowns: two velocities and the pressure. At the free surface, the boundary conditions are:

$$P - 2\mu \frac{\partial u_n}{\partial n} = 2H\sigma \qquad (\textit{normal stress}) \qquad (4)$$

$$\frac{\partial u_T}{\partial n} + \frac{\partial u_n}{\partial T} = 0 \qquad (\textit{tangential stress}) \qquad (5)$$

where n ≡ direction normal to surface
T ≡ direction tangential to surface
u_n ≡ normal velocity
u_T ≡ tangential velocity
H ≡ mean surface curvature

Equation (4), the Young-Laplace equation, is a normal stress balance across the interface. Equation (5) states that the interface supports no tangential stress. All velocities are initially zero.

Once the liquid film that initially separates the two bubbles ruptures, the shape of the resultant bubble is determined by the solution of equations (1) through (5). The cross section of the initial shape of the resultant bubble can be approximated as an inverse ellipse

according to the following equations[3]:

$$x(\theta) = R_o[(1-m^2)(1+m^2)^{-\frac{1}{2}}(1+2m\cos 2\theta+m^2)^{-1}](1+m)\cos\theta \qquad (6)$$

$$y(\theta) = R_o[(1-m^2)(1+m^2)^{-\frac{1}{2}}(1+2m\cos 2\theta+m^2)^{-1}](1-m)\sin\theta \qquad (7)$$

where x,y ≡ Cartesian coordinates of inverse ellipse
R_o ≡ radius of circle with the same cross sectional area as ellipse
m ≡ deformation parameter, where m=0 corresponds to one circle and m=1 corresponds to two circles
and $0 \le \theta \le 2\pi$.

A value of m=0.99 was used in all simulation to approximate the geometry of two bubbles with a small hole in the liquid film that initially separates them. A curve generated with equations (6) and (7) is shown in figure 5-1.

Equations (1) through (5) were solved with FIDAP version 7.52. FIDAP is a general purpose finite element program by Fluid Dynamics International[4]. The program

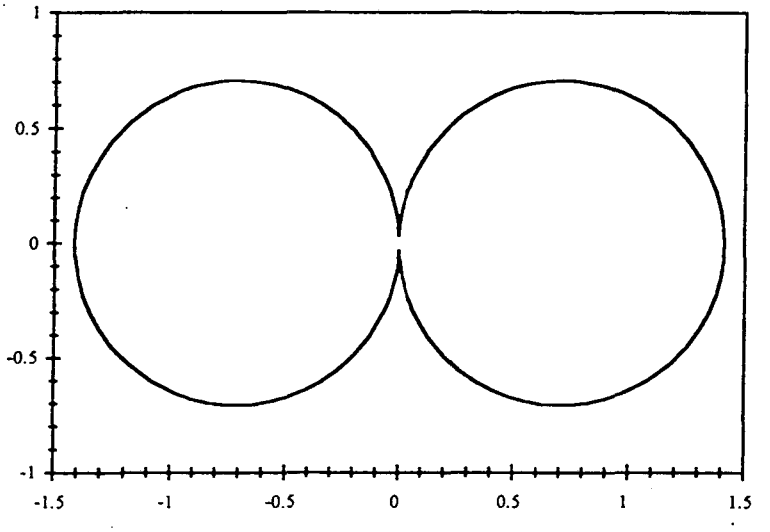

Figure 5-1. Inverse ellipse with R_o = 1 and m=0.99.

was run on a Hewlett Packard Model 715 work station with an HP-UX version 9.03 operating system. A user-supplied input file specifies the equations to be solved, the boundary conditions, the solution technique, and how the domain is to be meshed. A sample input file is printed in Appendix IIB. The meshed problem domain is shown in figure 5-2.

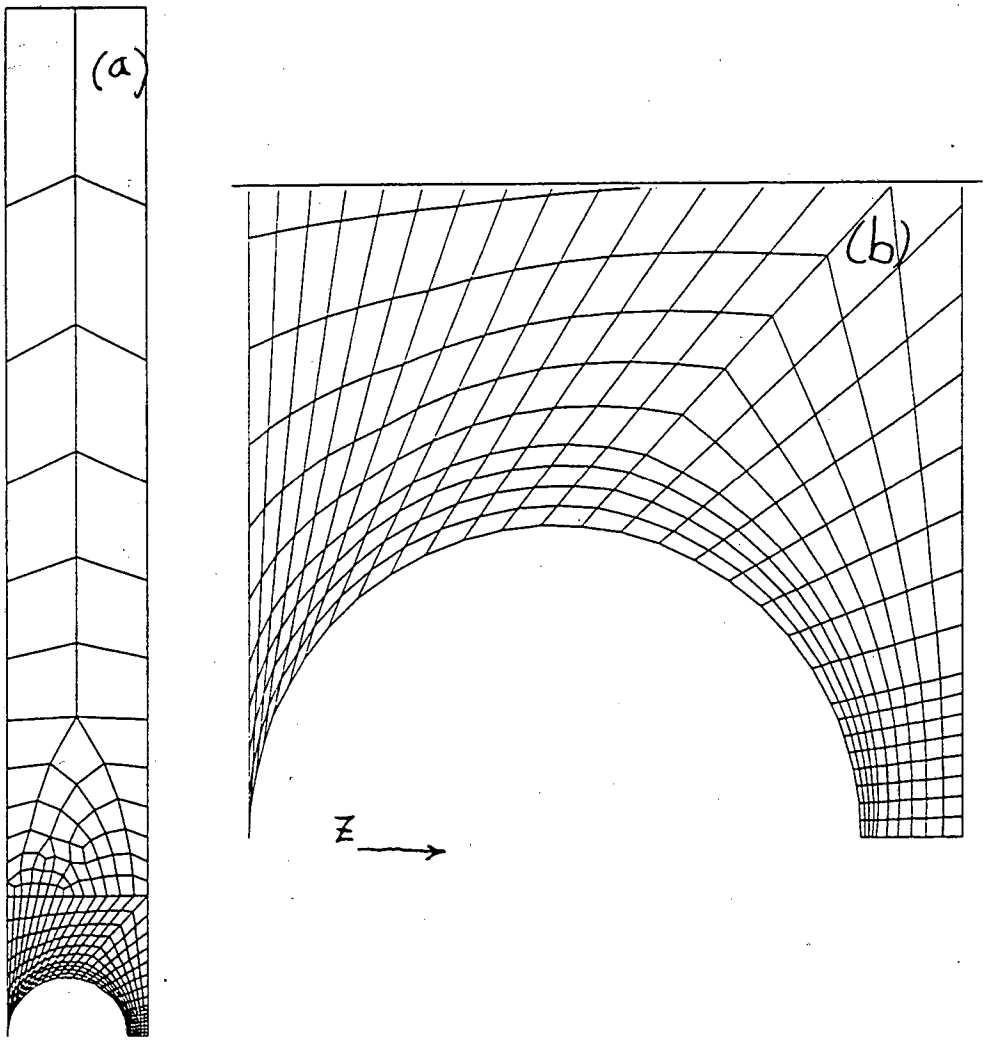

Figure 5-2. Meshed problem domain. (a) Full domain. (b) Magnified view of region near bubble interface. The numerical simulation is conducted on one quarter of the experimental domain assuming symmetric behavior. The bottom (z) axis is the axis of symmetry, the left side is a plane of symmetry, the top is a vessel wall and the right side is the electrode.

To reduce the number of calculations, only one quarter of the experimental domain was considered. The z-axis (bottom of figure 5-2(a)) is the axis of symmetry. The plane at z=0, hereafter referred to as the coalescence plane, is a plane of symmetry. The right border represents the electrode and the top border a vessel wall. The curve in the bottom left corner of the domain, specified with equations (6) and (7), represents the free surface. The intersection points of the lines in the figures are node points for the finite element algorithm. To solve free-surface problems, FIDAP uses a deforming spatial mesh. Nodes originally located on boundaries stay on boundaries. Mesh lines perpendicular to the surface shorten or lengthen to accommodate the motion of the surface. Nodes located on the perpendicular lines move along the lines.

Length, time, and mass were adjusted in the problem specification such that the surface tension, liquid density, and unit length used in the problem were unity. This scaling was done to minimize round-off errors.

B. General Form of Computed Results

In a more rigorous simulation of the experimental domain, the bubble surface is initially in contact with the electrode. It was found by trial and error that the simulation fails if the border representing the electrode was moved any closer to the bubble surface than shown in figures 5-1 and 5-2 where the bubble is 0.24 radii from the electrode. The influence of the location of the electrode was investigated by comparing the saddle-point motion results generated with the illustrated domain to the situation where the electrode is 11 units from the bubble surface (bubble radius = 1 unit). A comparison of the simulation

results in figure 5-3 shows that the proximity of the wall to the interface has only a small effect on saddle-point motion.

The simulated saddle-point-motion is compared to the experimental data in figure 5-4. The computed and measured saddle-point motions shown in figure 5-4 agree rather well. The average slope of the computed saddle motion in figure 5-4 (a) indicates a velocity of approximately 389 cm/s compared to the measured value of 360 cm/s for 375-μm bubbles coalescing in 1.1-cSt, 73-dyne/cm electrolyte. The period of the simulated oscillations shown in figure 5-4, 0.86 ms, was slightly less than the experimental value of 0.94 ms. The difference suggests that the surface tension in the experiments may have changed from the values measured before each run. This will be discussed in section D. The computed damping rate was 0.48 ms^{-1} compared to the experimental value of 0.54 ms^{-1}.

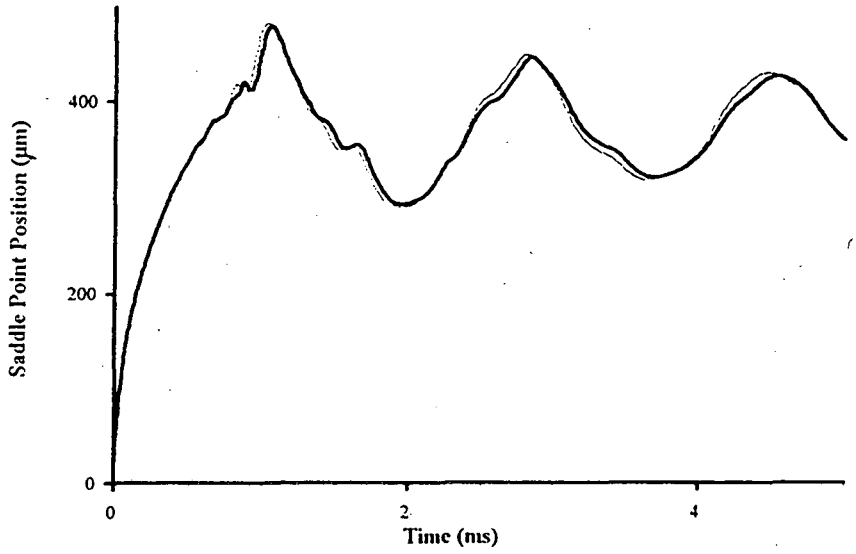

Figure 5-3. Simulation results: electrode location. Saddle-point motion of 600-μm bubbles coalescing in 1.1-cSt, 73-dyne/cm liquid with the electrode 0.24 (heavy line) and 11 (light line) bubble radii from the interface.

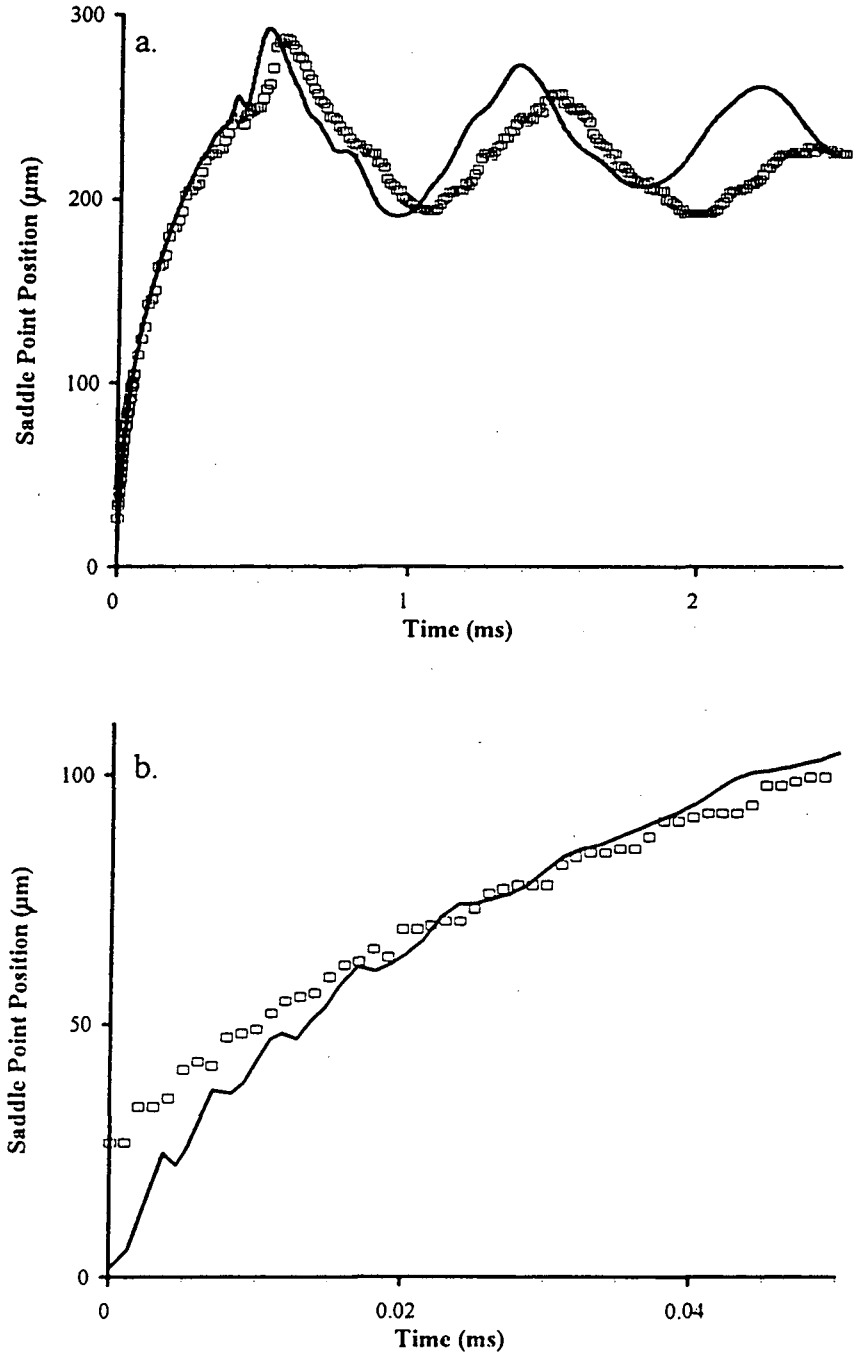

Figure 5-4. Computational (solid line) and experimental (□) results. (a) Saddle-point motion of 375-μm bubbles coalescing in 1.1-cSt, 73-dyne/cm liquid (1M H_2SO_4). (b) Expanded for short times.

The simulation captures the shoulders (shown as small peaks) superposed on the primary peaks that indicate the movement of surface waves through the saddle point region.

Figure 5-4(b) reveals three major differences between the computed and measured initial saddle-point motion. First, the computed curve begins near the origin, while the experimental data begin at a position of 27 μm. A possible explanation for this difference, given that the laser-beam waist has a finite width and the cusp is initially extremely narrow, is that the apparatus was unable to illuminate the saddle-point during the first several microseconds of its motion. Figure 5-5 illustrates how a 5-μm wide laser-beam sheet can affect the saddle-point position measurements of coalescing 375-μm bubbles. Since the beam intersects the interface at a point above the saddle-point location, the shadow position measured by the experimental apparatus could be above the actual saddle position, consistent with the difference between the results shown in figure 5-4. The error

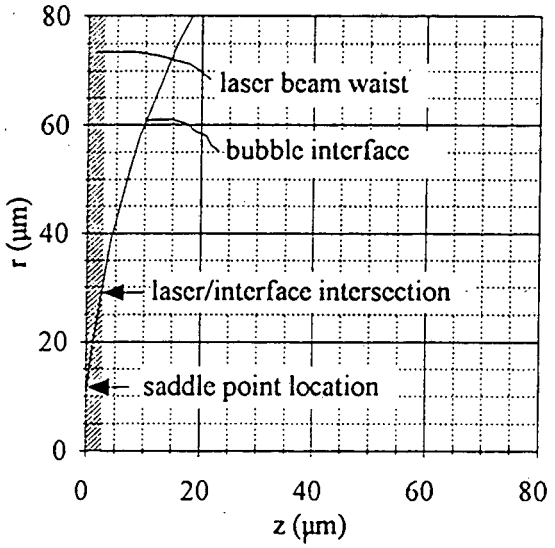

Figure 5-5. Illustration of laser constriction. A representation of a 5-μm wide laser beam sheet is superimposed on a portion of a 375-μm bubble interface.

introduced by constriction of the laser is expected to decay rapidly since the cusp opens as it moves. Using plots like figure 5-5 generated for each time step in the simulation, an estimate of the error caused by laser constriction was made. By adding the error introduced by a 5-μm beam waist to the computed position of the saddle-point of coalescing 375-μm bubbles, an adjusted curve for the motion of the saddle-point was generated and is presented with the experimental data in figure 5-6. Figure 5-6 demonstrates that the initial difference between the computed and measured saddle-point position could be caused by laser constriction. Differences after the first 5 microseconds are not likely to have been caused by this phenomenon. However, since the initial

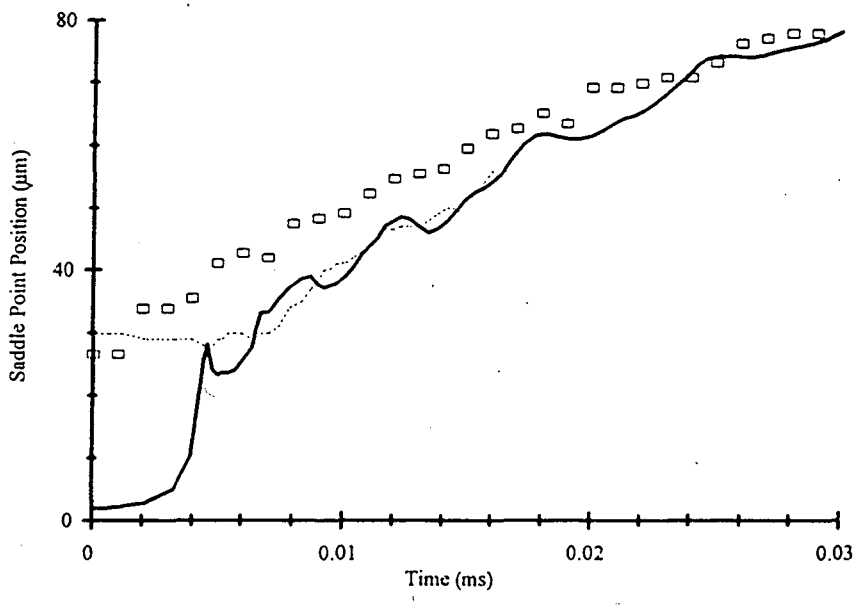

Figure 5-6. Estimated effect of laser constriction. Experimental data for 375-μm bubble coalescence (□) compared to simulation results (solid line) and simulation results modified to account for finite beam waist (dashed line). This graph shows that the laser beam did not illuminate the saddle-point initially because it was constricted between the surfaces of the bubbles.

velocities of the experimental saddle-point were probably affected by laser constriction, especially in the experiments with small bubbles, the accuracy of these results is limited.

The second difference between the computed and measured curves in figure 5-4 is that the measured saddle-point motion starts with a finite initial velocity. The acceleration of the initially stationary interface in the simulation occurs on a shorter time scale than the resolution capability of the experimental apparatus.

The third difference is the roughness of the computed curves compared to the measured curves. Simulations conducted using higher mesh densities and smaller time steps (not shown) had the same appearance. The roughness stems from small-amplitude surface waves superimposed on the large-scale motion of the cusp. The small waves damp within the first few dozen microseconds of the coalescence event.

C. Bubble Size, Kinematic Viscosity, and Surface Tension Results

Bubble size, liquid kinematic viscosity, and surface tension were independently changed from the conditions in figure 5-4 to produce the results shown in figures 5-7 through 5-9. Figure 5-7 shows that the overall form of the computed and measured results for coalescing 600-μm bubbles are similar and the oscillation period is the same. However, the computed results indicate a more rapid initial saddle-point deceleration, smaller amplitude oscillations, and a lower damping rate. The simulation calculated a damping rate of 0.23 ms^{-1}, compared the measured value of 0.40 ms^{-1}. Figure 5-8 shows that, when the liquid viscosity was increased, the deceleration, the damping rate, and the period were greater in the experiment than in the simulation. The computed period and damping rate

were 0.84 ms and 1.43 ms^{-1}, compared to the experimental results of 0.98 ms and 1.97 ms^{-1}, respectively. Figure 5-9 shows that the computed and measured saddle-point decelerations were the same while the computed oscillation damping rate was lower and the computed period was longer than observed experimentally when the surface tension was reduced. The simulation gave a period of 1.48 ms and a damping rate of 0.40, compared to the experimental results of 1.34 ms and 0.90 ms^{-1}, respectively. The high measured damping rate was most likely caused by bubble movement after coalescence. Adhesion was difficult to control in the large bubble experiments since buoyancy forces were high. If the coalescence plane of the newly formed bubbles moved toward the electrode with the highest adhesion after coalescence and away from the laser beam sheet, the apparent oscillation amplitude would be lower than the coalescence plane amplitude.

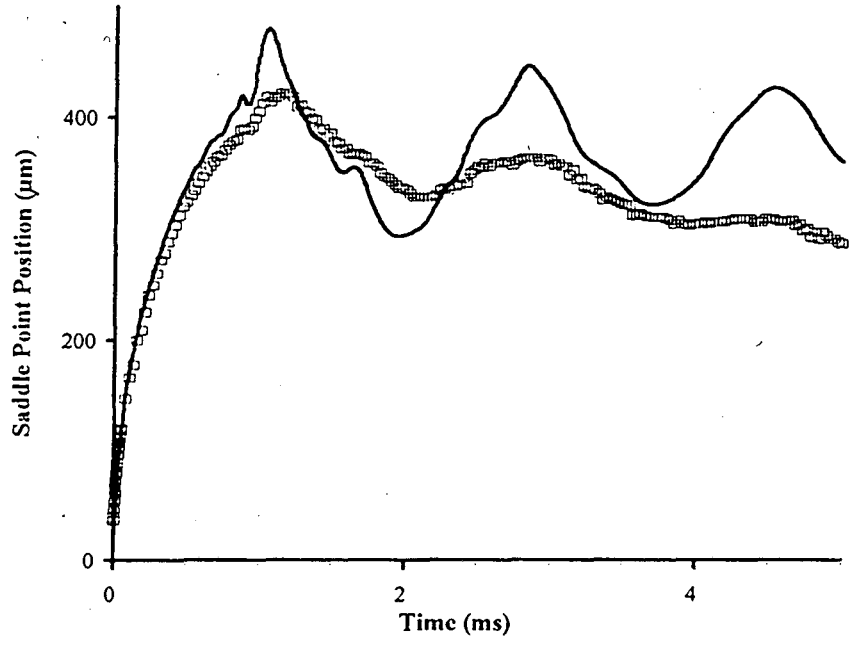

Figure 5-7. Bubble size. Computed (solid line) and measured (□) motion of the saddle-point of 600-μm diameter bubbles coalescing in 1.1-cSt, 73-dyne/cm liquid.

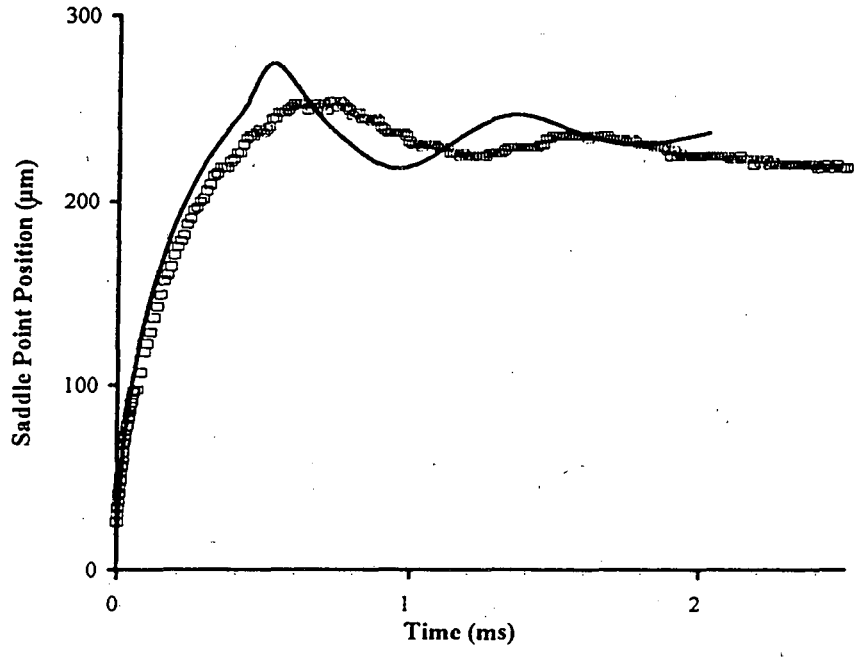

Figure 5-8. Kinematic viscosity. Computed (solid line) and measured (□) saddle-point motion of 375-μm bubbles coalescing in 5.0-cSt, 73-dyne/cm liquid.

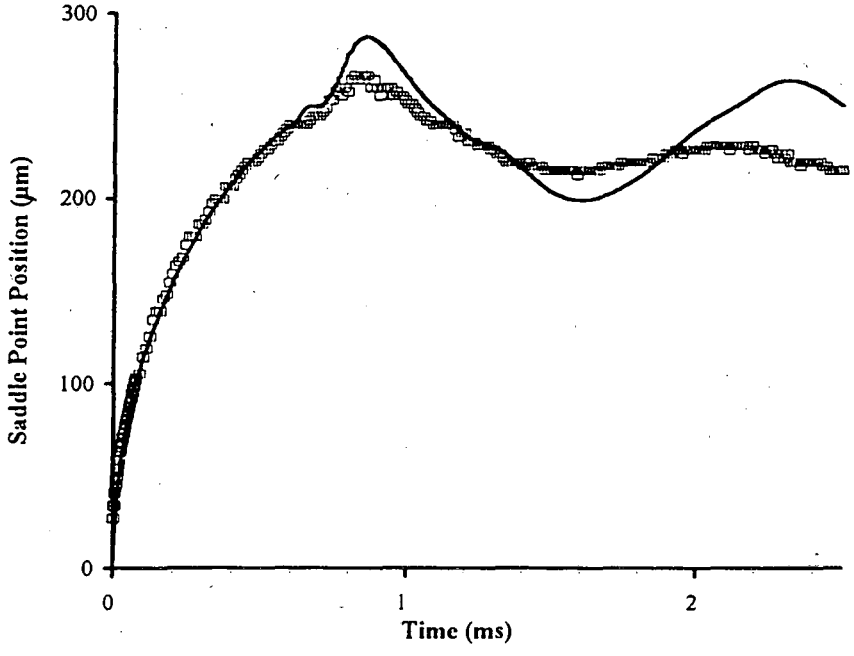

Figure 5-9. Surface tension. Computed (solid line) and measured (□) saddle-point motion of 375-μm bubbles coalescing in 1.1-cSt, 25-dyne/cm liquid.

D. Surface Tension Change Hypothesis

The differences between the computed and measured saddle-point decelerations and period suggest that the surface tension in the experiments may have changed from the values measured before each run. Kelsall[5] measured the change in bubble rise rates as a function of time after the seal on his system was broken and showed that exposure to the atmosphere causes a shift in bubble surface properties. Measurable changes in bubble rise rates were detected within an hour after exposure to the atmosphere. Levich[6] showed that the adsorption of surface-active particles on bubbles and drops retard their motion by up to 50% by immobilizing the interface. The amount of retardation depended on the surface concentration of absorbed species. Since the electrolytic cell used in the present study was open to the atmosphere, the surface tension could have changed with time. Small bubbles are affected to a greater degree by this mechanism than large bubbles because they have less surface area. Experiments conducted over long time periods are affected to a greater degree than those completed rapidly because of the increased exposure time.

To test the hypothesis that the surface tension in the experiments was actually lower than that of the pure electrolyte, the surface tension in the simulation was lowered until the computed period approximately matched the experimental data. The results for 150-μm bubbles are shown in figure 5-10. A surface tension of 49 dyne/cm gave computed results that matched both the experimentally determined oscillation period and the initial saddle-point deceleration of coalescing 150-μm bubbles. The results for 375 μm bubbles were fit with a surface tension of 60 dyne/cm (graph not shown) and the 600 μm bubble results were fit without changing the surface tension from the measured value

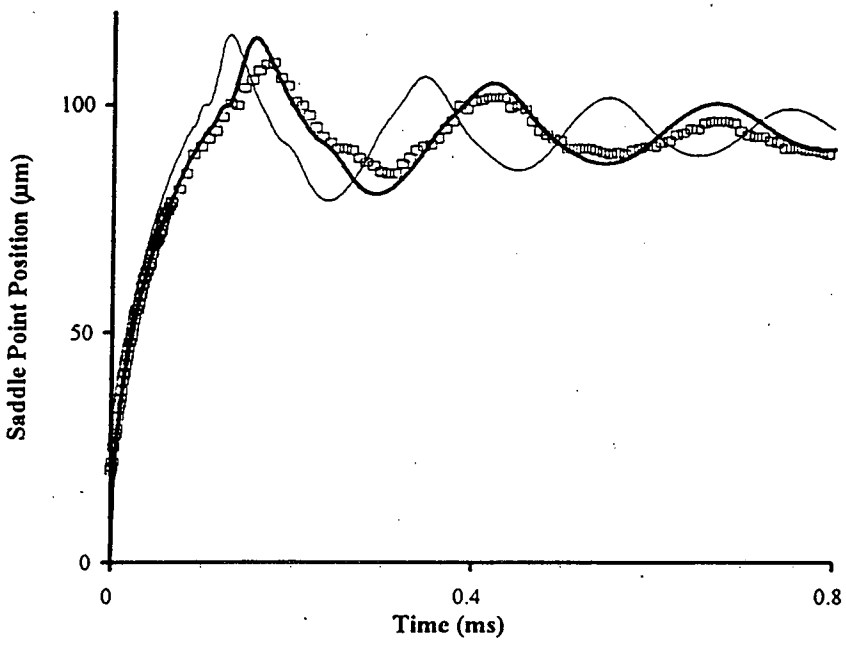

Figure 5-10. Experimental surface tension measurement. The experimental data of 150-μm bubbles coalescing in electrolyte with no additives (□) is compared with computed results with a surface tension of 49 dyne/cm (heavy line) and 73 dyne/cm (light line).

of 73 dyne/cm (see figure 5-7). Therefore, coalescence experiments with small bubbles were more susceptible to time-dependent surface tension changes than the experiments with large bubbles. Small bubbles were affected to a greater degree than large bubbles both because less surface-active material was required to alter their surface concentration, and because the experiments with small bubbles were conducted over time periods of several hours, while the experiments with large bubble were completed in less than one hour. Despite the good fit obtained, it is not clear that atmospheric contamination could cause a surface-tension change of this magnitude.

The computed saddle-point motion for the bubble sizes, electrolyte kinematic viscosities, and surface tensions examined in the experiments are given in Appendix IIc.

The results for the initial velocity, oscillation period, and damping rate are summarized in table 5-1. The initial velocities were calculated from the slopes of the saddle-point motion curves. Initial film thicknesses were estimated using the Culick relationship and the computed initial velocities. In the simulations, increasing the viscosity lowered the initial velocities. Since the Culick relationship does not take viscosity into account, the estimated film thicknesses in high-viscosity liquid, given in table 5-1, are quite high.

Table 5-1. Results: computed and measured values.

VARIABLES			MEASURED			COMPUTED			
single bubble diameter (μm)	surface tension (dyne/cm)	kinematic viscosity (cSt)	initial velocity (cm/s)	damp rate (ms^{-1})	period (ms)	initial velocity (cm/s)	damp rate (ms^{-1})	period (ms)	initial film thickness (μm)
600	73	1.1	342	0.40	1.78	317	0.23	1.77	14.6
600	25	1.1	321	0.40	2.7	195	0.17	2.92	13.4
600	73	5.0	400	0.70	1.89	128	0.63	1.68	89.7
375	73	1.1	360	0.54	0.94	389	0.48	0.86	9.7
375	25	1.1	336	0.90	1.34	258	0.40	1.48	7.6
375	73	5.0	284	1.97	0.98	184	1.43	0.84	43.4
150	73	1.1	350	2.8	0.252	584	2.40	0.21	4.3
150	25	1.1	210	3.6	0.408	330	2.28	0.36	4.7
150	73	5.0	195	20	0.25	196	8.40	0.21	38.3
50	73	1.1	187	14	0.057	1017	17.8	0.04	1.4

E. Scaling Analysis of Numerical Results

The experimental and computed coalescence results will be presented on scaled axis to show how the results depend on the parameters of the system. The oscillation damping rates, also given in table 5-1, are plotted in figure 5-11. The ordinate of figure 5-11 is the kinematic viscosity divided by the square of the resultant bubble radius according

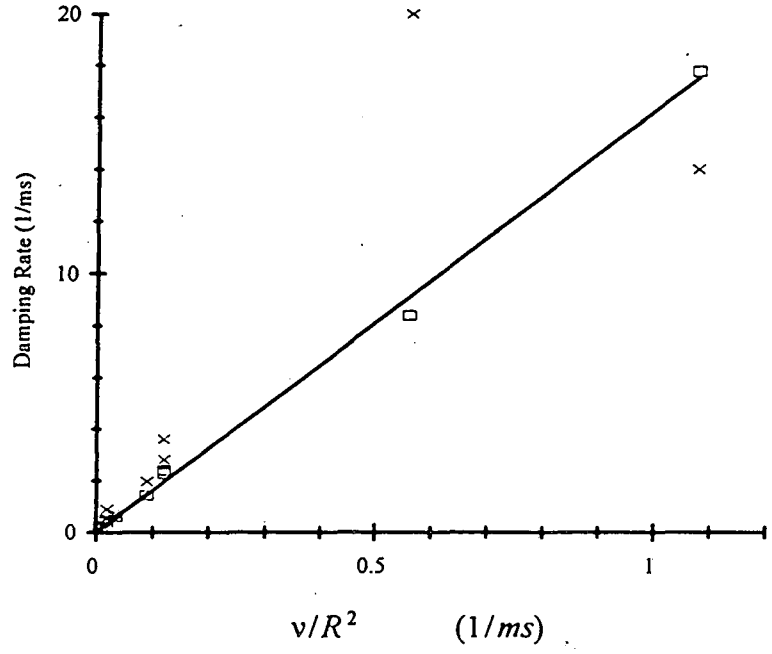

Figure 5-11. Oscillation damping rate scaling analysis. The data points were read from the computed saddle-point motion curves (□) and the experimental data (×) of 50- to 600-μm diameter bubbles coalescing in 1.1- to 5.0-cSt, 25- to 73-dyne/cm liquid.

to the harmonic oscillator equation. All the computed results and most of the experimental results fall on a straight line. The two experimental points that lie farthest from the line had the highest degree of experimental uncertainty. These results support the conclusions from the harmonic oscillator analysis, namely, that damping scales linearly with the viscosity, inversely with the square of the bubble radius, and does not depend on surface tension.

The computed and measured oscillation period are shown in figure 5-12. The combination of parameters used for the abscissa was derived in the harmonic oscillator analysis. In figure 5-12, all the data fall on a line that passes through the origin. This analysis shows that the period scales with the resultant bubble radius raised to the 3/2 power and inversely with the square root of the surface tension. Viscosity has no effect on

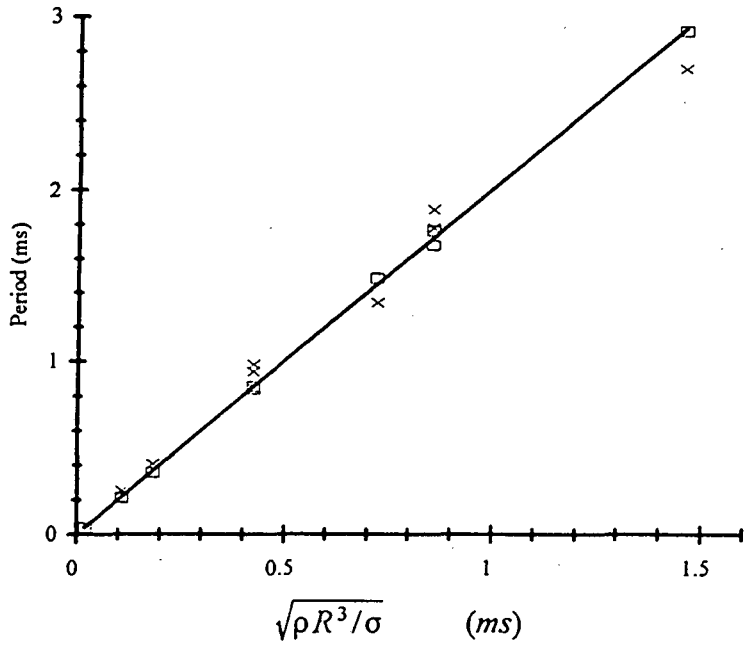

Figure 5-12. Oscillation period scaling analysis. The data points were read from the computed saddle-point motion curves (□) and the experimental data (×) of 50- to 600-μm diameter bubbles coalescing in 1.1- to 5.0-cSt, 25- to 73-dyne/cm liquid.

the period.

The computed initial velocities in 1.1-cSt kinematic viscosity liquid are plotted in figure 5-13 along with the experimental results. The ordinate was scaled with the surface tension and resultant bubble radius according to the Culick relationship, assuming a linear relationship between bubble radius and initial film thickness. The computed results for coalescence in 1.1-cSt liquid lie on a line that passes through the origin. The highest computed initial velocity was obtained for the smallest bubble size, contrary to the experimental results and the Culick relationship. A similar lack of fit was found for the results at higher viscosity. The computed relationship between bubble size and initial velocity seems physically reasonable because the smallest bubbles have the highest

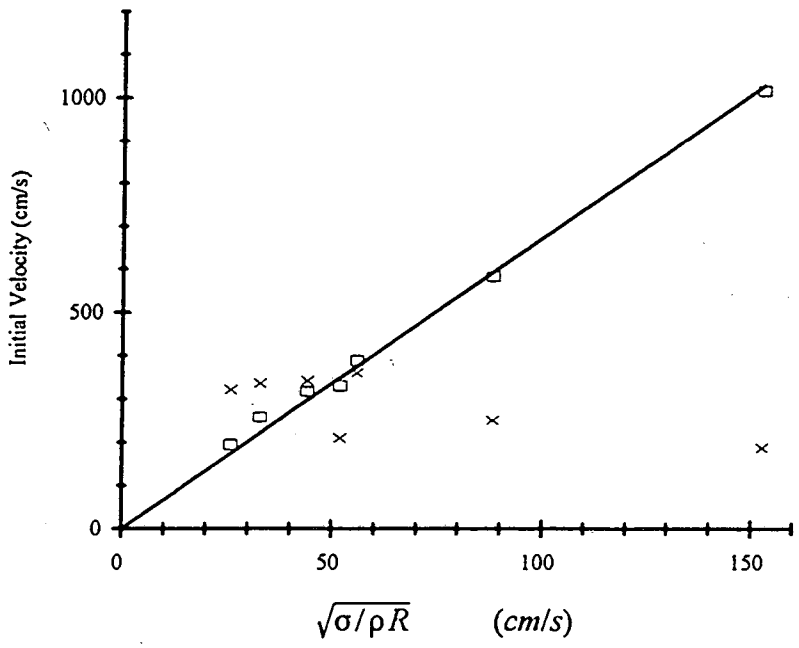

Figure 5-13. Initial velocity scaling analysis: computed (□, solid line) and measured (×) velocity in 1.1-cSt liquid. The computed initial velocities are fit with a linear regression line with a slope of 6.7.

curvature and, accordingly, the highest surface energy. However, the simulation does not fully explain the experimental results which indicates the complexity of the rupture of the liquid film. A more focussed analysis should be done to elucidate the phenomena that occur in the receding liquid film immediately following rupture.

The simulations provide two-dimensional images of the bubble interface. The series of frames in figure 5-14 shows graphically the shape of a portion of the interface with time after two 600-μm bubbles coalesce. The experimental data, shown in the frames as solid symbols, are in good agreement with the computed results for the interface near the coalescence plane. Surface waves are clearly visible. The large wave created by the initial motion of the cusp travels around the interface and eventually returns to the coalescence plane. The point of the interface that intersects with the coalescence plane

(the saddle-point) is accelerated rapidly by the wave just before it reaches the maximum displacement from the axis of symmetry. This sudden acceleration is clearly visible in the saddle-point motion curves. The frames in figure 5-14 demonstrate that the acceleration corresponds to the local deformation in the interface caused by a surface wave.

References

1. Perry's Chemical Engineers' Handbook, 50th Edition, Perry, R.H., Green, D.W., and Maloney, J.O., eds., McGraw-Hill, 1984, p. 5-62.

2. *ibid.*

3. Hopper, Robert W., "Coalescence of Two Equal Cylinders: Exact Results for Creeping Viscous Plane Flow Driven by Capillarity", Communications of the American Ceramic Society, p. C-262, December 1984.

4. FIDAP is a trademark of Fluid Dynamics International, Inc. 500 Davis St., Suite 600, Evanston, IL, 60201 (U.S.A.).

5. Kelsall, Geoff, J. Chem. Soc., Faraday Trans., *to be published.*

6. Levich, V.G., Physiochemical Hydrodynamics, Prentice-Hall, Englewood Cliffs, N.J., p.409, 1962.

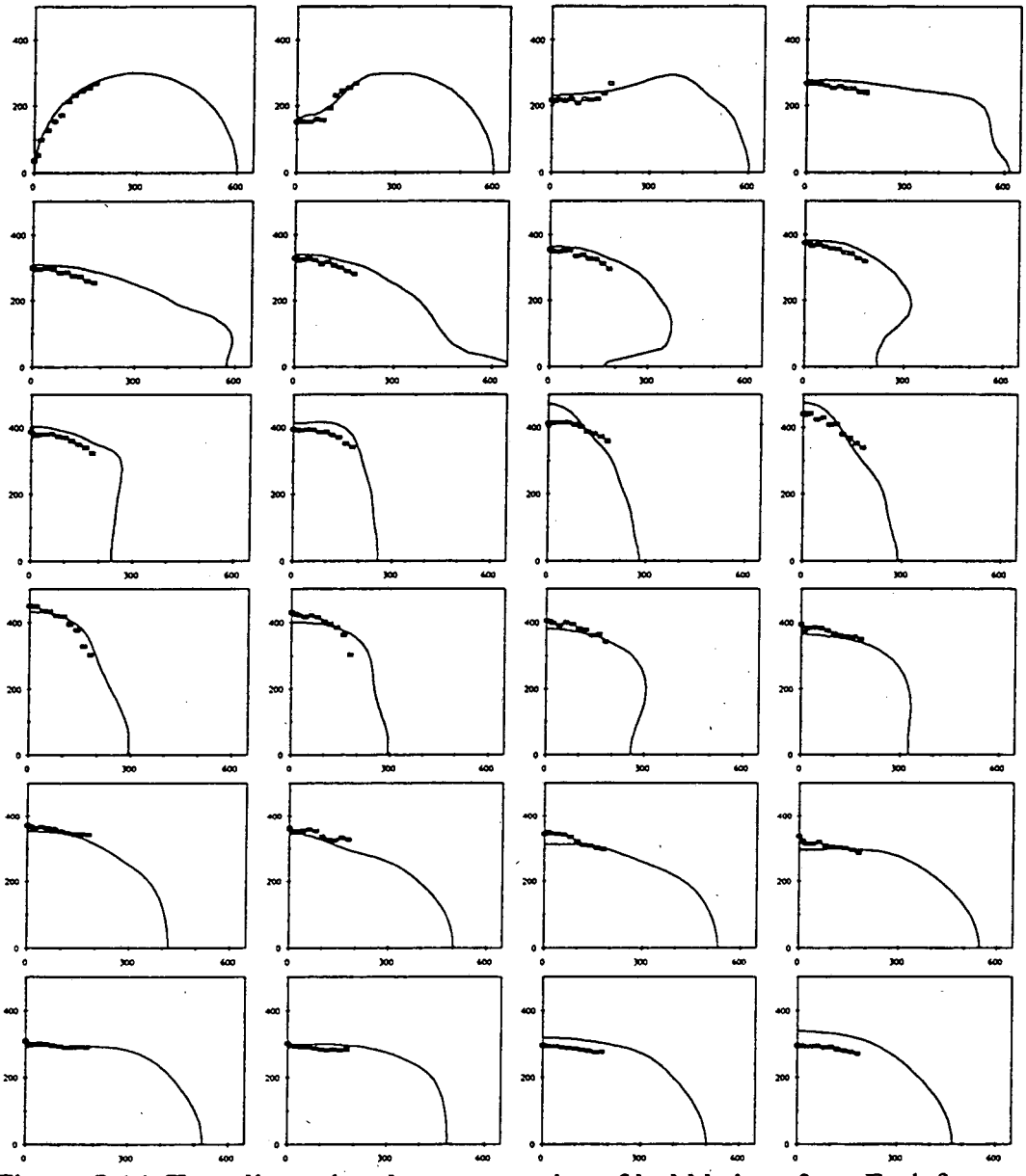

Figure 5-14. Two-dimensional representation of bubble interface. Each frame shows one quarter of the cross section of two 600-μm bubbles coalescing in 1.1-cSt, 73-dyne/cm liquid. One frame is shown for every 0.02 ms of elapsed time. Experimental data points are shown along with the computed line.

Chapter 6. CONCLUSIONS

The apparatus and procedures developed in this research permit the observation of electrolytic bubble coalescence, which heretofore has not been possible. The influence of bubble size, electrolyte viscosity, surface tension, gas type, and pH on bubble coalescence was examined. The Navier-Stokes equations with free surface boundary conditions were solved numerically for the full range of experimental variables that were examined.

Based on this study, the following mechanism for bubble coalescence emerges: when two gas bubbles coalesce, the surface energy decreases as the curvature and surface area of the resultant bubble decrease, and the energy is imparted into the surrounding liquid. The initial motion is driven by the surface tension and slowed by the inertia and viscosity of the surrounding fluid. The initial velocity of the interface is approximately proportional to the square root of the surface tension and inversely proportional to the square root of the bubble radius. Fluid inertia sustains the oblate/prolate oscillations of the resultant bubble. The period of the oscillations varies with the bubble radius raised to the 3/2 power and inversely with the square root of the surface tension. Viscous resistance dampens the oscillations at a rate proportional to the viscosity and inversely proportional to the square of the bubble radius. The period does not depend on the viscosity and damping does not depend on surface tension. Coalescence does not depend on gas type (electrode polarity) or electrolyte pH.

The numerical simulations were consistent with most of the experimental results. The differences between the computed and measured saddle point decelerations and periods suggest that the surface tension in the experiments may have changed during each

run. By adjusting the surface tension in the simulation until a good fit was obtained for the 150-μm diameter bubbles, a surface tension of 49 dyne/cm was obtained. This is substantially lower than the measured surface tension of 74 dyne/cm. The simulations fit the experiments on larger bubbles with very little adjustment of surface tension indicating that surface tension did not change to a significant degree in these runs. The simulations did not fully explain the initial velocity results which indicates the complexity of the rupture of the liquid film. A more focussed analysis should be done to elucidate the phenomena that occur in the receding liquid film immediately following rupture.

Both the simulations and the experiments show that surface waves are superimposed on the initial and oscillatory motion of the bubbles. These small-amplitude motions locally reduce the surface energy during a coalescence event. This energy dissipation can explain the disparity between the velocities predicted by the hole expansion theory of Charles and Mason and the measured velocities.

Saddle-point positions and velocities measured in this work are higher and more accurate than those reported by Egan and Tobias because of the improved experimental apparatus and procedures.

APPENDIX IA: LASER BEAM INTENSITY PROFILE

A beam profilometer was constructed and used to quantify the intensity of laser light near the surface of a bubble. The profilometer consisted of a photodiode with a 5-μm diameter aperture, a translating stage, a 5-rpm motor, and an x-y plotter. The photodiode was positioned in the laser beam near the shadow of a 600-μm diameter bubble as shown schematically in figure IA-1. The photodiode was moved at a constant velocity into the shadow as the intensity of the light was recorded.

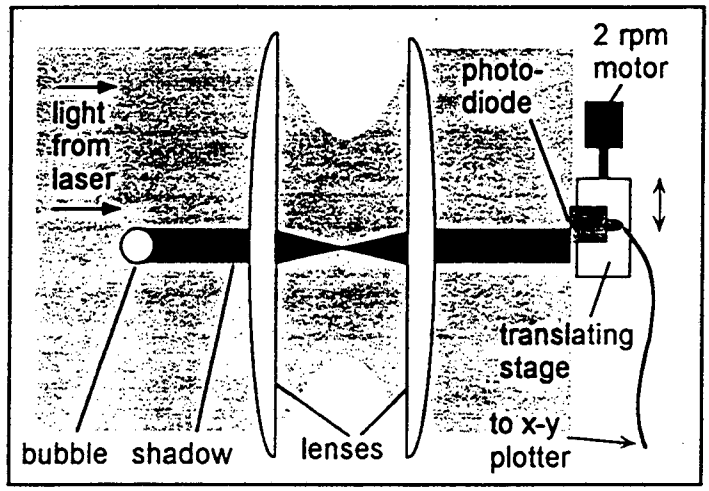

Figure IA-1. Schematic of Laser Profilometer.

The potential of the photodiode, when exposed to the beam, was measured relative to the potential measured in darkness as a function of time. The potential was converted to a light intensity assuming a linear relationship, with zero intensity corresponding to the potential measured in darkness. The time was converted to position by multiplying by the translational velocity of the motor and dividing by the known magnification. A sample profile for a 600-μm bubble in a 3-cm diameter beam is shown in figure IA-2.

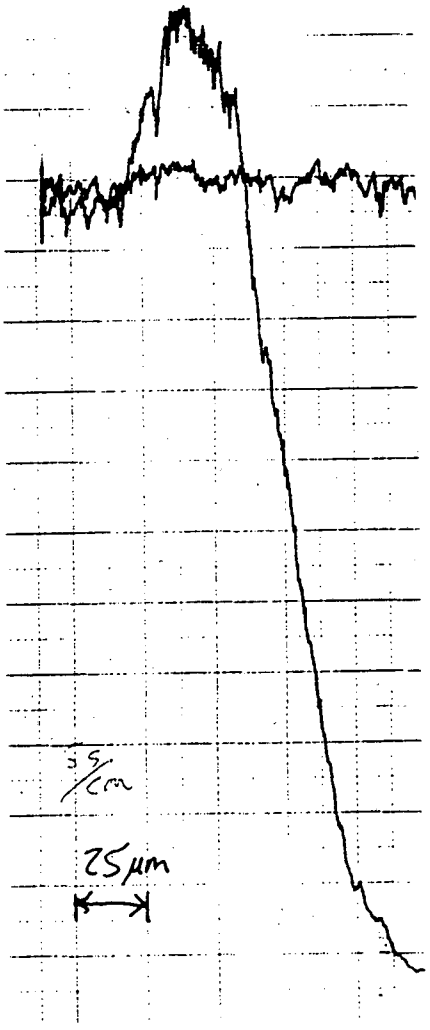

Figure IA-2. Sample of Laser Profilometer Data. Light intensity at edge of bubble superimposed on intensity without a bubble present.

The profile shown in figure IA-2 quantifies the precision with which the position of the bubble surface is detected. Because the light intensity decreases sharply over a distance of about 25 µm for a 600-µm diameter bubble, the apparatus can determine the surface positions to within +/- 4% of the bubble diameter.

APPENDIX IB: OPTICS DESIGN AND SET-UP PROCEDURE

Lens Selection – The variables that are important for lens selection are the focal length and magnification type (either 1-D or 2-D corresponding to a cylindrical or a spherical lens, respectively). Referring to the schematic of the laser optics setup shown in figure IB-1, the lenses used to modify the laser beam are the two beam-expander lenses, the beam-sheet lens, the magnification lens, and the compensating lens.

The *beam-expander lenses* expanded the beam to a diameter of 3.2 mm which provided a uniform light intensity over the distance of the largest event measured (the coalescence of two 600-μm diameter bubbles) without reducing the laser intensity below

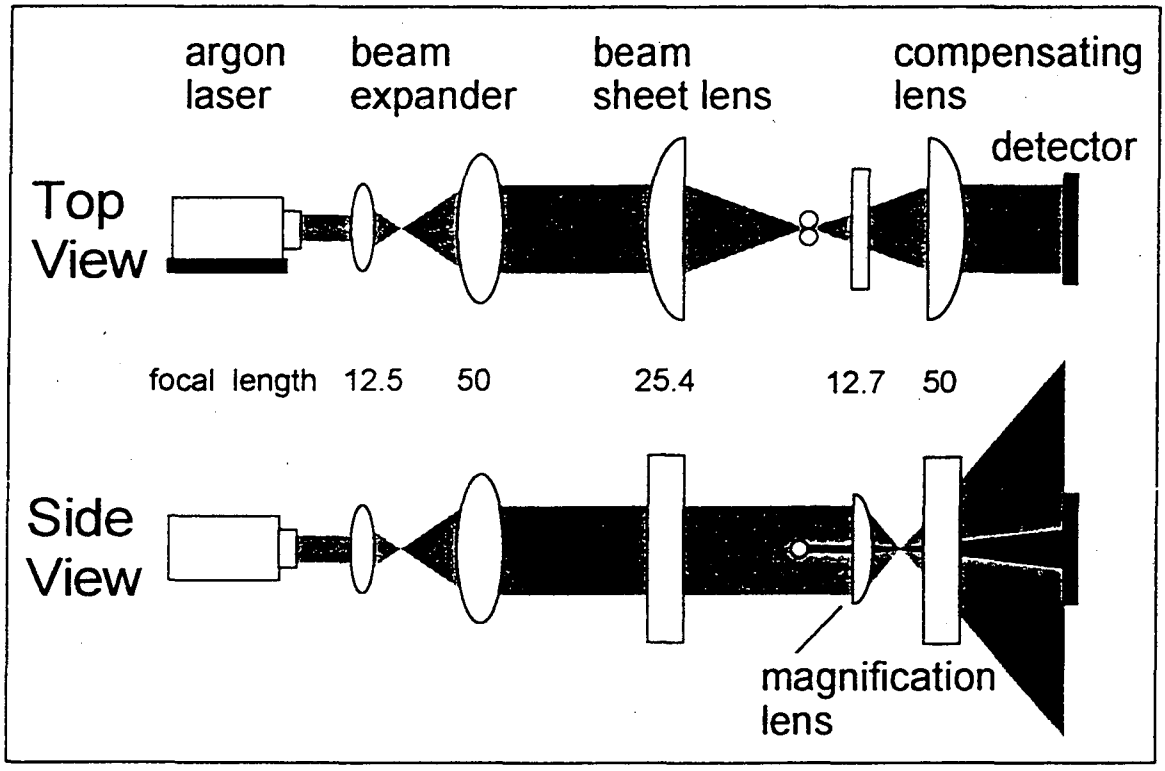

Figure IB-1. Schematic of laser projection optics.

the level required for detection (approximately 5 mW). Spherical achromatic lenses of 12.5- and 50-mm focal length were used. Since the beam from the laser diverged, the lenses were positioned to collimate the beam in addition to expanding it. The expansion factor of 3.8 was determined with the beam profilometer by measuring the beam diameter before and after the expander.

The beam expander was followed by the *beam-sheet lens* which reduced the beam to a narrow sheet of light. The width at the focal point was too small to measure with the beam profilometer. However, the beam width was estimated by the equation[1] :

$$2\omega = \frac{4\lambda f}{\pi D} \qquad (1)$$

where $2\omega \equiv$ width at the center of the focal field (beam waist),
$\lambda \equiv$ wavelength of the laser light,
$f \equiv$ lens focal length, and
$D \equiv$ diameter of the incoming beam

as illustrated in figure IB-2.

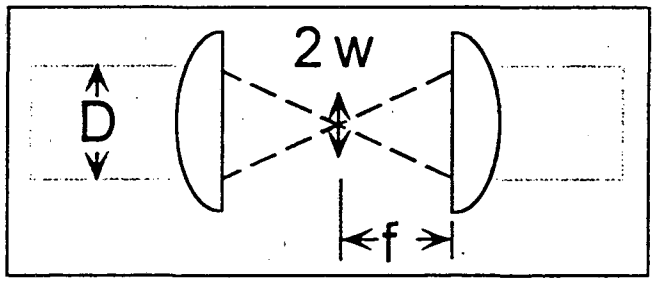

Figure IB-2. Laser Beam Focussing Variables.

The depth of focus (DOF) is the distance over which the beam width does not exceed the width at the waist by more than a factor of $\sqrt{2}$. DOF is estimated by[2] :

$$D.O.F. = \frac{8\lambda}{\pi}\left(\frac{f}{D}\right)^2 \qquad (2)$$

In general, a narrow beam waist and a long DOF are desirable. However, both beam waist and DOF decrease with decreasing focal length, necessitating a compromise. The beam waist and DOF in the experiments were optimized for each bubble size by selecting beam sheet lenses according to their focal lengths. The lens with a 25.7-mm focal length shown in figure IB-1 provided an estimated beam waist of 5 μm and a DOF of 80 μm, which were adequate for 150-to 375-μm diameter bubbles. For experiments with 600-μm diameter bubbles, the 50-mm beam sheet lens provided a beam waist of 10 μm and a DOF of 305 μm. For 50-μm diameter bubbles, a 12.4-μm beam sheet lens was used, giving a beam waist of 2.4 μm and a DOF of 19 μm.

The next lens in the sequence was the *magnification lens* which is used to project the image of the coalescing bubbles onto the photodiode array. Magnification was required only in the vertical direction so a horizontally oriented cylindrical lens was employed. A short-focal-length magnification lens maximizes the resolution by maximizing the magnification. However, the range of focal lengths was restricted by the physical constraints placed on the image and object distances. The closest approach of a lens to the bubbles, the minimum image distance, was 10 mm, because of the dimensions of the electrolytic cell. The maximum object distance was 2 meters, which is established by the size of the optics table used for the experiments. Achieving magnifications of 20 to 300 under these constraints led to the selection of a 12.7-mm lens for all bubble sizes except for the smallest (50-μm diameter) bubbles, for which a special cell was constructed to

permit use of a 6.35-mm magnification lens. In addition, a pair of mirrors, placed near the detector and the magnification lens, was used to triple the image distance without exceeding the available space.

The final lens in the sequence, the *compensating lens*, collected the light diverging from the beam sheet lens and projected it onto the detector. The criteria for selecting the compensating lens were that the beam not change in the vertical direction, that it be positioned relatively far from the cell to not interfere with the magnification lens, and that it focus most of the beam onto the 5-mm wide detector elements. A 50-mm focal length cylindrical lens adequately accomplished all of these objectives.

Lens, Cell, and Detector Positioning – The positions of the laser, lenses, electrolytic cell, and detector were fixed relative to each other by bolting all the components of the apparatus onto a Newport optics table. The lenses were placed in holders that slide on an optics bar attached to the table. The cell was mounted on a 3-axis stage which was bolted onto the optics table and cantilevered over the optics bar.

The optical alignment procedures, which were conducted with the laser on at reduced power, were developed for accurate and reproducible positioning of the lenses and the electrolytic cell. The sequence that was developed assured that the image projected onto the detector was focussed in both the horizontal and vertical directions.

The first beam-expander lens was placed such that the beam passed through its center point. The beam-expander second lens was placed so that the beam was columnated, i.e.: neither converging nor diverging, and focussed onto the detector.

Columnation is essential for accurate magnification. Columnation was checked by diverting the beam with a number of mirrors at opposite ends of the room and examining the spot size along the beam path over a distance of approximately 50 feet.

Next, the detector was positioned so that the distance between the cell and the detector was the sum of the object and image distances as calculated with equations (1) and (2).

The remaining steps of the procedure were conducted with the gas bubbles attached to the microelectrodes. A pair of bubbles was grown until they nearly coalesced and they were illuminated by the laser beam. The bubbles were approximately aligned relative to each other by adjusting the position of the mobile electrode relative to the fixed electrode until they were aligned on the video monitor. The magnification and compensation lenses, which are affixed to sliding mounts, were placed on the optics bar and the lens positions were adjusted until a sharply focussed image of the bubbles was obtained on the face of the detector. Bubble alignment was then fine tuned.

The beam sheet lens was placed onto the optics bar in front of the cell such that the image of the bubbles on the detector was reduced to an arbitrarily narrow vertical line. A photodiode cell, the same one used for the beam-profile measurements, was placed in the beam path between the detector and the compensating lens. The bubbles were then grown very close to the point of coalescence. Although it was impossible to accurately measure the thickness of the liquid film separating the bubbles with this apparatus, a film thickness less than the width of the beam waist (approximately 5 μm) was desired. The position of the beam sheet lens was then adjusted until a maximum beam intensity was

measured with the photodiode cell which occurs at a location for which the maximum light passed between the bubbles. It was assumed that the beam waist was then positioned at the mutual axis of the bubbles.

The final adjustment in the optics setup was to adjust the detector sensitivity and laser intensity. The detector sensitivity was determined by setting the reference voltage in the detector circuitry. Because the reference-voltage adjustment screw was not indexed, a setting in the center of its range was selected and maintained throughout the experiments. The laser intensity was decreased from full power to the point where the detector triggered and then increased by approximately 5 mW. This intensity rendered the detector adequately sensitive while reducing the incidence of false triggers stemming from either slight fluctuations in the power supply or the presence of dust in the beam path.

APPENDIX Ic: ELECTROLYTIC CELL CONSTRUCTION

The electrolytic cell was designed to hold opposing, glass-encased microelectrodes in the aqueous electrolyte. The electrodes were fabricated by suspending a 127-μm diameter platinum wire inside a 0.5-cm o.d. glass tube and melting the glass to form a seal around the wire. The melted region was cut and the exposed faces were polished to a mirror finish using a Buehler metallurgical wheel with a pressure sensitive adhesive-backed nylon polishing cloth, Metadi diamond polishing compounds, and Buehler polishing oil. The electrodes were held perpendicular to the wheel in a 7-cm square jig made of acrylic resin. Polishing compounds with 5-, 1-, and 0.25-μm diamond particle sizes were used in sequence. The smoothness of the surface was checked optically using a microscope at 200 magnification. It was found by trial and error that if excessive heat is produced during the polishing procedure, the platinum wire tip was recessed in the glass tube. This occurs because platinum expands more than glass and, while it was flush with the glass surface while hot, it then recessed upon cooling. Polishing was conducted gradually with a constant flow of oil to minimize heating. Each electrode required about 30 minutes to polish. The oil and polishing compounds were removed by washing the electrodes in a flowing stream of deionized water followed by soaking and rinsing in the electrolyte.

The glass served as an insulation around the conducting platinum wires. Glass was selected rather than another insulator (such as epoxy) because of its hydrophilicity. The early prototype electrodes made with wires embedded in epoxy did not function properly because the bubbles stuck to the epoxy and accumulated, eventually obscuring both the

laser and microscope optics. On the other hand, the bubbles easily detached and floated away from the glass-encased electrodes after coalescence, and did not interfere with the observation or generation of subsequent bubble pairs. Platinum was used as the conductor since it is inert in the electrolyte and in the operating potential range of this work. Furthermore, platinum is a good electrocatalyst for both hydrogen and oxygen evolution.

The other ends of the platinum wires inside the glass tubes were connected to heavy, insulated copper wires with silver solder. Five-minute epoxy was used to seal the wire into the glass tubes. The electrode and copper wires were wrapped with a few turns of Teflon plumbing tape near their juncture at the back of the electrode. The copper wires were threaded into plexiglass electrode holders machined to fit tightly around the electrodes and the Teflon tape. The slight compressibility and hydrophobicity of the Teflon effectively sealed the copper wire and the back of the electrode from the electrolyte.

The fixed electrode holder (the left one in the schematic, figure IB-1) was held in place in the cell with a Viton o-ring. The mobile electrode holder was attached to a 3-axis stage with micrometer positioners (not shown in the schematic). The electrodes were, therefore, fully adjustable relative to each other. The entire cell, including the 3-axis stage for the mobile electrode holder, was mounted on a second 3-axis stage which was, in turn, bolted onto the optics table. The second stage, also equipped with micrometer positioners, allowed accurate positioning of the cell relative to the laser beam. Brackets and supports for the cell and stages were machined from aluminum.

The requirements for the focal length of the optics placed constraints on two of the dimensions of the cell. The distance from the bubbles to the second optical flat in the laser

path was less than the 12.7-mm focal length of the laser magnification lens. The distance from the angled plexiglass top plate to the bubbles was less than the 15-mm focal length of the microscope objective lens.

APPENDIX ID: VISCOSITY AND SURFACE TENSION OF ELECTROLYTE SOLUTIONS

Introduction – Sulfuric acid solutions with a range of surface tensions and viscosities were prepared for investigations of the coalescence of electrolytically generated hydrogen and oxygen bubbles. The kinematic viscosity and surface tension were controlled independently by adding selected compounds to 1M H_2SO_4. Dextran, a polysaccharide, was added at concentrations up to 9 wt% to increase the kinematic viscosity of 1M H_2SO_4 from one to five centistokes. 2-hexanol was added at concentrations up to 0.1 M to lower the surface tension of the sulfuric acid solution from 73.5 to 25 dyne/cm.

Viscosity – The kinematic viscosity was measured as a function of dextran concentration. Dextran is electrochemically inert and had no significant effect on the surface tension in the concentration range of interest. It also showed Newtonian behavior at shear rates from 1 to 100 s^{-1} measured on a Rheometric RFS-8500 rheometer. The amount of dextran added was determined by the equation:

$$Grams\ of\ dextran\ added = \frac{(\%)(Ml)}{(100\%)} \qquad (3)$$

where % ≡ dextran weight percent
Ml ≡ base electrolyte weight (in grams)

The viscosity was measured with a Cannon-Ubbelohde size 100 capillary viscometer. Drop times were on the order of one to five minutes. Ten drop times were

measured for each solution. The average time was then multiplied by a constant of 0.01603 cSt/s to determine the kinematic viscosity.

Dextrans with molecular weights of 500,000, 70,000, and 40,000 grams per mole were used. The viscosity was obtained at five to seven different concentrations for each type of dextran. The viscosity versus concentration for various molecular weights of dextran in acid and for dextran in water are plotted in figure ID-1.

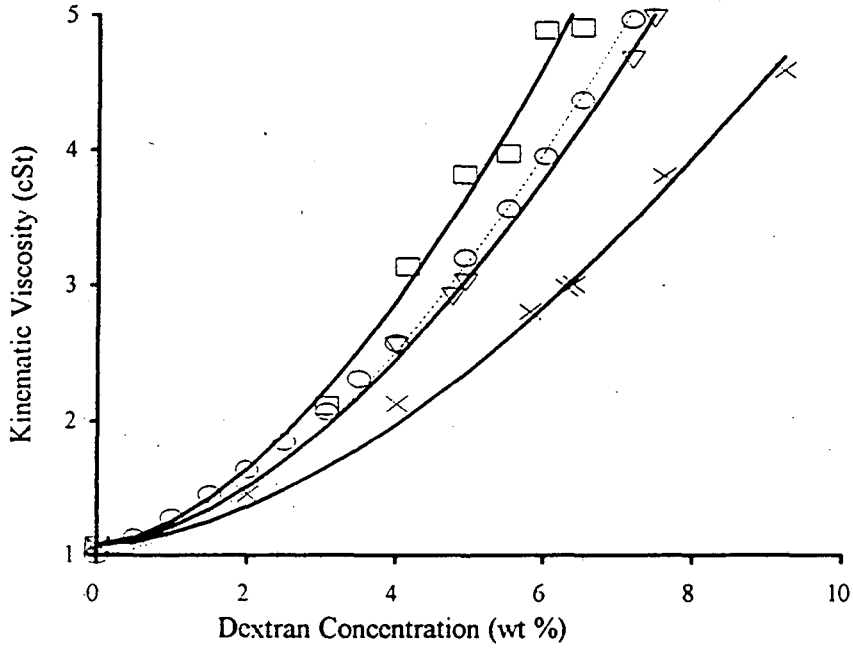

Figure ID-1. Kinematic Viscosity of Aqueous Dextran. Measured kinematic viscosity of 40,000 mol. wt. (×), 70,000 mol. wt. (▽), and 500,000 mol. wt. (□) dextran in 1M H_2SO_4 and literature values for 72,000 mol. wt. dextran (○) in water[3]. Data are shown with best-fit curves.

Least squares fit of power laws to the experimental data yielded the following functions for kinematic viscosity (ν) in cSt versus concentration:

72,000 g/mol dextran in water	$\nu = 1.00 + 0.150\,(\%)^{\frac{5}{3}}$	(4)
500,000 mw dextran in 1M H_2SO_4	$\nu = 1.07 + 0.179\,(\%)^{\frac{5}{3}}$	(5)

70,000 mw dextran in 1M H_2SO_4 $\quad \nu = 1.07 + 0.137\,(\%)^{\frac{5}{3}}$ (6)

40,000 mw dextran in 1M H_2SO_4 $\quad \nu = 1.07 + 0.090\,(\%)^{\frac{5}{3}}$ (7)

A gradual decrease in viscosity with time was observed in the 1M H_2SO_4 solutions. It is suspected that the dextran slowly reacts with the acid. The rate of reaction varied with the molecular weight of dextran. A five percent decrease in viscosity was observed for the 500,000 g/mol dextran in about one day. A similar decay for the 70,000 g/mol and 40,000 g/mol took 3 and 10 days, respectively. Based on this information, the 40,000 g/mol dextran was deemed the most suitable for this application. The experimentally measured kinematic viscosities in 1M H_2SO_4 containing 40,000 molecular weight dextran solutions are plotted along with equation (7) in figure ID-2.

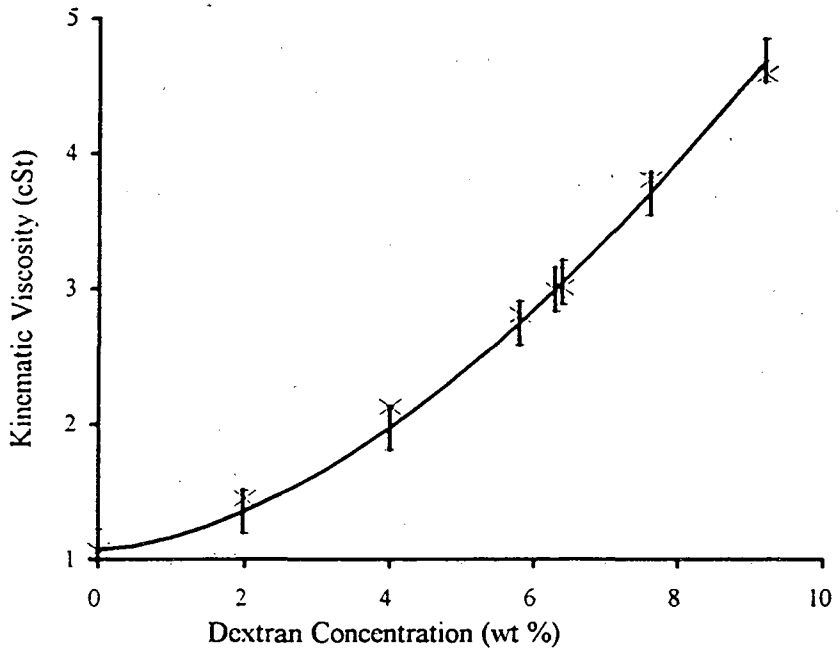

Figure ID-2. Kinematic viscosity of 1M H_2SO_4 as a function of 40,000 molecular weight dextran weight percent. Experimental results are presented with best-fit equation.

The primary source of is attributed to the variation in ambient temperature of ±4°F. Based on tabulated data for pure water[3], a four-degree temperature variation results in a kinematic viscosity variation of ±0.05 centistokes. This variation is indicated in figure ID-2 by the error bars.

Surface tension – The equation used to determine the concentrations of 2-hexanol for the experiments was

$$V_c C_c = V_d C_d \tag{8}$$

where V_c ≡ volume of pure 2-hexanol
V_d ≡ volume of dilute solution
C_c ≡ concentration of 2-hexanol (7.84 M)
C_d ≡ concentration of hexanol desired.

The concentrations of 2-hexanol (0.001 to 0.1 M) were sufficiently low enough that properties other than surface tension were not significantly affected, but high enough to facilitate easy rinsing of the apparatus used. Also over this range of concentrations, 2-hexanol is relatively nonvolatile, soluble, and electrochemically inert for our purposes.

The surface tension was determined with a Wilhelmy plate apparatus which consist of a Roller-Smith precision balance and a pure platinum plate from Biolar Corporation. The plate was suspended in air and the weight recorded, then it was slowly lowered into the solution until the bottom edge just touched the surface. The solution then pulled on the plate by capillary action. The weight in air was then subtracted from the weight when the liquid was pulling on the plate. The Wilhelmy plate was then cleaned by rinsing in distilled water and held over a flame until it glowed red. 10 or 11 measurements were averaged for

each solution. The weight was then multiplied by a constant which yielded the surface tension. The value of the constant, 0.98/2L, where L is the length of the plate, was determined by calibration using de-ionized water with a surface tension of 72.4 dynes/cm at room temperature. The constant 0.98/2L was determined to be 0.23 dynes/cm.

The surface tension was measured for ten different concentrations of 2-hexanol. The data were approximately fit with the following function:

$$SURFACE\ TENSION = 59.3 - 65.4(X - 0.0008)^{\frac{1}{4}} \qquad (9)$$

Here, X is the 2-hexanol concentration (M). The surface tension for 2-hexanol in 1M H_2SO_4 is shown along with equation (9) in figure ID-3. Also shown are surface tension data for n-hexanol in water from Hommelen[4].

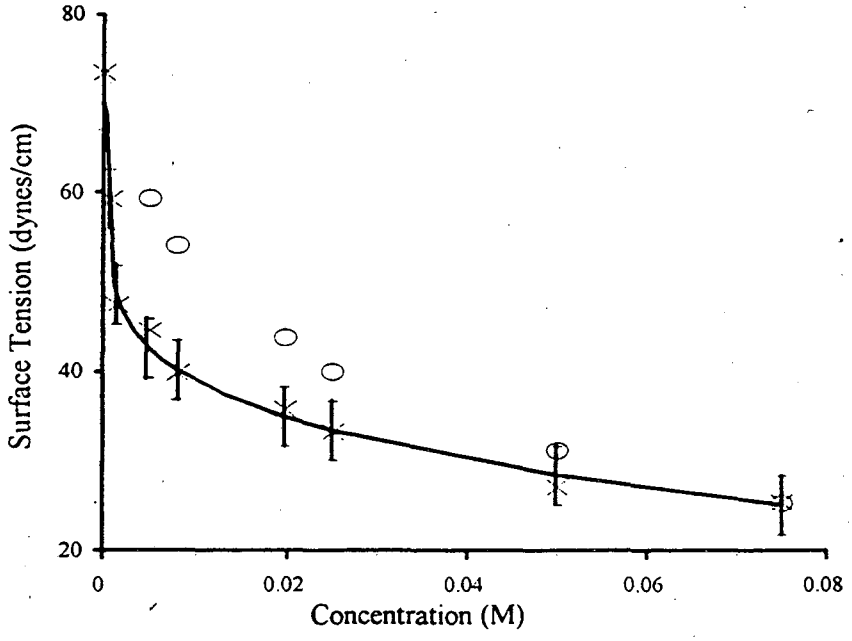

Figure ID-3. Surface tension of 1M H_2SO_4 as a function of hexanol concentration. Experimental results (×) and best-fit equation are compared with literature results for aqueous n-hexanol (○).

The primary source of error is attributed to a slight deformation of the Whilhelmy plate. This altered the surface tension constant, which is a function of the wetted perimeter. A maximum deformation of 1 millimeter in the wetted perimeter yielded an error in surface tension of ±3.3 dyne/cm. This variation is indicated by the error bars in figure ID-3.

References

1. Melles Griot Laser & Instruments Guide, Melles Griot, 1994, pp. A. 14-16.
2. *ibid.*
3. CRC Handbook of Chemistry and Physics, 64th edition, Robert C. Weast ed., CRC Press Inc., Boca Raton, FL, p. D-231, 1984.
4. Hommelen, J. J. Coll. Sci., v14, p. 385, 1959.

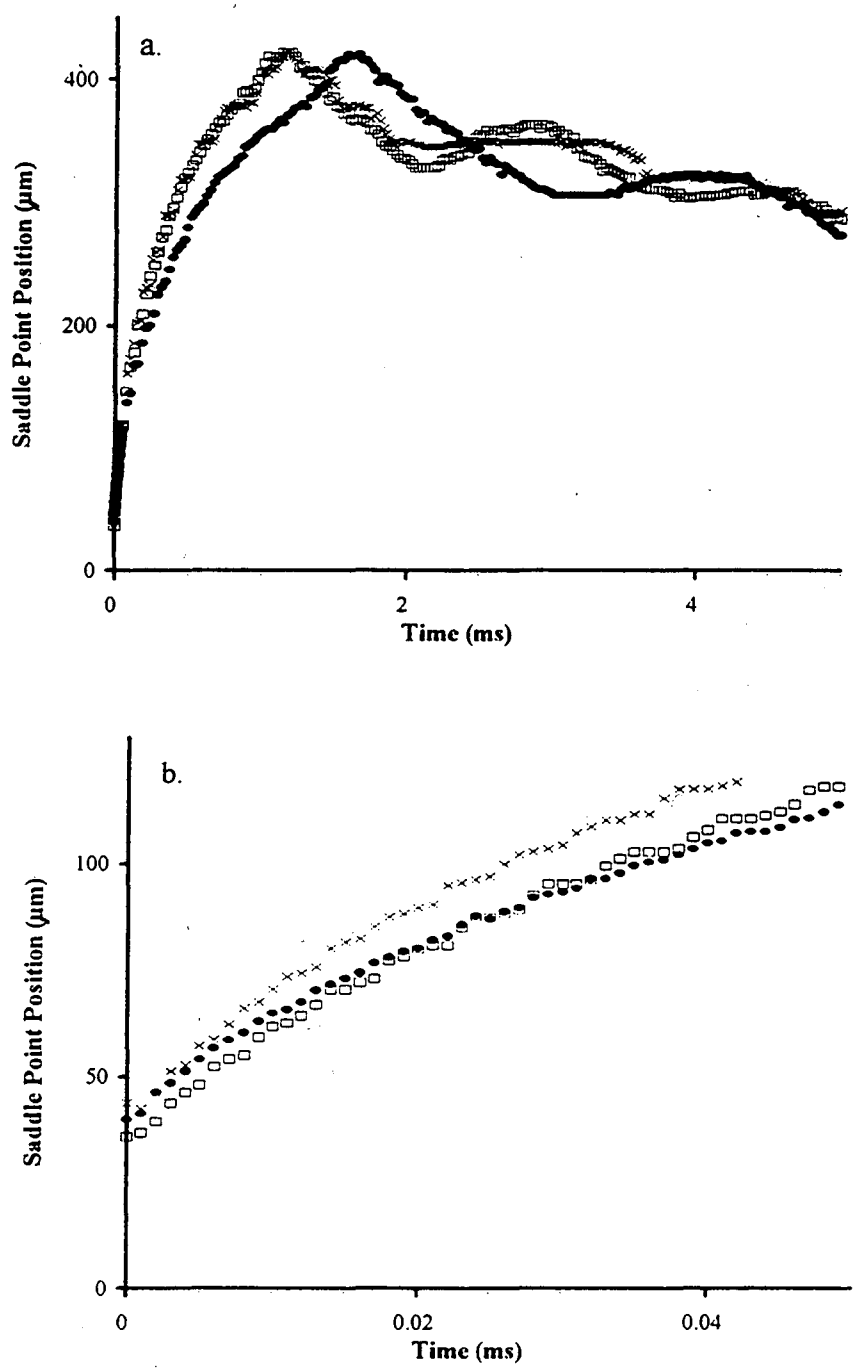

Figure IIA-1. Surface tension, 600-μm dia. hydrogen bubbles. (a) Saddle-point motion in 1M H_2SO_4 with 0.07M n-hexanol (●, σ = 25 dyne/cm), with 0.001M n-hexanol (×, σ = 49 dyne/cm), and without alcohol (□, σ = 73 dyne/cm). (b) Expanded scale for short time.

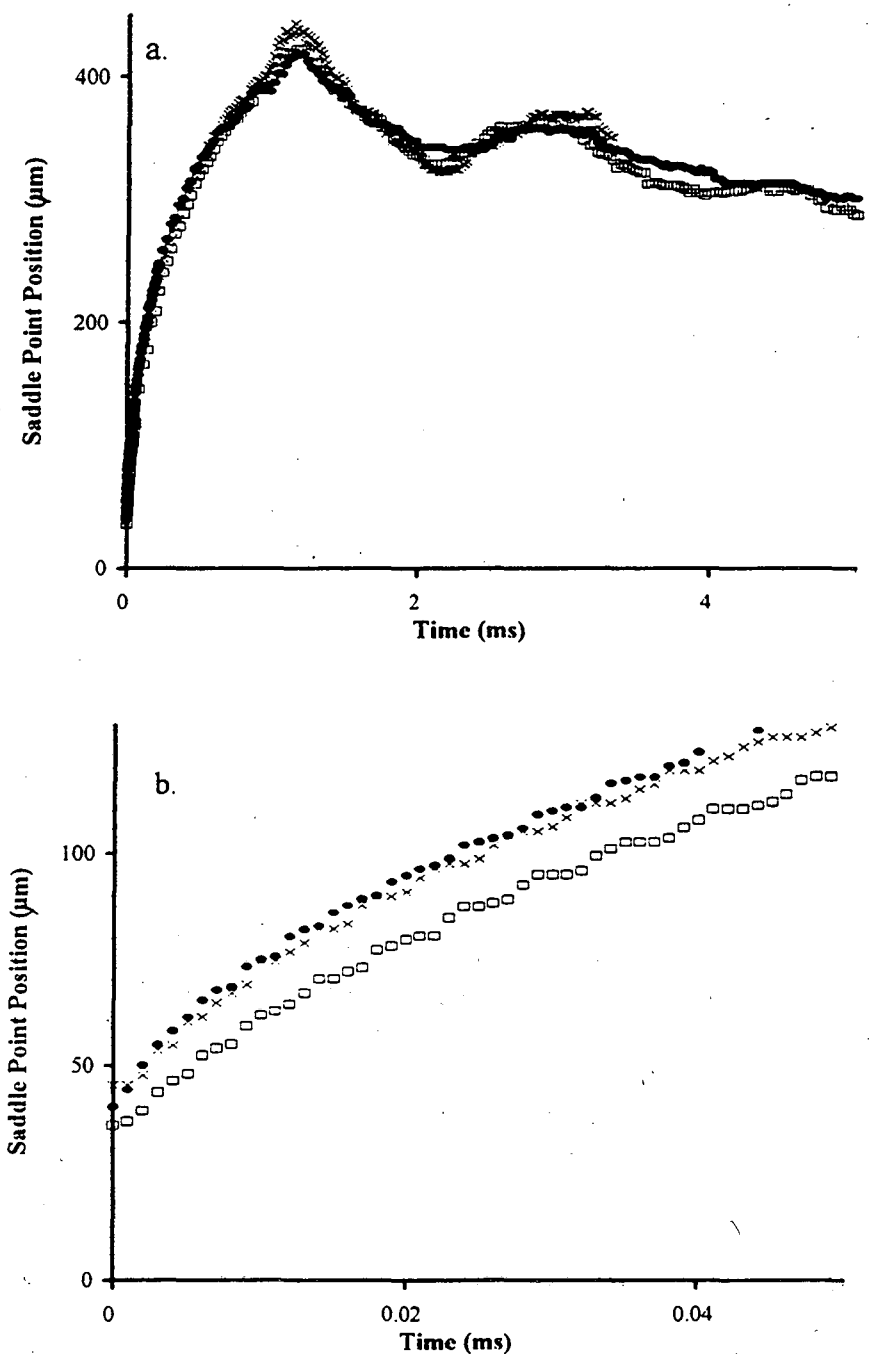

Figure IIA-2. Kinematic viscosity, 600-μm dia. bubbles. (a) Saddle-point motion in 1M H_2SO_4 with 10 wt% dextran (●, ν = 5.0 cSt), with 6 wt% dextran (×, ν = 3.0 cSt), and without dextran (□, ν = 1.1 cSt). (b) Expanded scale for short time.

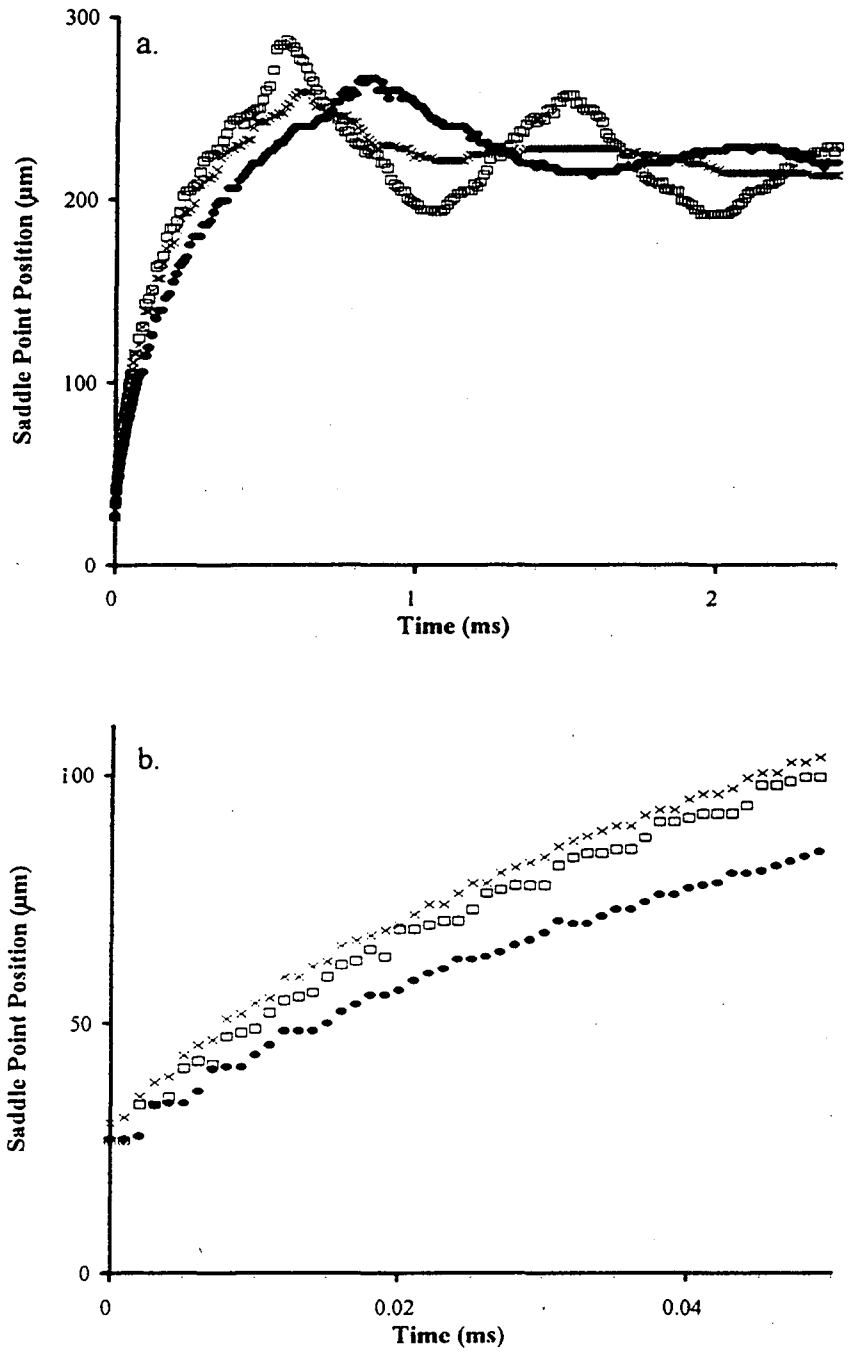

Figure IIA-3. Surface tension, 375-μm dia. bubbles. (a) Saddle-point motion in 1M H_2SO_4 with 0.07M n-hexanol (●, σ = 25 dyne/cm), with 0.001M n-hexanol (×, σ = 49 dyne/cm), and without alcohol (□, σ = 73 dyne/cm). (b) Expanded scale for short time.

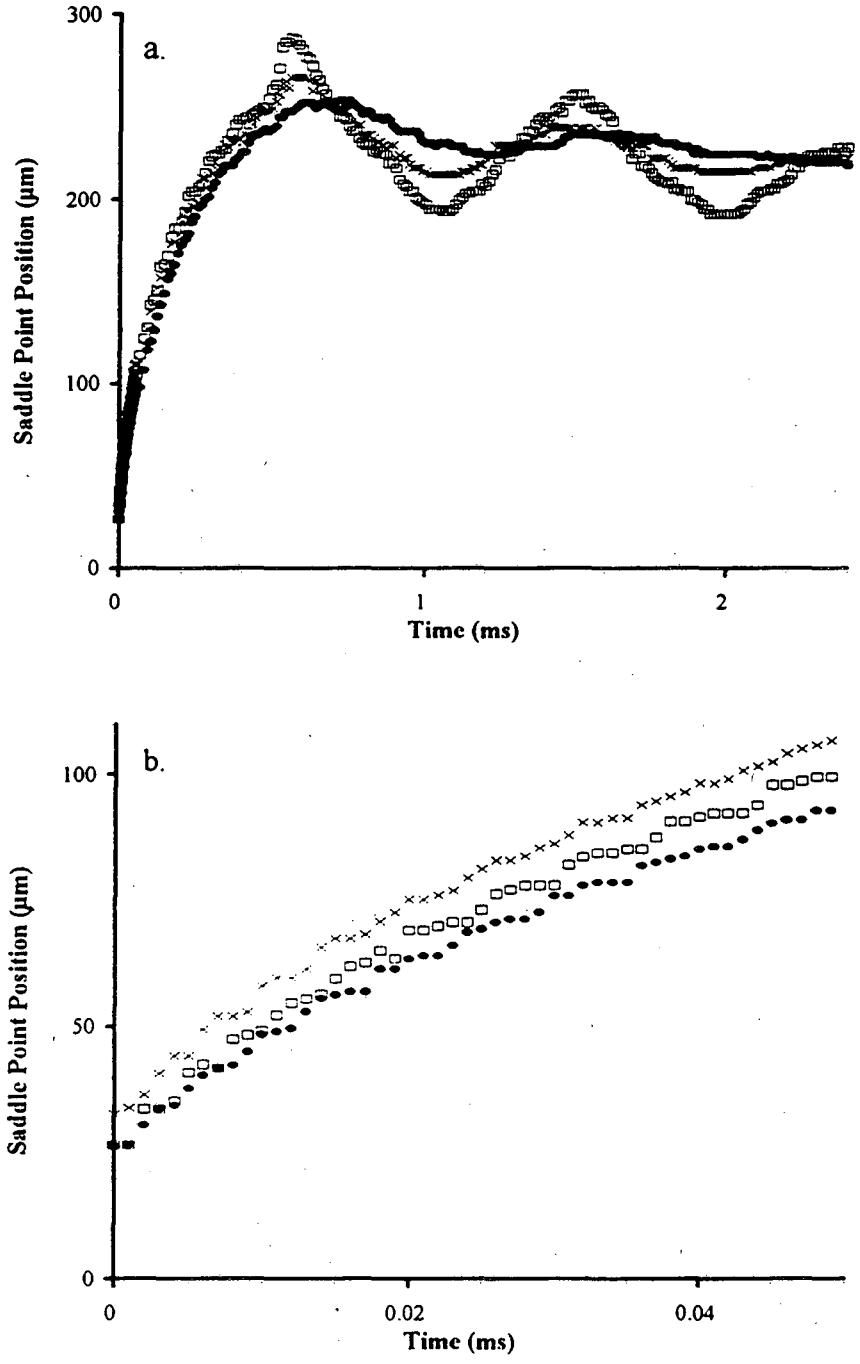

Figure IIA-4. Kinematic viscosity, 375-μm dia. bubbles. (a) Saddle-point motion in 1M H_2SO_4 with 10 wt% dextran (●, ν = 5.0 cSt), with 6 wt% dextran (×, ν = 3.0 cSt), and without dextran (□, ν = 1.1 cSt). (b) Expanded scale for short time.

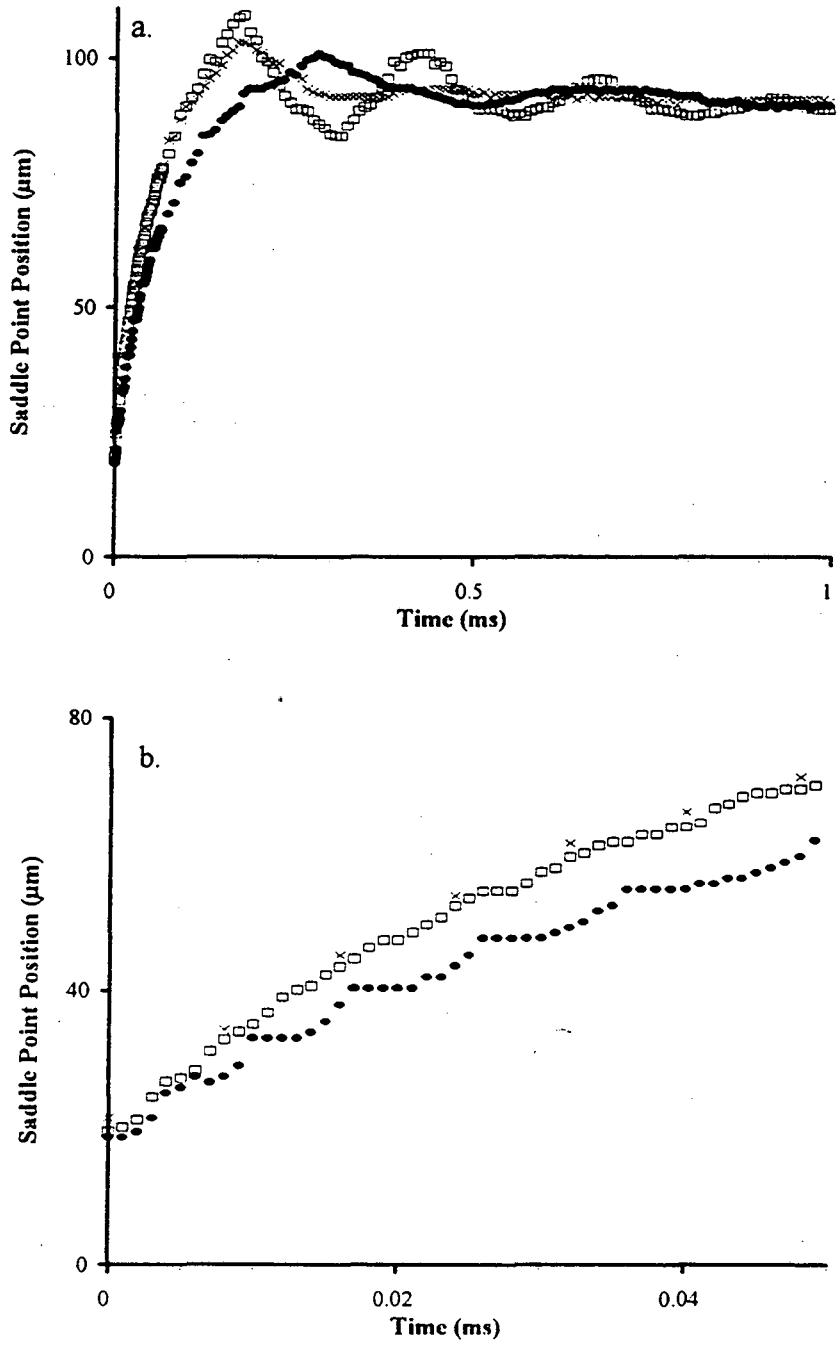

Figure IIA-5. Surface tension, 150-μm dia. bubbles. (a) Saddle-point motion in 1M H_2SO_4 with 0.07M n-hexanol (●, σ = 25 dyne/cm), with 0.001M n-hexanol (×, σ = 49 dyne/cm), and without alcohol (□, σ = 73 dyne/cm). (b) Expanded scale for short time.

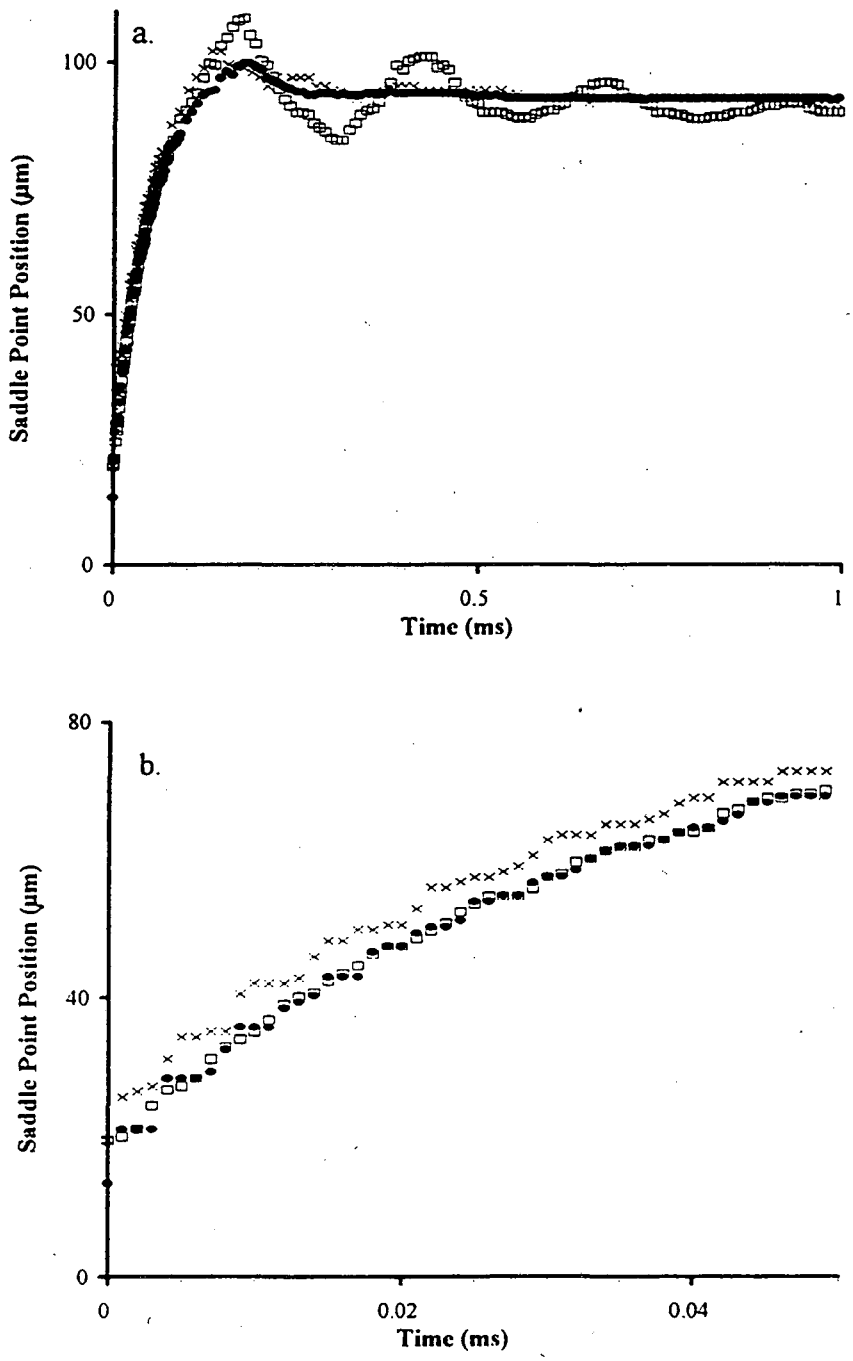

Figure IIA-6. Kinematic viscosity, 150-μm dia. bubbles. (a) Saddle-point motion in 1M H_2SO_4 with 10 wt% dextran (●, ν = 5.0 cSt), with 6 wt% dextran (×, ν = 3.0 cSt), and without dextran (□, ν = 1.1 cSt). (b) Expanded scale for short time.

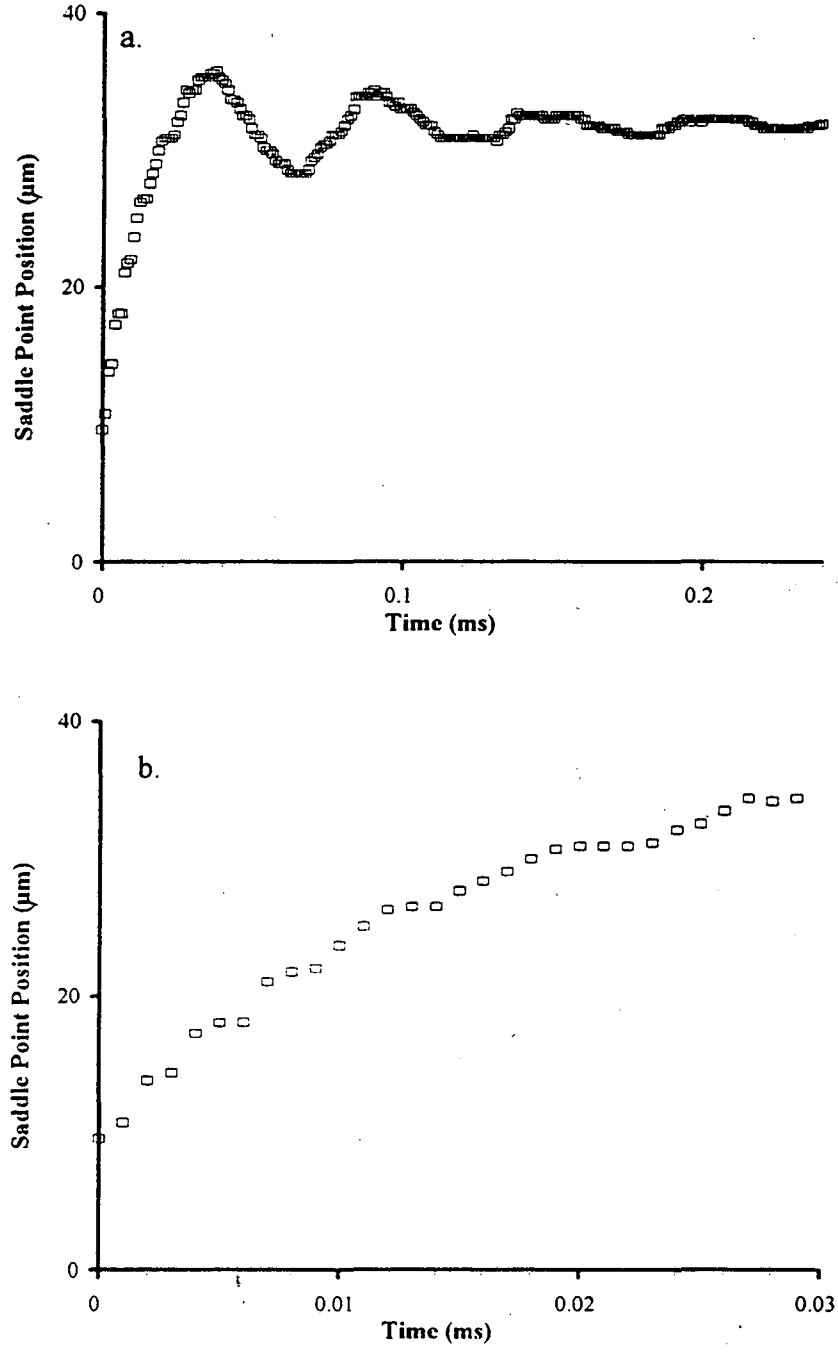

Figure IIA-7. 50-μm dia. bubbles. (a) Saddle-point motion in 1M H_2SO_4. (b) Expanded scale for short time.

APPENDIX IIB: FIDAP Input File

This is the input file for the simulation of bubble coalescence. This file creates the domain, specifies the mesh, and states boundary conditions and solution strategy to be used by FIDAP.

```
FI-GEN
/ Creating POINTS ----------------------------------------------------------------
POINT ( ADD, COORDINATES, SYSTEM = 1, CARTESIAN)
/ [X] [Y] [Z]          [Id comment]
  1.65 0 0
  1.65 1.65 0
  0 1.65 0
  0 0 0
  0 0.00711 0
  0.00175 0.05 0
  0.00452 0.08 0
  0.00859 0.11 0          8
  0.01398 0.14 0
  0.02072 0.17 0
  0.02886 0.2 0
  0.03843 0.23 0
  0.04952 0.26 0
  0.06 0.28509 0
  0.13 0.40863 0
  0.2 0.49281 0           16
  0.27 0.55583 0
  0.34 0.60436 0
  0.41 0.64167 0
  0.48 0.66965 0
  0.55 0.68944 0
  0.62 0.70172 0
  0.69 0.7069 0
  0.76 0.70512 0          24
  0.83 0.69634 0
  0.9 0.68028 0
  0.97 0.65642 0
  1.08125 0.6
  1.18077 0.525 0
  1.25252 0.45 0
  1.30657 0.375 0
  1.3474 0.3 0            32
  1.37744 0.225 0
```

```
 1.3981 0.15 0
 1.41021 0.075 0
 1.4142 0 0
 1.45 0 0
 1.42 0.3163 0
 0.95 0.84 0
 0.22235 0.7 0        40
 0 0.4 0
 1.65 12 0
 0 12 0
 1.65 0.3675 0
/ Creating CURVES ----------------------------------------------------------
POINT ( SELECT, ID )
 4
 36
 37
 1
CURVE (ADD,LINE)
POINT ( SELECT, ID )
 4
 5
 41
 3
CURVE (ADD,LINE)
POINT ( SELECT, ID )
 4
 15
 40
CURVE (ADD,LINE)
POINT ( SELECT, ID )
 4
 32
 38
CURVE (ADD,LINE)
POINT (SELECT,ID)
 5
 6
 7
 8
 9
 10
 11
 12
```

13
14
15
CURVE(ADD)
POINT(SELE,ID)
15
16
17
18
19
20
21
22
23
24
25
26
27
28
29
30
31
32
CURVE(ADD)
POINT(SELE,ID)
32
33
34
35
36
CURVE (ADD)
POINT (SELECT, ID)
37
38
39
CURVE (ADD,ARC)
POINT (SELECT, ID)
39
40
41
CURVE (ADD,ARC)
POINT (SELECT, ID)
2

```
 42
 43
 3
 2
 44
 1
CURVE (ADD, LINE)
CURVE(SELE,ID=14)
POINT(SELE,ID=38)
CURVE(SPLI)
CURVE(SELE,ID=15)
POINT(SELE,ID=40)
CURVE(SPLI)
/ curve 26
POINT(SELE,ID)
 38
 44
CURVE(ADD, LINE)
/ Creating MESH EDGES ----------------------------------------------------------
CURVE(SELE,ID)
 2
 10
 8
 5
MEDGE(ADD,LSTF,INTE=4,RATI=0)
CURVE(SELE,ID)
 3
 26
 6
MEDGE(ADD,LSTF,INTE=6,RATI=2)
CURVE(SELE,ID)
 13
 22
 21
MEDGE(ADD,LSTF,INTE=8,RATI=0)
CURVE(SELE,ID=12)
MEDGE(ADD,LSTF,INTE=16,RATI=0)
CURVE(SELE,ID)
 23
 24
MEDGE(ADD,LSTF,INTE=8,RATI=0)
CURVE(SELE,ID)
 11
```

```
 25
MEDGE(ADD,LSTF,INTE=6,RATI=0)
CURVE(SELE,ID=19)
MEDGE(ADD,LSTF,INTE=14,RATI=2)
CURVE(SELE,ID=20)
MEDGE(ADD,LSTF,INTE=8,RATI=0.5)
CURVE(SELE,ID=16)
MEDGE(ADD,LSTF,INTE=12,RATI=13)
CURVE(SELE,ID=17)
MEDGE(ADD,LSTF,INTE=2,RATI=0)
CURVE(SELE,ID=18)
MEDGE(ADD,LSTF,INTE=12,RATI=0.0769)
/ Creating MESH FACES ------------------------------------------------------
CURVE(SELE,ID)
 2
 22
 10
 13
MFACE(WIRE)
CURVE(SELE,ID)
 10
 23
 24
 8
 12
MFACE(WIRE,EDG2CNT=2)
CURVE(SELE,ID)
 8
 25
 5
 11
MFACE(WIRE)
CURVE(SELE,ID)
 3
 21
 26
 22
MFACE(WIRE)
CURVE(SELE,ID)
 26
 20
 19
 6
```

```
 25
 24
 23
MFACE(WIRE,EDG2CNT=2,EDG4CNT=3)
CURVE(SELE,ID)
 19
 16
 17
 18
MFACE(WIRE)
/ MESHING ------------------------------------------------------------------
MFACE(SELE,ID)
 1
 2
 3
 4
 5
MFACE(MESH,MAP,ENTI="water")
MFACE(SELE,ID=6)
MFACE(MESH,PAVE,ENTI="topwat")
MEDGE(SELE,ID)
 1
 5
MEDGE(MESH,MAP,ENTI="horiz")
MEDGE(SELE,ID)
 4
 7
 20
MEDGE(MESH,MAP,ENTI="vert")
MEDGE(SELE,ID)
 10
 17
 18
 19
MEDGE(MESH,MAP,ENTI="vessel")
MEDGE(SELE,ID)
 8
 11
 14
MEDGE(MESH,MAP,ENTI="surface")
END
```

```
FIPREP
/ This section specifies the equations to be solved, the solution technique,
/     the physical properties, and the boundary conditions.
scale(value=1.12436)
problem(axi-symmetric,free,nonlinear,transient)
PRESSURE(MIXE,discontinuous)
execution(newjob)
option(stress)
solution(q.n.=10)
print(none)
post(nblock=1)
3,100000,3
time(dt=0.5e-5,nsteps=8000,trap,vari=0.004,tsta=0,nofix=5)
/
surfacetension(set="1",const=1.)
viscosity(set="1",const=0.00642)
density(set="1",const=1.0)
/
entity(surface,name="surface",msurf="1",depth=11,ang2=-90.,ang1=180.)
entity(fluid,name="water",mvisc="1",mdens="1")
entity(fluid,name="topwat",mvisc="1",mdens="1")
entity(plot,name="vert")
entity(plot,name="horiz")
entity(plot,name="vessel")
/
bcnode(UX,zero,entity="vert")
bcnode(UY,zero,entity="horiz")
bcnode(velocity,zero,enti="vessel")
/
end
create(fisolv)
end
```

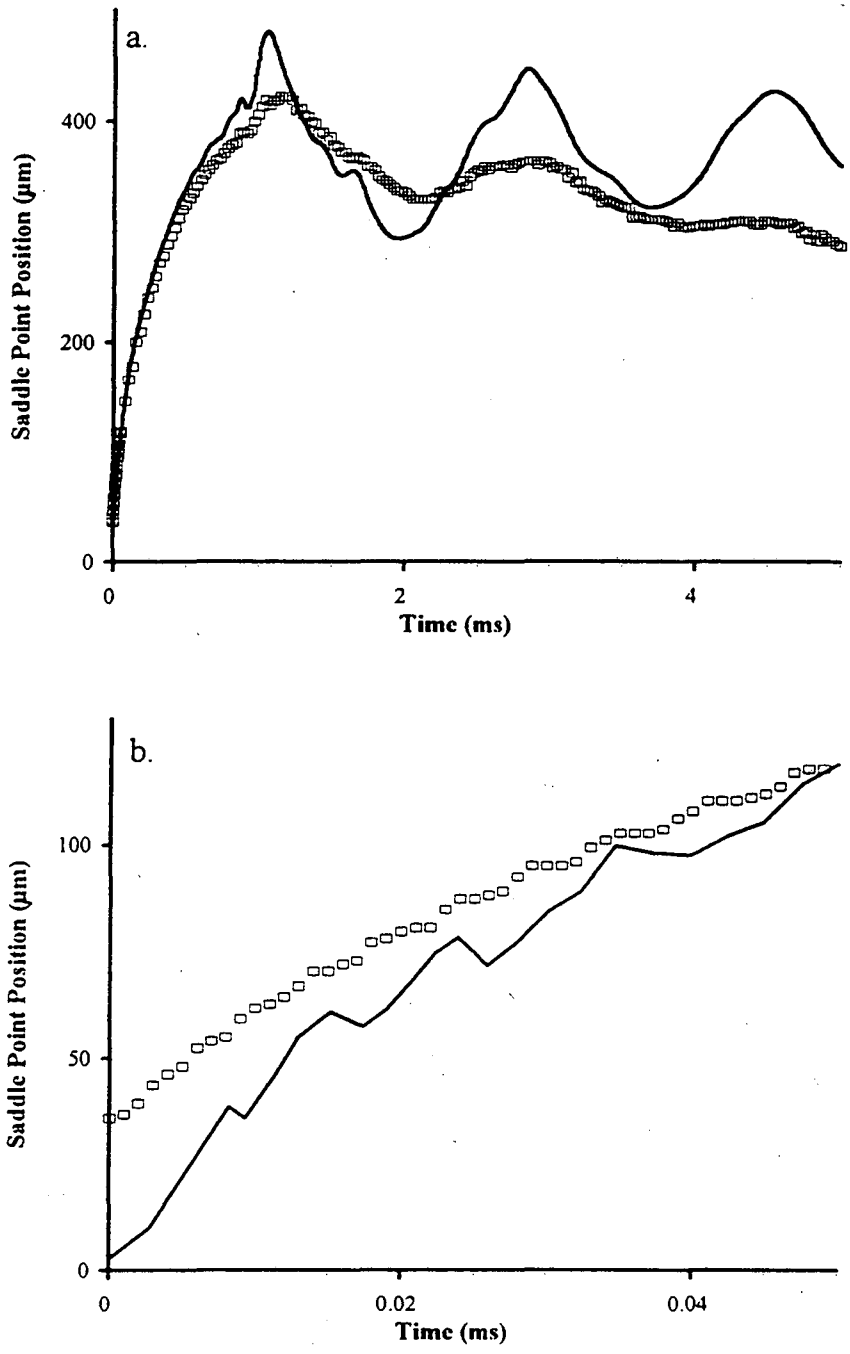

Figure IIc-1. 600-μm dia. bubbles coalescing in 1.1-cSt, 73-dyne/cm liquid. (a) Computed saddle-point motion (—) compared to experimental data (□). (b) Expanded scale for short time.

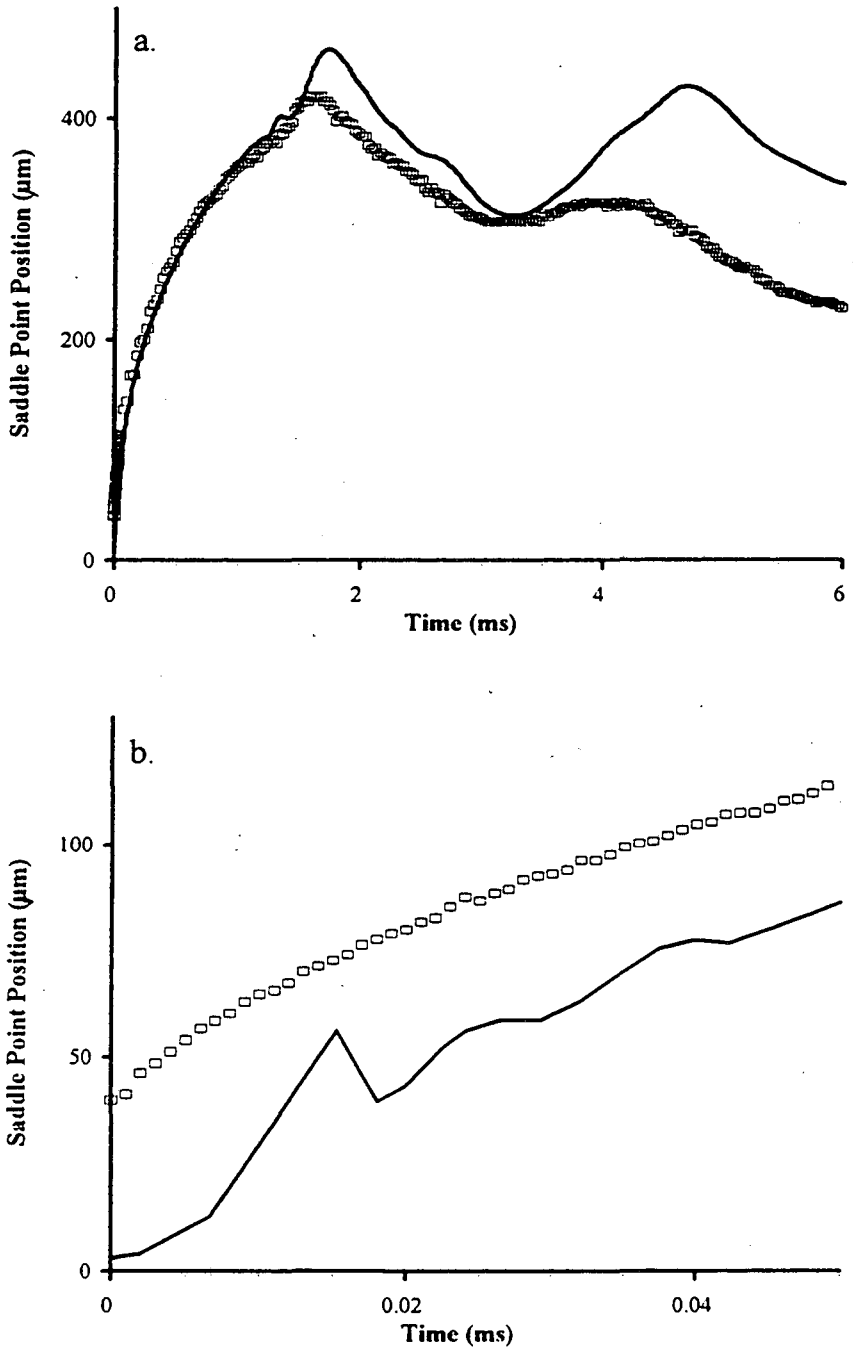

Figure IIc-2. 600-μm dia. bubbles coalescing in 1.1-cSt, 25-dyne/cm liquid. (a) Computed saddle-point motion (—) compared to experimental data (□). (b) Expanded scale for short time.

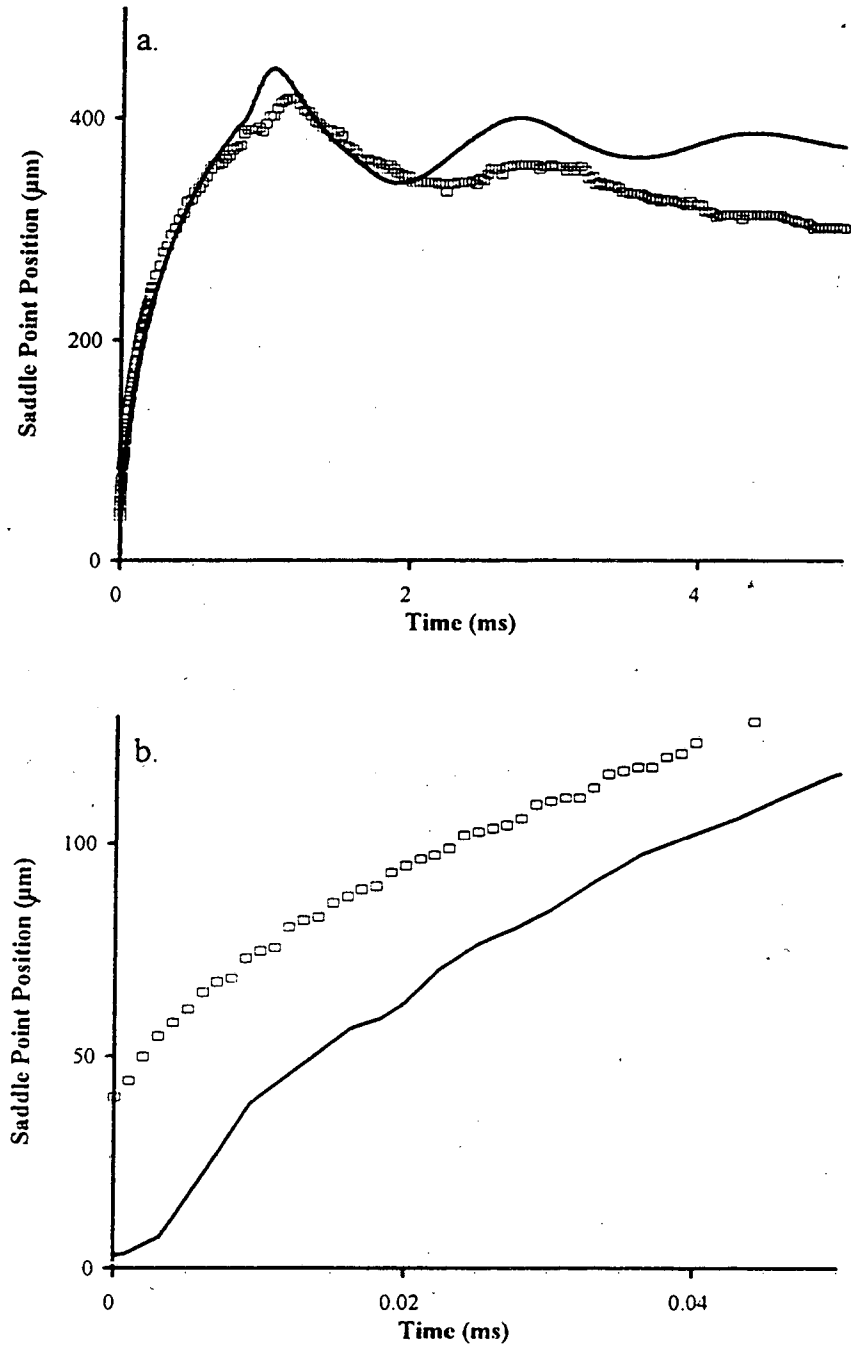

Figure IIc-3. 600-μm dia. bubbles coalescing in 5.0-cSt, 73-dyne/cm liquid. (a) Computed saddle-point motion (—) compared to experimental data (□). (b) Expanded scale for short time.

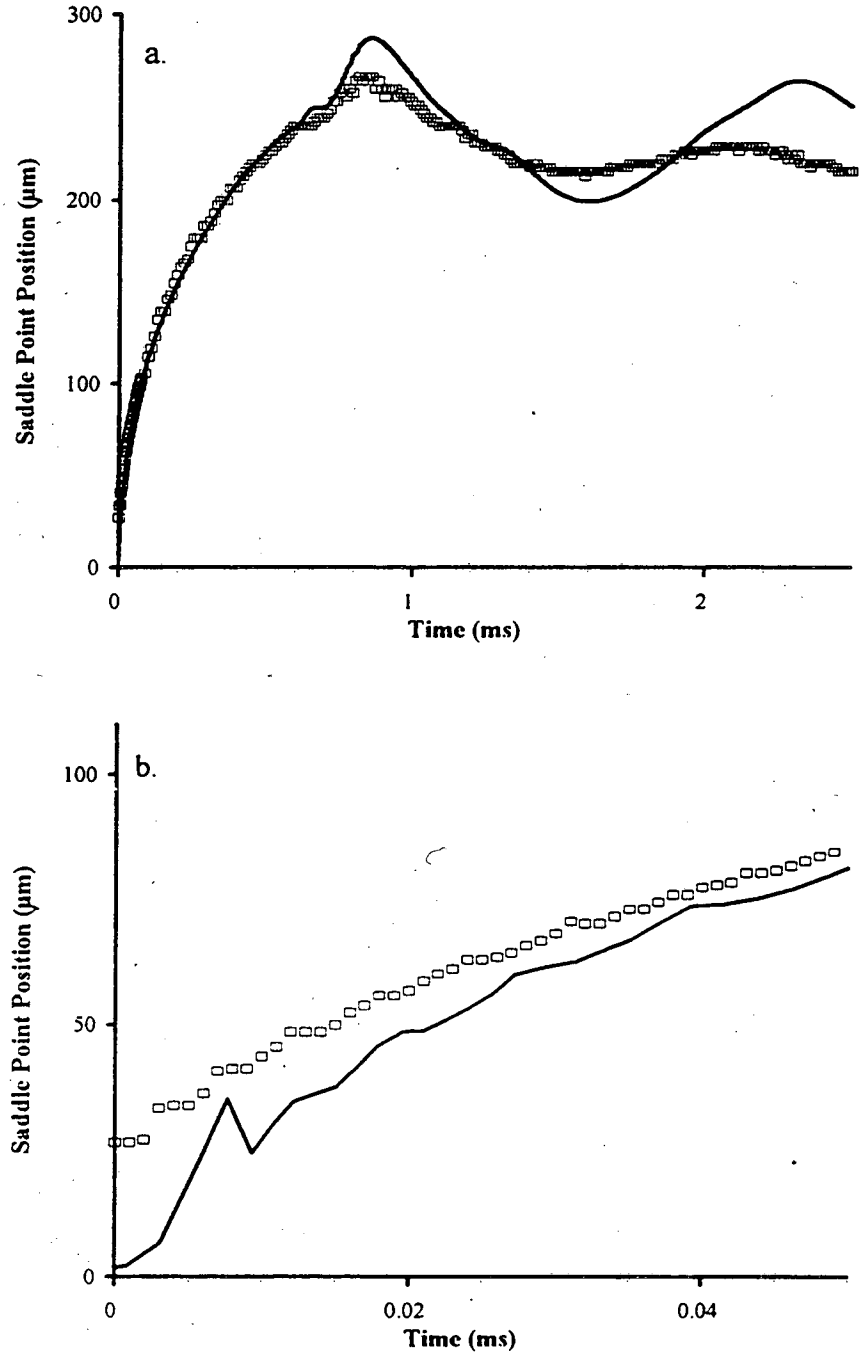

Figure IIc-4. 375-μm dia. bubbles coalescing in 1.1-cSt, 25-dyne/cm liquid. (a) Computed saddle-point motion (—) compared to experimental data (□). (b) Expanded scale for short time.

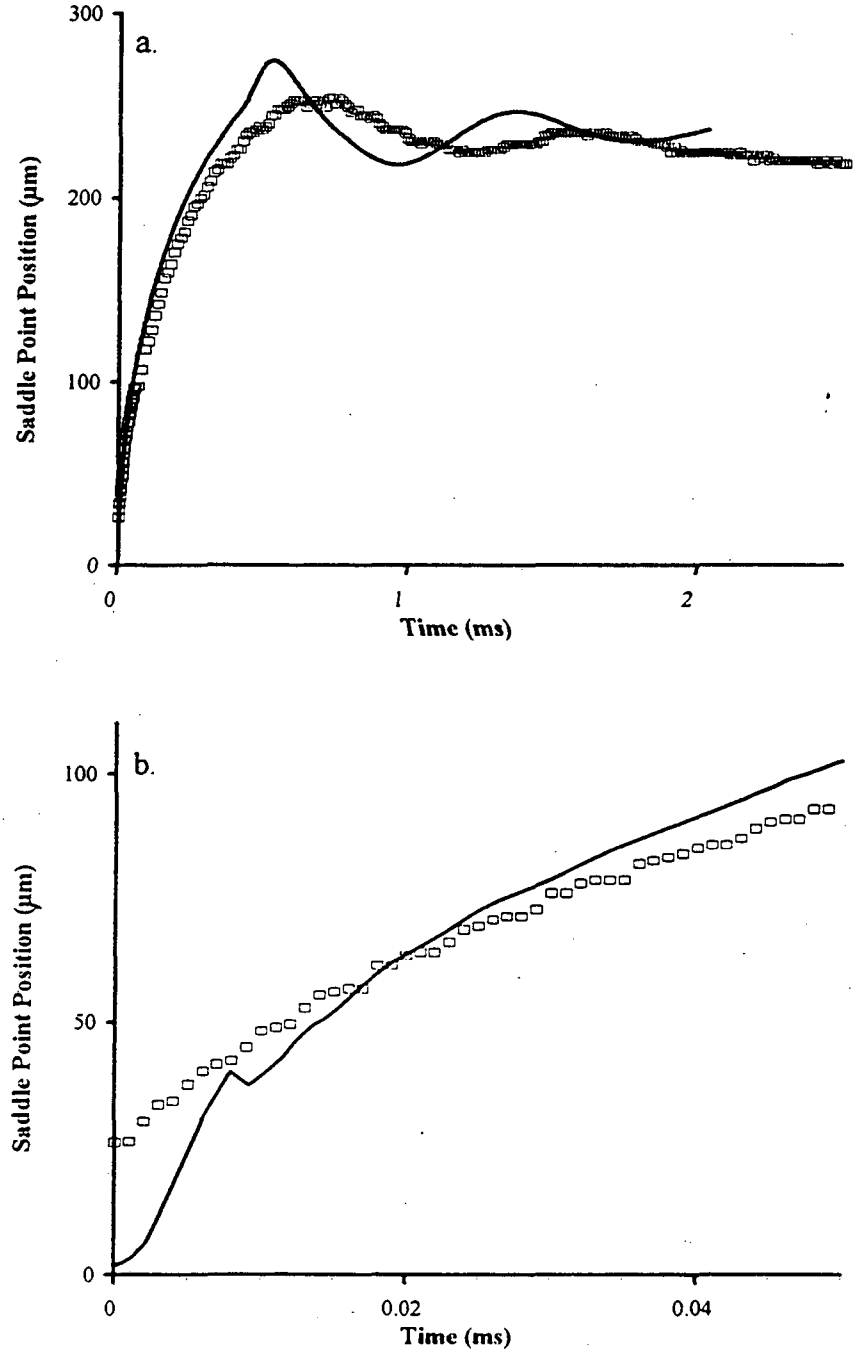

Figure IIc-5. 375-μm dia. bubbles coalescing in 5.0-cSt, 73-dyne/cm liquid. (a) Computed saddle-point motion (—) compared to experimental data (□). (b) Expanded scale for short time.

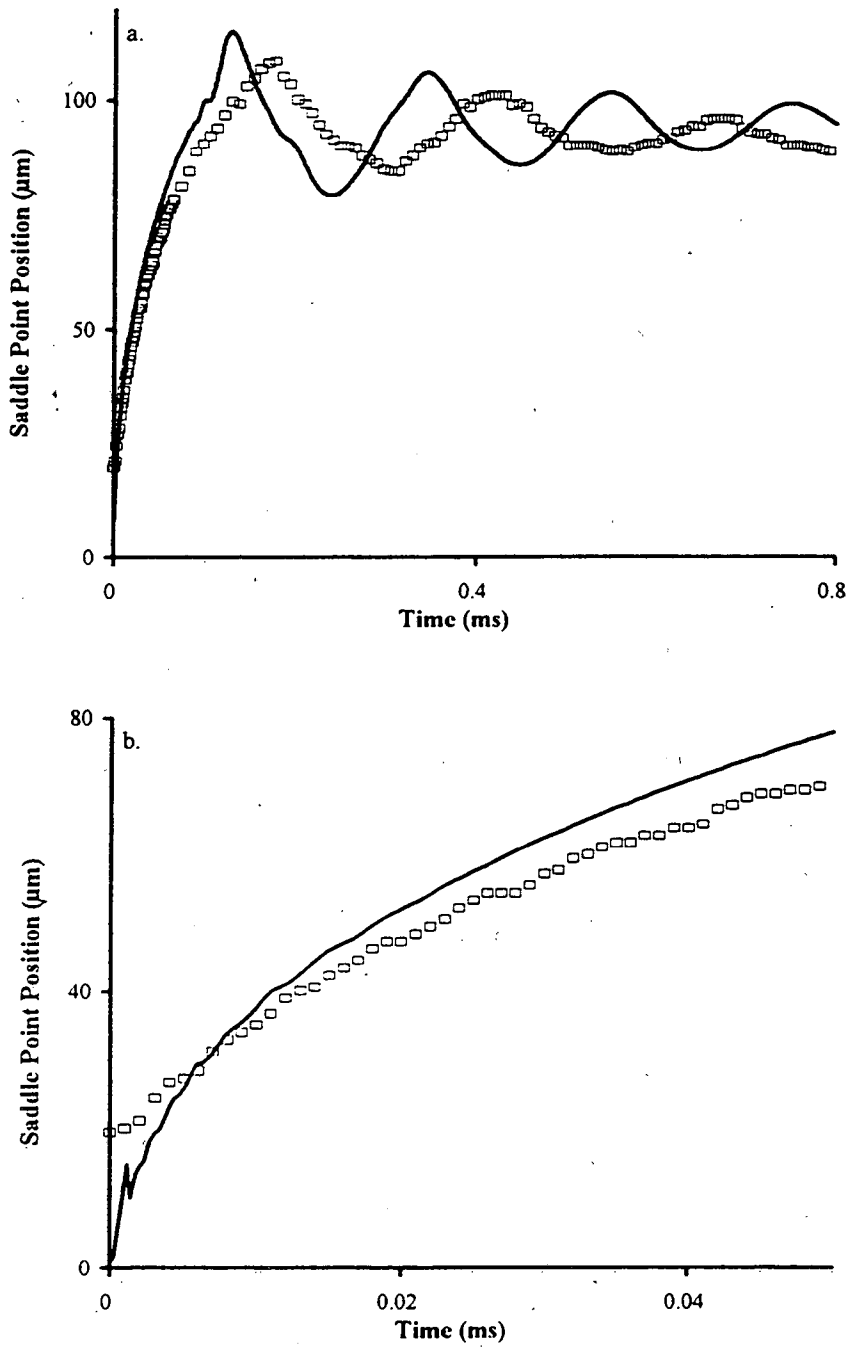

Figure IIc-6. 150-μm dia. bubbles coalescing in 1.1-cSt, 73-dyne/cm liquid. (a) Computed saddle-point motion (—) compared to experimental data (□). (b) Expanded scale for short time.

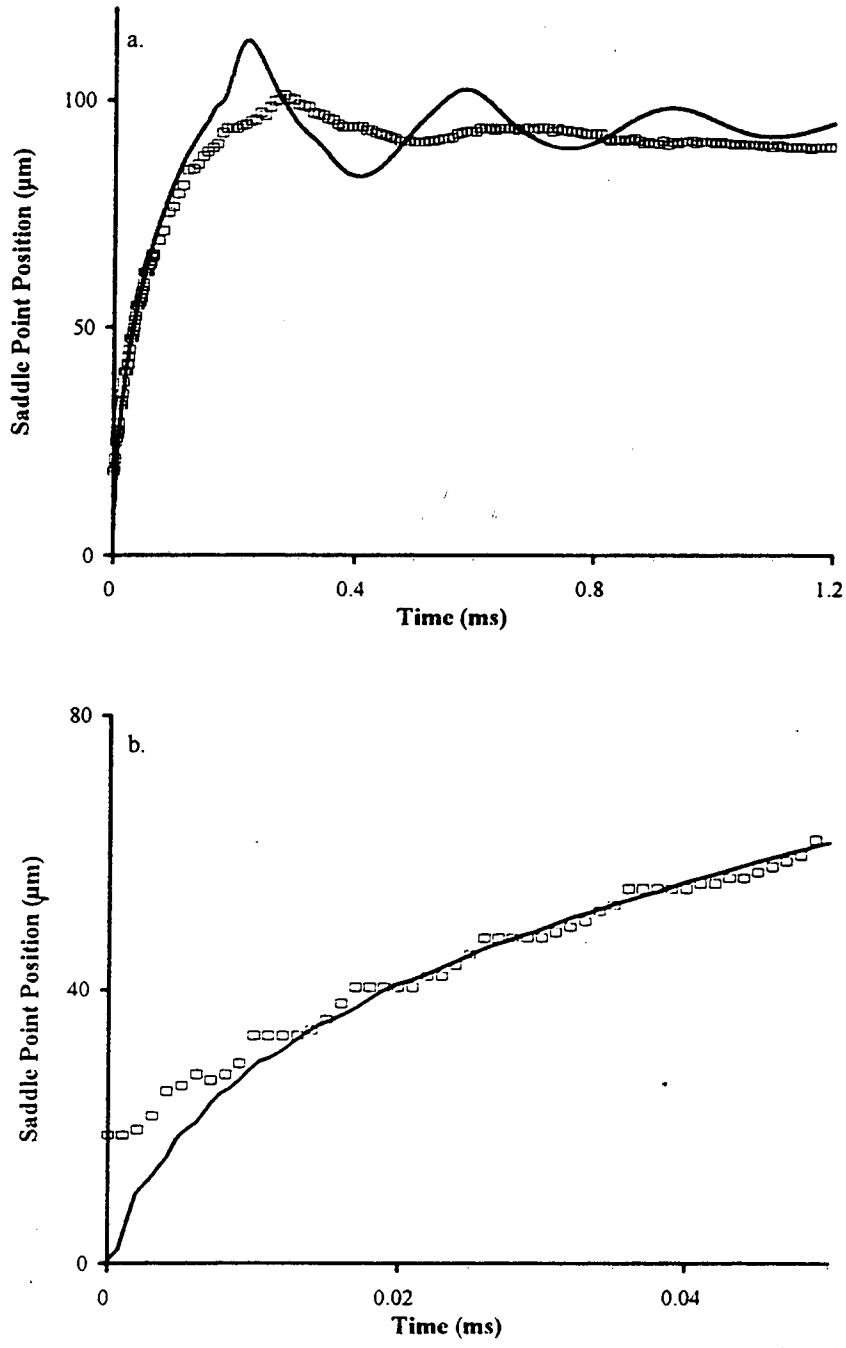

Figure IIc-7. 150-μm dia. bubbles coalescing in 1.1-cSt, 25-dyne/cm liquid. (a) Computed saddle-point motion (—) compared to experimental data (□). (b) Expanded scale for short time.

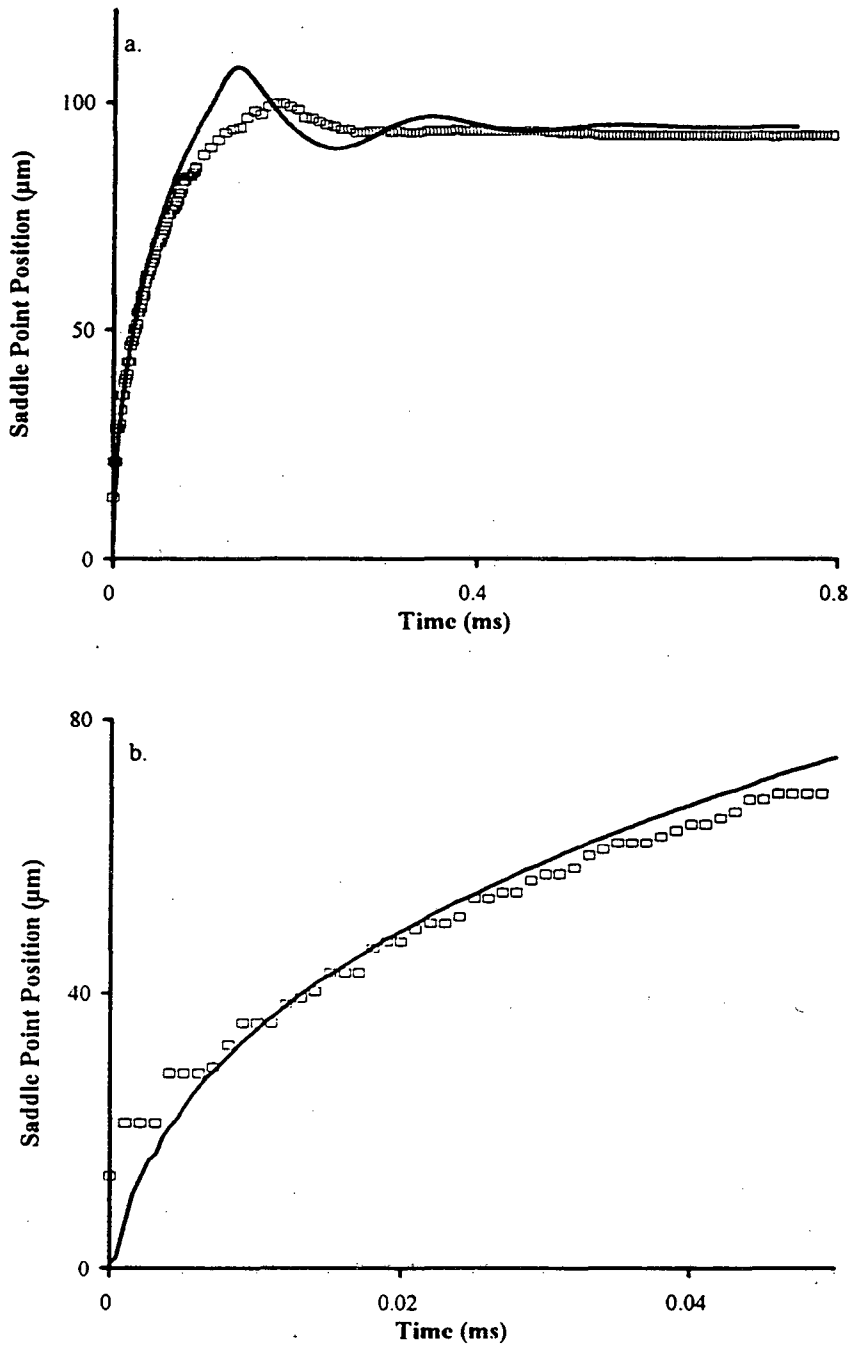

Figure IIc-8. 150-μm dia. bubbles coalescing in 5.0-cSt, 73-dyne/cm liquid. (a) Computed saddle-point motion (—) compared to experimental data (□). (b) Expanded scale for short time.

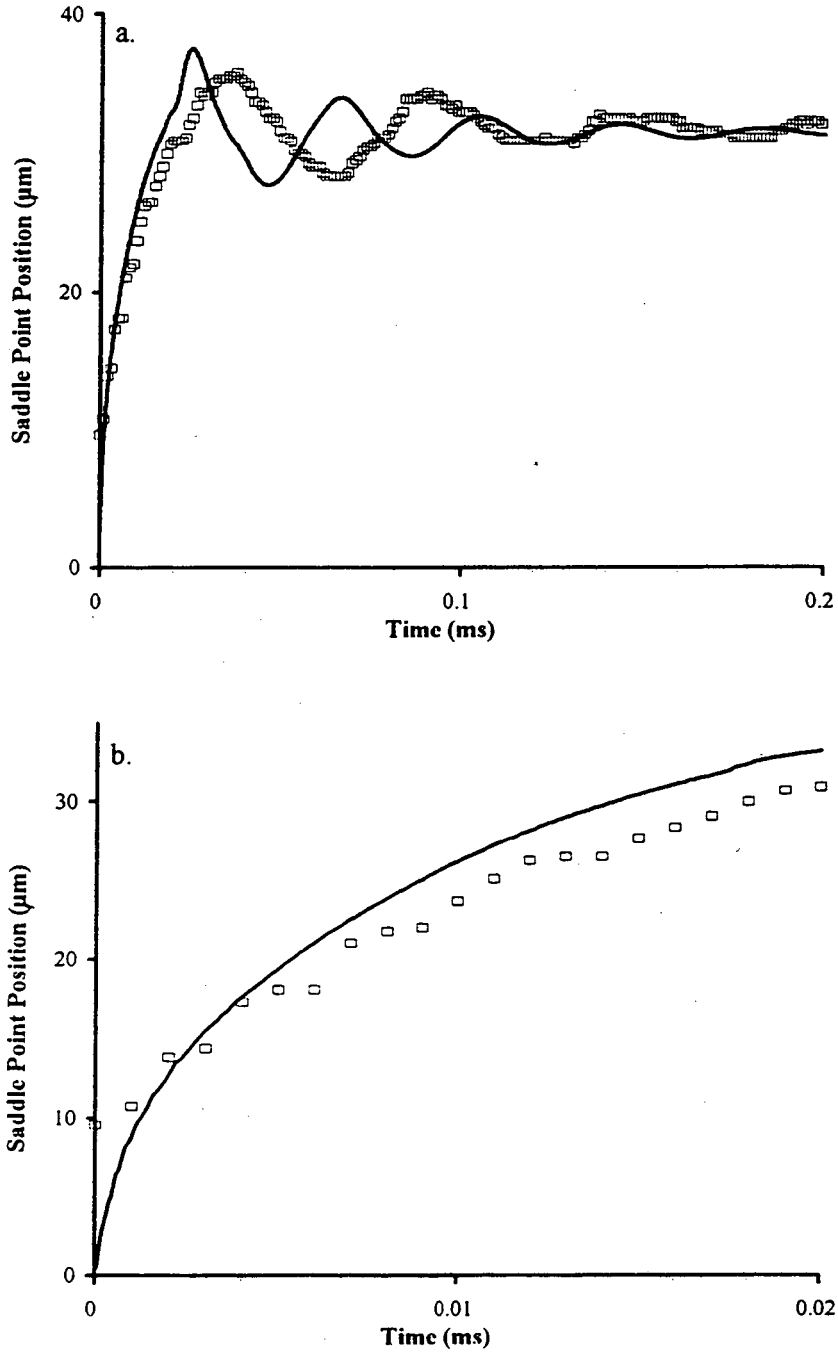

Figure IIc-9. 50-μm dia. bubbles coalescing in 1.1-cSt, 73-dyne/cm liquid. (a) Computed saddle-point motion (—) compared to experimental data (□). (b) Expanded scale for short time.

PART 2: SUPERSATURATION AT GAS EVOLVING ELECTRODES

Chapter 7. INTRODUCTION

A. Overview

The purpose of this investigation is to understand the supersaturation phenomena associated with gas-evolving electrode processes. The accumulation of dissolved gas in the electrolyte adjacent to an electrode creates a concentration overpotential that lowers the energy efficiency of the system. In this research, the dependence of gas supersaturation (concentration in excess of the equilibrium saturation concentration at the system pressure) on current density is determined. We focus on cathodic hydrogen evolution at a recessed, smooth, horizontal, upward-facing, platinum electrode in an unstirred aqueous electrolyte. This system is designed to minimize the variables associated with hydrodynamic and bubble nucleation to provide favorable conditions to attain high degrees of supersaturation. While other investigators have employed only the current-interrupt technique, this study also applies chronopotentiometric polarity-reversal, first used by Breiter[1]. In addition, the range of applied current densities is extended to include low currents. The results of this research and other data are interpreted using the surface renewal model.

Electrolytic gas-bubble evolution is considered to occur in four stages. The first is the establishment of gas supersaturation in the electrolyte adjacent to the electrode. The second, bubble nucleation, occurs at particular locations or sites and is driven by local supersaturation. High-supersaturation concentrations lead to a high density of nucleation sites on the electrode surface. The third stage of gas evolution, bubble growth, occurs

after a bubble has nucleated. Bubbles grow by evaporation of dissolved gas from the surrounding electrolyte and by coalescence with other bubbles. The rate of growth depends on the dissolved gas concentration, the length of the diffusion path, and bubble size and number density. Growth by coalescence occurs when adjacent bubbles touch either by growing into each other or as a consequence of movement of the electrolyte. The fourth stage is bubble detachment which occurs when the forces acting on the bubble, including buoyancy and drag imparted by the motion of the surrounding fluid, overcome the adhesion force between the bubble and the electrode. The buoyancy force is proportional to the size of the bubble. Adhesion forces depend on the nature and properties of the electrode and electrolyte and the presence of surface-active species. The potential of the electrode, including the concentration overpotential, influences adhesion by affecting the gas/liquid/solid contact angle.

The accumulation of dissolved gas, which affects the nucleation frequency and density, diffusion, and bubble adhesion to the electrode, plays a fundamental role in the other three stages of electrolytic gas evolution. The fluid motion and bubble nucleation, conversely, affect supersaturation. The measurement of gas concentration, therefore, requires control of fluid motion and bubble nucleation.

Gas accumulates at an electrode when it is generated faster than it is depleted by convection, diffusion, and/or elimination by bubble formation. Understanding and quantifying gas supersaturation are important to control and improve system performance. However, bubble nucleation, growth, and detachment move the electrolyte in such a complex manner that the fluid mechanics and mass transfer conditions which result are

intractable. In this study, the results obtained on supersaturation at gas-evolving electrodes are compared to those from previous work and analyzed with the goal of quantifying gas supersaturation and its effects on electrolytic processes.

B. Prior Work

The techniques employed to measure gas supersaturation include the indirect method of observing bubble growth and direct methods of determining concentration overpotential or dissolved gas consumption time (transition time) after potential reversal. Bubble-growth observations are best conducted on isolated bubbles at low currents to suppress the effects of fluid motion and bubble nucleation. The necessary assumptions of the method include growth by diffusion only, no interference by adjacent bubbles, and a known dissolved gas concentration profile. Most observations of bubble growth have been analyzed by assuming a uniform concentration[2,3]. However, Bon[4] measured hydrogen concentration overpotentials in the boundary layer at a hydrogen-evolving electrode and found that the hydrogen concentration decayed approximately logarithmically as a function of distance from the electrode surface (figure 7-1).

Concentration overpotential and transition time measurements are electrochemical techniques. The first involves measuring the potential of the electrode surface after the current is interrupted. In the second, the gas species is generated at the electrode and then consumed by application of a reverse current. The time it takes to consume the dissolved gas, the transition time, provides a measure of the interfacial concentration. The equations derived assuming ideal conditions, including stagnant electrolyte and no interference by

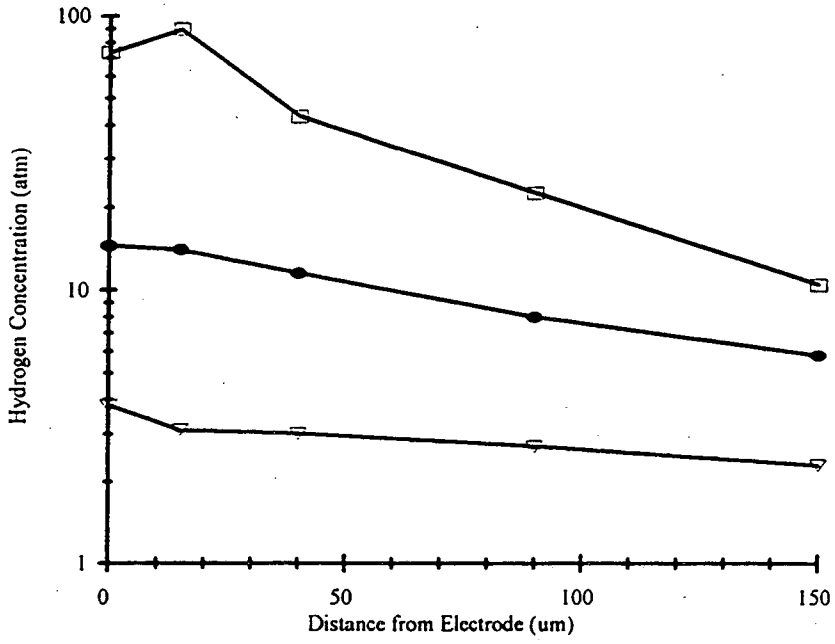

Figure 7-1. Hydrogen concentration profiles adjacent to a gas evolving electrode from Bon[4]. Applied current densities before interrupt were 39.5 (□), 4.0 (●), and 0.4 (▽) mA/cm^2.

other bubbles, are used to calculate the dissolved gas concentrations from the measurements. Both methods rely on the rapid cessation of fluid motion and bubble nucleation, and the rapid decay of the surface overpotential once the gas-generation current is interrupted. The time for bubble nucleation to cease is unknown. Assuming instantaneous cessation of nucleation, fluid motion can be expected to dissipate according to

$$\tau_m = \frac{\rho h^2}{\mu} \qquad (1)$$

where $\tau_m \equiv$ inertial time constant,
$\rho \equiv$ fluid density,
$h \equiv$ characteristic length, and
$\mu \equiv$ fluid viscosity.

The time constant for decay of the surface overpotential, τ_s, can be estimated using[5]

$$\tau_s = R_s C_d a \tag{2}$$

where $R_s \equiv$ electrical resistance of the solution
$C_d \equiv$ capacitance of the double layer, and
$a \equiv$ electrode area.

These time constants provide an estimate of the duration of fluid motion or surface overpotential after the current is interrupted and the cessation of bubble nucleation. Since the fluid motion and surface overpotential decay simultaneously, the larger of the two time constants is used as an estimate of their combined duration.

The concentration overpotential at the working electrode is measured relative to the potential of a reference electrode in the bulk after the current is interrupted. The potential at the time of the interrupt is the concentration overpotential η. Concentrations are then calculated using the Nernst equation which relates the reversible potential, E, of an electrode reaction to the concentrations, C_i, of the reaction constituents assuming unit activity coefficients, as follows[6]:

$$E = E^\circ - \frac{RT}{nF} \ln\left(\prod C_i^{s_i}\right) \tag{3}$$

where $E^\circ \equiv$ standard electrode potential,
$R \equiv$ gas constant (8.314 J/mol-K),
$T \equiv$ temperature (K),
$n \equiv$ stoichiometric number of electrons transferred in the reaction
$F \equiv$ Faraday = 96,485 C, and
$s_i \equiv$ stoichiometric coefficient of species I with the convention that s_i is positive for products and negative for reactants.

In the absence of other overpotentials,

$$\eta = E - E_{reference} \quad (4)$$

In the transition-time measurement technique, also called constant-current chrono-potentiometry, the potential of the electrode surface is measured relative to the potential of a reference electrode in the bulk as the current is switched from cathodic to anodic[7,8]. The anodic current consumes the cathodically generated species present at the electrode interface. Eventually, the concentration of the species decreases to zero and the flux of species to the electrode surface is insufficient to accept all of the electrons being forced across the electrode-solution interface. The potential of the electrode then rapidly increases to more positive values until another oxidation reaction occurs. The time required for this potential transition to occur is called the transition time, τ. Assuming mass transport by diffusion only, the measured transition time is used in conjunction with the Sand equation

$$\frac{J_a \tau^{\frac{1}{2}}}{C_i} = \frac{nFaD_i^{\frac{1}{2}} \pi^{\frac{1}{2}}}{2} \quad (5)$$

to determine the concentration of the species of interest at the electrode surface, C_i. Here, J_a is the anodic reversal current, a is the electrode area, and D_i is the diffusion coefficient of species I. The anodic current must be of sufficient magnitude to oxidize the cathodic product species before a measurable amount has diffused into the bulk or departed as bubbles. According to equation (5), the quantity $J_a\tau^{1/2}$ should be constant, independent of J_a, for a given cathodic current.

In this study, the concentration overpotential measured after current interrupt and the transition time determined after current reversal provide two independent means to quantify supersaturation concentrations at a gas-evolving electrode.

References

1. Breiter, M. and Becker, M., *Z. Electrochem.*, **60**, 1081 (1956).
2. Westerheide, D.E. and Westwater, J.W., *A.I.Ch.E Journal*, 7, 357 (1961).
3. Glas, J.P. and Westwater, J.W., *Int. J. Heat Mass Transfer*, 7, 1427 (1964).
4. Bon, C.K., M.S. Thesis, University of California at Berkeley, 1970.
5. Bard, A.J. and Faulkner, L.R., Electrochemical Methods, Wiley, p. 570, 1980.
6. *ibid*, p. 51.
7. Breiter, M., Transactions of the Symposium on Electrode Processes, E. Yeager, ed., John Wiley (1961).
8. Bard, A.J. and Faulkner, L.R., *op.sit.*, p.249.

Chapter 8. EXPERIMENTAL

Apparatus - Hydrogen supersaturations were measured using a two-compartment acrylic resin cell with an intervening porous glass frit shown in figure 8-1. To separate the reaction products, the anode was located in one compartment and the cathode and a bubbling, reversible, hydrogen reference electrode was placed in the other compartment (figure 8-1). 1M H_2SO_4 was used as the electrolyte in all experiments. It was prepared with analytical grade 99.95% H_2SO_4 and de-ionized distilled water. The cell contained about 500 ml of electrolyte. The electrolyte was pre-electrolyzed and sparged with pure hydrogen in a separate glass container overnight before being introduced into the cell. Hydrogen sparging continued in both compartments during the experiments. Anodic and cathodic cycling at 60 mA/cm^2 was applied for approximately 5 minutes before recording each datum.

The working electrode was a 1.43-cm diameter platinum disk. The surface of the electrode was polished using a Buehler metallurgical polishing wheel, nylon polishing

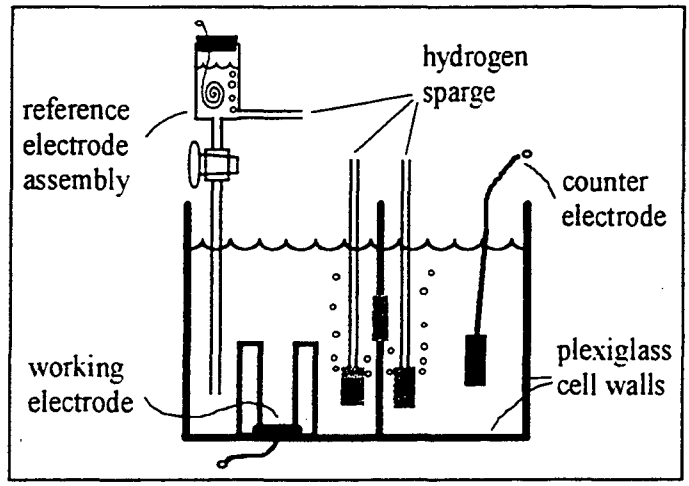

Figure 8-1. Supersaturation cell schematic.

cloth, and 5-, 1- and 0.25-micron diamond paste. Polishing continued until a mirror finish was obtained and no scratches were observable under 10x magnification. Thorough rinsing with hexane, de-ionized distilled water, and the electrolyte preceded placement of the electrode in the cell. The electrical connection was made to the electrode through the bottom of the cell. A 1-cm deep acrylic resin annulus fitted on the inside with an insulating 1.15 cm inner diameter glass shim was placed on the electrode surface, which was facing upwards. Bolts threaded through the bottom of the cell into the annulus sealed the annulus to the electrode and the bottom of the cell. This arrangement assured a uniform current distribution by restrictive contact between the insulating annulus and the surface of the electrode. Because the electrode was recessed, flow of electrolyte from the bulk was restricted.

The counter electrode was a 2-cm by 1-cm platinum sheet spot welded to a heavy, 1-mm diameter platinum wire. The reference electrode was constructed using 1 meter of 0.5-mm diameter platinized-platinum wire coiled and suspended in 20 ml of the electrolyte in a 40-ml glass vessel. Pure hydrogen, bubbled into the bottom of the vessel, escaped through a small hole in the top to ensure that the electrolyte remained saturated and deaerated. Electrical contact between the reference electrode assembly and the cell was maintained through a wetted glass stopcock in a glass tube extending from the bottom of the reference electrode vessel into the working electrode compartment (see figure 8-1).

The experiments were conducted galvanostatically using an EG&G PAR 173/176 potentiostat/galvanostat. Data were recorded with a Nicolet 4094 digital oscilloscope and transferred to a desktop computer for analysis.

Concentration overpotential measurements - Current densities in the range 0.4 to 72 mA/cm^2 were applied. Overpotentials were measured to the nearest 1 mV, the detection limit of the apparatus. Cathodic currents were applied to the working electrode until steady-state potentials were observed, approximately 15 seconds at 40 mA/cm^2 and 4 minutes at 0.1 mA/cm^2. Current interrupt and data collection with an oscilloscope were initiated simultaneously by manual switching. The sampling rate was 1000 pts/s and the oscilloscope memory has a 1200 point capacity. Using equation (1) in Chapter 7 with a characteristic length of 50 μm (the median diameter of a hydrogen bubble liberated in 1M H_2SO_4)[1] and the properties of 1M H_2SO_4, the time constant for cessation of fluid motion is 2.5 ms. Assuming a double layer capacity of 230 $\mu F/cm^2$ (appropriate for a 2M ionic strength electrolyte), a cell resistance of 14 Ω (measured in the apparatus), and an electrode area of 1 cm^2, equation (2) in Chapter 7 gives a time constant of 3.2 ms for decay of the surface overpotential. Overpotential data were extrapolated to three time constants, or 9.6 ms, after interrupt.

The Nernst equation was applied to the hydrogen evolution reaction :

$$2H^{\bullet} + 2e^{-} \rightleftharpoons H_2 \qquad (1)$$

yielding the following expression for the hydrogen concentration overpotential, $\eta_{H2}^{\bullet}$, at the working electrode :

$$\eta_{H_2}^{\bullet} = -\frac{RT}{2F}\ln\left(\frac{C_{H_2}}{C_{H^{\bullet}}^2}\right) \qquad (2)$$

where C_{H2} ≡ supersaturation concentration of hydrogen in solution and

C_{H+} ≡ concentration of protons.

C_{H+} can be considered equal to the bulk proton concentration of 2M.[a] Because the reference electrode used in the present work is a reversible hydrogen electrode, equations (3) and (4) in Chapter 7 apply. The measured overpotential is

$$\eta = -\frac{RT}{2F}\ln\left(\frac{C_{H_2}}{C_{H^+}^2}\right) - \left[-\frac{RT}{2F}\ln\left(\frac{C_{H_2}}{C_{H^+}^2}\right)\right]_{ref} \quad (3)$$

Since the electrolyte in the cell and in the reference electrode assembly are the same, the proton concentration is uniform. Rearranging equation (3) leads to

$$\eta = -\frac{RT}{2F}\ln\left(\frac{(C_{H_2})}{(C_{H_2})_{ref}}\right) \quad (4)$$

With a linear relationship between the hydrogen concentration in solution and the pressure of hydrogen in equilibrium with the solution, an expression for the concentration overpotential in terms of the supersaturation pressure, P_{H2}, is obtained:

$$\eta = -\frac{RT}{2F}\ln(P_{H_2}) \quad (5)$$

Transition time measurements - Oxidizing currents were applied after a steady potential was recorded during cathodic hydrogen evolution, as described in the section above. It was found by trial and error that an oxidizing current density of 55 mA/cm^2 was

---

[a] Over a 50-micron Nernst boundary layer, at a current density as high as 10 A/cm^2, the concentration of protons at the interface would only be reduced by 0.2 % in 1M H_2SO_4 because of the high mobility of H^+.

sufficient to produce constant values of $j_a\tau^{1/2}$ for hydrogen evolution current densities of 4 mA/cm^2 or smaller. A 120 mA/cm^2 oxidizing current density was applied after cathodic currents above 4 mA/cm^2. Current reversal was accomplished by switching a constant external signal to the galvanostat such that the cathodic current plus the external signal resulted in the desired anodic current density. Supersaturation concentrations were calculated using equation (5) of Chapter 7, a hydrogen diffusivity of $3.8x10^{-5}$ cm^2/s [2], and an atmospheric saturation concentration of $7.2x10^{-7}$ mol/cm^3 [3].

References

1. Janssen, L.J.J., and Hoogland, J.G., *Electrochimica Acta*, **15**, 1013 (1970).
2. Aikazyan, E.A. and Federova, A.I., Dolk. Akad. Nauk. SSR, **86**, 1137 (1952).
3. Pray, Schweickert, and Minnich, *Ind. Eng. Chem.*, **44**, 1146 (1952).

Chapter 9. RESULTS

Discussion of results - Results of measurements of the concentration overpotential and transition time are shown in figures 9-1 and 9-2, respectively, and summarized in table 1. The estimated experimental error in the concentration overpotential technique was ± 3 mV or about ±8%. The error in the transition time technique was ± 0.001 $As^{1/2}$ or about ±5%. These errors represent the standard deviation of 5 repeated measurements carried out under identical conditions. These values indicate that the experiments are quite reproducible.

The data in table 1 were used to calculate the supersaturation ratio shown in figure 9-3. The values shown in the figure are the hydrogen activities measured relative to the hydrogen activity at the reference electrode at steady state as a function of the cathodic current. The results in figure 3 show good agreement between the saturation obtained from the concentration overpotential and transition time techniques.

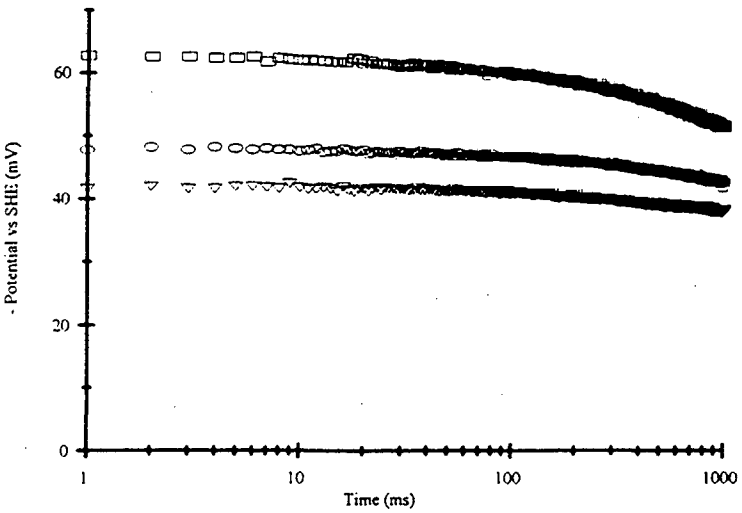

Figure 9-1. Concentration overpotential data. Applied current density before interrupt was 40 (□), 4.0 (○), and 0.4 (▽) mA/cm^2.

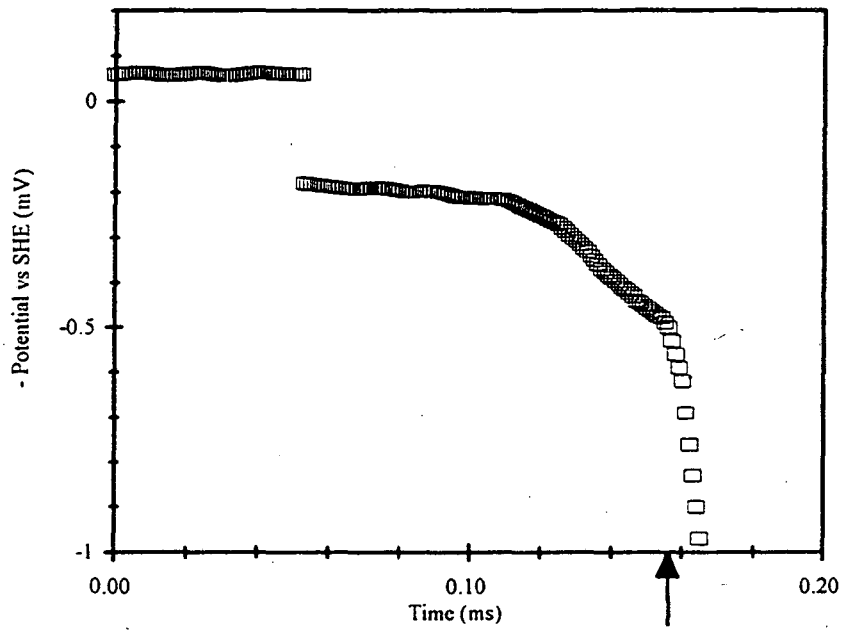

Figure 9-2. Transition time data. An cathodic current of 0.4 mA/cm^2 was switched to an anodic current of 55 mA/cm^2 at t=0.05 ms. The arrow indicates a transition time of 118 ms.

Table 1. Hydrogen supersaturation data.

current density (mA/cm^2)	concentration overpotential (mV vs SHE)	transition time τ (ms)	$J_a\tau^{1/2}$ (A s$^{1/2}$)
0.4	42.0	118	0.0189
1.7	45.4		
4.0	48.5	223	0.0260
9.5	53.6		
17.3	56.5		
27.5	60.1		
40.0	61.5	439	0.0795
54.8	64.0		
72.0	66.5		

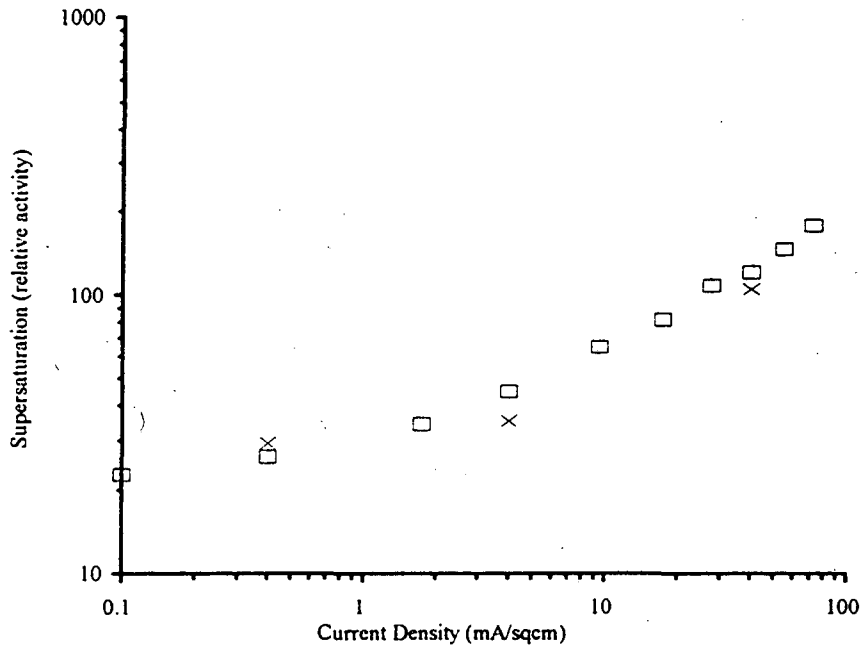

Figure 9-3. Hydrogen supersaturation experimental data.
Supersaturation measured by concentration overpotential method (□) and transition time method (×).

Comparison to other experiments - For comparison, figure 9-4 shows the results of Egan[1], Bon[2] , and Shibata[3]. The supersaturation results determined in this work agree with those of Bon using similar surface texture (smooth), orientation (horizontal), and system geometry (recessed electrode). The results obtained by Egan with a coarse electrode were lower than those of this work, indicating the effect of surface texture on supersaturation. Since bubbles nucleate preferentially at scratches and pits on the electrode surface[4], a coarse electrode such as that of Egan shortens the average gas diffusion path length by providing a high density of nucleation sites. Also, because the actual surface area of a coarse electrode is greater than that of a smooth electrode of the same superficial area, the actual current density and corresponding supersaturation are lower. Supersaturations measured in this work were also higher than those of Shibata measured at a smooth

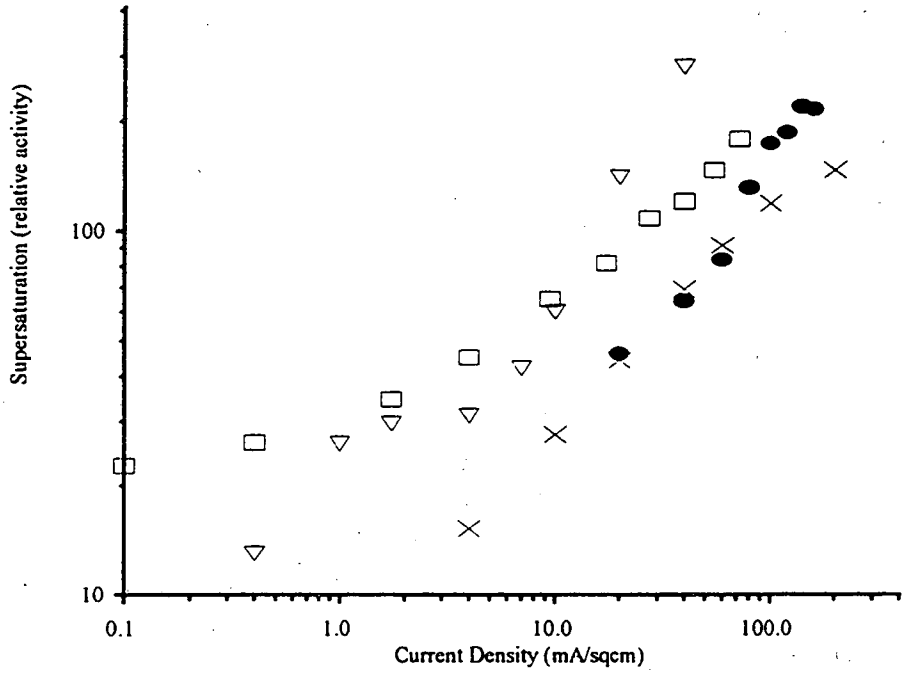

Figure 9-4. Hydrogen supersaturation results. This work (□) compared to the results of Egan (●) at a coarse horizontal recessed electrode, of Bon (▽) at a smooth horizontal recessed electrode, and of Shibata (×) at a smooth vertical non-recessed electrode.

vertical non-recessed platinum wire. At the vertical electrode used by Shibata, movement of bubbles along the surface mixed the electrolyte and replenishing flow was obstructed only by the electrode surface itself.

References

1. Egan, E. and Tobias, C.W., personal communication (1993).

2. Bon, C.K., M.S. Thesis, University of California at Berkeley, 1970.

3. Shibata, S., *Bull. Chem. Soc. Jpn.*, **36**, 53 (1963).

4. Westerheide, D.E. and Westwater, J.W., *A.I.Ch.E Journal*, 7, 357 (1961).

Chapter 10. THEORETICAL ANALYSIS

Asymptotic limits - Homogeneous nucleation theory, which represents the limiting case of an ideally smooth electrode (no nucleation sites), predicts a hydrogen supersaturation of 1500 atm in 1N H_2SO_4[1,2]. However, homogeneous nucleation is not observed in the present study because supersaturation did not reach this level. Even with a highly polished surface, sites for bubble nucleation are present which reduces gas supersaturation.

Under the hypothetical condition of no bubble formation, maximum supersaturation is achieved, because hydrogen removal from the surface is limited by low diffusion rates in aqueous systems [D = O(10^{-5} cm^2/s)]. Assuming the bulk electrolyte is well mixed, a linear concentration profile of thickness δ forms, and the steady-state surface concentration of hydrogen is

$$C_{H_2,o} = C_{H_2,\infty} + \frac{i\delta}{nFD} \qquad (1)$$

where $C_{H2,o}$ ≡ surface concentration,
$C_{H2,\infty}$ ≡ bulk concentration, and
D ≡ hydrogen diffusion coefficient.

At low currents where gas bubbles are not formed and the electrolyte is stagnant, the surface concentration is a function of time according to equation (5) of Chapter 8. Supersaturation concentrations at the electrode in the absence of bubble formation were estimated using equation (1) with a diffusion layer thickness of 50 μm at high currents and equation (5) of Chapter 8 with a current-on time of 10 minutes at low currents. The

results are shown in figure 10-1. At current densities above 1 mA/cm^2, the estimated supersaturation in the absence of gas bubbles is higher than observed in practice. This result is reasonable because mass transport adjacent to the electrode surface is not restricted to diffusion only, rather, it is also aided by bubble formation. At current densities below 1 mA/cm^2, however, the experimentally determined supersaturation is higher than the limit predicted without bubble formation. Since bubble formation was observed at all currents, this result is puzzling.

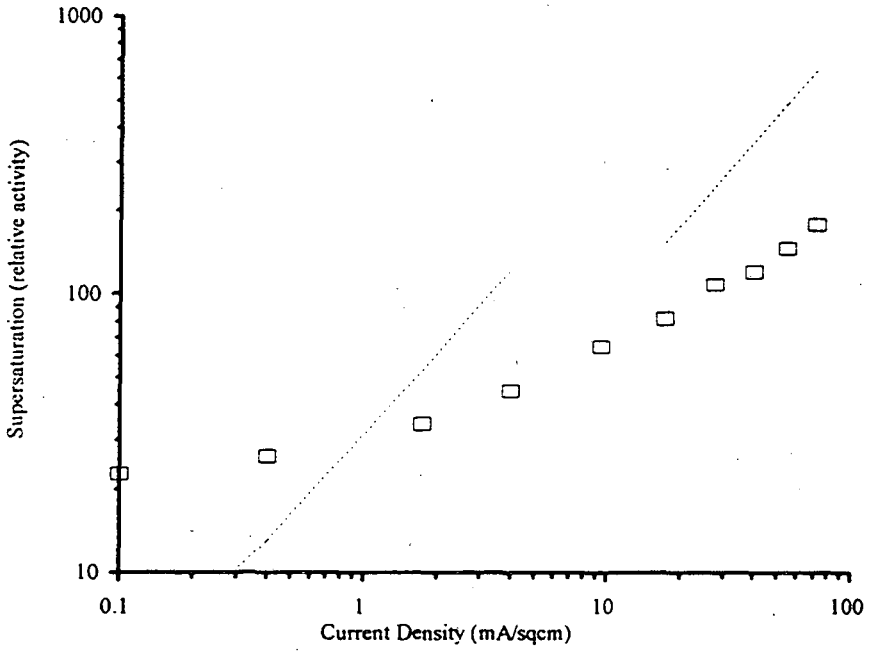

Figure 10-1. Hydrogen supersaturation experimental data and asymptotic limits. Supersaturation measured by concentration overpotential method (□) compared with estimated supersaturation if bubbles did not form (dashed line).

A possible explanation for the unexpectedly high supersaturations measured at low current densities is that contaminants that accumulate on the surface reduce the surface area (increased current density) or eliminate bubble nucleation sites. Although the

electrolyte was purified, gas sparging was continued throughout the experiments, and aggressive anodic/cathodic cycling was applied between runs, still, contaminants could affect the experimental measurements. If contaminants are gradually accumulating during the experiments, their effects would be most significant at low current densities where longer times (up to 10 minutes) are required to achieve steady-state potentials before the current is interrupted.

Surface renewal analysis - A surface renewal model, initially proposed by Ibl[3], will be developed and used to correlate the supersaturation results with current density and other system properties. When dissolved gas leaves the electrode by transient diffusion to form bubbles on the surface (with no diffusion or convection to the bulk), the space occupied by a bubble that detaches from the surface is filled with fresh electrolyte from the bulk. Following bubble detachment, diffusion occurs into the fresh electrolyte until a new bubble forms which instantaneously departs from the electrode surface. If the applied current density, the average bubble size, and the gas diffusion coefficient are known, then the gas supersaturation in the electrolyte that is obtained can be estimated.

The derivation by Ibl derivation begins with the Cottrell solution to the problem of one-dimensional transient diffusion from a constant concentration boundary[4]. Alternately, we began with the solution of the problem of one-dimensional transient diffusion from a constant flux boundary. This equation, analogous to the solution for transient heat conduction into a semi-infinite solid with a constant flux at one wall, is[5]

$$C(t,x) - C_\infty = \frac{2i}{nF}\left(\frac{t}{D}\right)^{\frac{1}{2}} ierfc\left[\frac{x}{(4Dt)^{\frac{1}{2}}}\right] \qquad (2)$$

where $x \equiv$ distance from the electrode surface and
$C_\infty \equiv$ gas concentration in the bulk.

At the surface,

$$C_o = C_\infty + \left(\frac{2i}{nF}\right)\left(\frac{t}{D}\right)^{\frac{1}{2}} \frac{1}{2\Gamma\left(\frac{3}{2}\right)} \qquad (3)$$

Here, $C_o = C(t,0)$. Assuming C_o is constant and equal to the supersaturation concentration at the surface, equation (3) is integrated over the average time for a bubble to form, t_b,:

$$C_o = C_\infty + \frac{2i}{3\Gamma\left(\frac{3}{2}\right)nF}\left(\frac{t_b}{D}\right)^{\frac{1}{2}} \qquad (4)$$

The volume flux of gas into the bubbles, $\dot{\upsilon}$, is estimated with the following equation:

$$\dot{\upsilon} = \frac{\frac{4}{3}\pi\left(\frac{d}{2}\right)^3}{\pi\left(\frac{d}{2}\right)^2 t_b} = \frac{2}{3}\frac{d}{t_b} \qquad (5)$$

is set equal to the total volume flux, $\dot{V}$, of gas from the surface :

$$\dot{V} = \frac{i\nu}{nF} \qquad (6)$$

Here, ν is the molar volume of the gas. The following equation for t_b results :

$$t_b = \frac{2nFd}{3\nu i} \qquad (7)$$

Equation (7) is inserted into equation (4) to give :

$$C_o = C_\infty + 0.614\left(\frac{di}{nFDv}\right)^{\frac{1}{2}} \quad (8)$$

The presence of bubbles on the surface effectively increases the current density by screening a fraction of the electrode area[6]. When the surface coverage, θ, is taken into account, the following equation is obtained:

$$C_o = C_\infty + 0.614\left(\frac{di}{nFDv(1-\theta)}\right)^{\frac{1}{2}} \quad (9)$$

The equation reported by Ibl differs from equation (9) by the value of the constant (Ibl obtained 0.723) and by the fact that C_∞ has not been set to zero. Equation (9) indicates that the gas concentration at the electrode increases with the square root of the applied current density and that it also depends on the bubble size, the diffusion coefficient, and the fractional surface coverage.

The implicit assumptions made in the derivation are that bubbles in close proximity do not interfere with each other and that the surface is uniformly accessible for bubble nucleation. If the surface is not uniformly accessible (i.e., if there are a limited number of nucleation sites) or if the electrolyte which replaces the departing bubbles has a concentration which exceeds C_∞, then the values of C_o will exceed those predicted by equation (9).

Hydrogen supersaturation calculated with equation (9) is shown in figure 10-2 with an average bubble diameter of 50 μm, a fractional surface coverage of 0.15[7], and a diffusion coefficient of 4.7×10^{-5} cm^2/s. The predicted dependence of supersaturation on current density agrees qualitatively with the dependence observed in

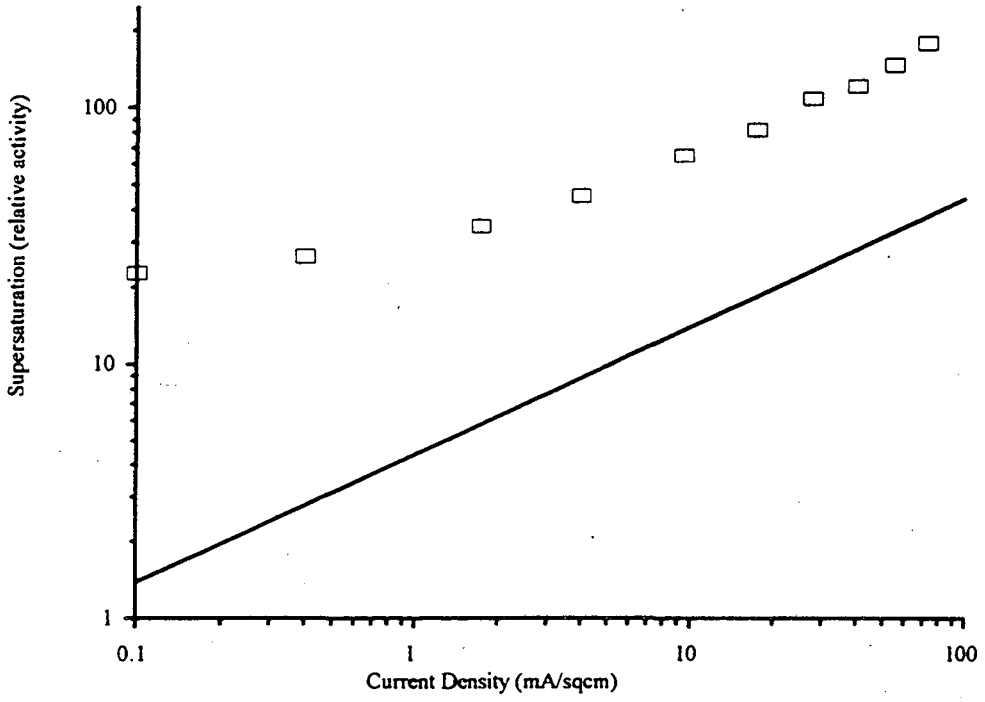

Figure 10-2. Surface renewal model. Experimental results using concentration overpotential technique (□) are compared to equation (9) (solid line).

the experiments. However, the model consistently predicts a lower supersaturation than those measured experimentally.

One of the assumptions in the model is that the bubbles have an equal likelihood of forming at any point on the electrode surface. This assumption permits the use of the relatively simple expression for one dimensional diffusion given as equation (2) and the equal distribution of the total flux to each nucleation site implied by the equality of equations (5) and (6). When only certain areas of the electrode are active for bubble nucleation, the average gas diffusion path length is greater than assumed in the model and the average gas concentration at the electrode would be higher. The data in figure 10-2 were obtained with a highly polished electrode and probably not uniformly accessible, consequently, higher supersaturation is expected than predicted by the model, in

agreement with the trend in figure 10-2. Higher nucleation densities are observed at higher currents[7,8] which could explain the smaller difference between the theoretical and experimental results at increasing current density in figure 10-2.

Modified surface renewal model - The fractional coverage of the surface and the average bubble size were assumed to be constant in the derivation of equation (9). In fact, both have been found to increase at high currents. A high fractional coverage increases the supersaturation predicted by the model by increasing the current density. Larger bubbles would increase supersaturation by increasing the average bubble formation time (t_b). Using the surface-coverage data of Venczel[9] and the bubble sizes reported by Janssen and Hoogland[10], the surface renewal model was modified and the results are shown in figure 10-3. At low current densities, the fractional coverage is less and the average bubble size is less than the results from equation (9) in figure 10-3. The net effect is to lower supersaturation predictions. At high current densities, both the bubble size and fractional coverage increase, leading to higher predicted supersaturations. However, neither of these changes improve the fit of the model. Accordingly, variable surface coverage and bubble sizes will not be considered further.

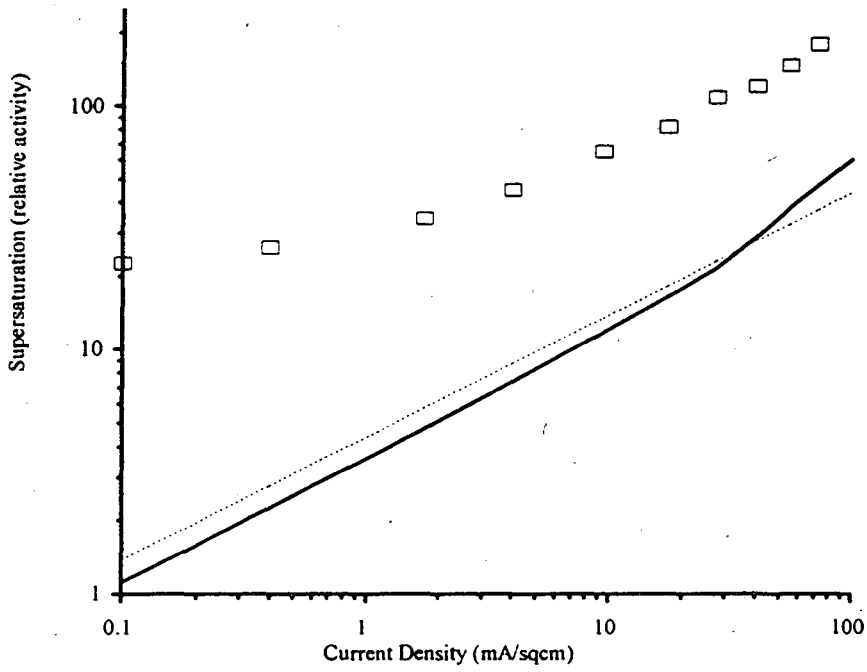

Figure 10-3. Modified surface renewal model. The surface coverage data of Venczel and the bubble size data of Janssen and Hoogland have been incorporated into equation (9) to produce the solid line. Also shown are the experimental data (□) and equation (9) (dashed line).

Impact of bubble departure on gas concentration profile - To address the overall fit of the model to the data, the basis of the model should be further examined. A major assumption of the model is that the bubbles that detach from the surface are replaced by electrolyte containing dissolved gas with a concentration equal to that of the bulk electrolyte. If, instead, supersaturated electrolyte replaces the departing bubbles, the diffusion driving force is reduced, mass transfer is reduced, and the experimental results would lie above the supersaturations predicted by the surface-renewal model. In the following analysis, the momentum and the overall and species continuity equations were solved numerically for the situation of a bubble rising through a liquid near a solid surface. The results provide a qualitative characterization of the impact of bubble detachment on

the concentration field of a species dissolved in the liquid.

The equations solved were

$$\rho\left(\frac{\partial v_r}{\partial t} + v_r\frac{\partial v_r}{\partial r} + v_z\frac{\partial v_r}{\partial z}\right) = -\frac{\partial p}{\partial r} + \mu\left[\frac{\partial}{\partial r}\left(\frac{1}{r}\frac{\partial}{\partial r}(r v_r)\right) + \frac{\partial^2 v_r}{\partial z^2}\right] \quad \textbf{(10)}$$

$$\rho\left(\frac{\partial v_z}{\partial t} + v_r\frac{\partial v_z}{\partial r} + v_z\frac{\partial v_z}{\partial z}\right) = -\frac{\partial p}{\partial z} + \mu\left[\frac{1}{r}\frac{\partial}{\partial r}\left(r\frac{\partial v_z}{\partial r}\right) + \frac{\partial^2 v_z}{\partial z^2}\right] + \rho g_z \quad \textbf{(11)}$$

$$\frac{1}{r}\frac{\partial}{\partial r}(r v_r) + \frac{\partial}{\partial z}(v_z) = 0 \quad \textbf{(12)}$$

$$\frac{\partial c_A}{\partial t} + v_r\frac{\partial c_A}{\partial r} + v_z\frac{\partial c_A}{\partial z} = D_{AB}\left[\frac{1}{r}\frac{\partial}{\partial r}\left(r\frac{\partial c_A}{\partial r}\right) + \frac{\partial^2 c_A}{\partial z^2}\right] \quad \textbf{(13)}$$

where
- t ≡ time
- r ≡ radial coordinate
- z ≡ axial coordinate
- R ≡ resultant bubble radius
- v_r ≡ radial velocity
- v_z ≡ axial velocity
- p ≡ pressure
- c_A ≡ concentration of species A in liquid B
- ρ ≡ density
- D_{AB} ≡ diffusion coefficient of species A in liquid B
- g_z ≡ gravitational vector

These equations, which are statements of the conservation of momentum and mass, apply to both the liquid and gas phases. However, gas phase contributions are assumed to be negligible. Axial symmetry and constant properties have been assumed. At the free surface, the boundary conditions are:

$$p - 2\mu\frac{\partial v_n}{\partial n} = 2H\sigma \quad \textbf{(14)}$$

$$\frac{\partial v_T}{\partial n} + \frac{\partial v_n}{\partial T} = 0 \qquad (15)$$

where $n \equiv$ vector normal to surface
$T \equiv$ vector tangential to surface
$v_n \equiv$ normal velocity
$v_T \equiv$ tangential velocity
$H \equiv$ mean surface curvature

Equation (14), the Young-Laplace equation, is a stress balance normal to the interface. Equation (15) states that the interface supports no tangential stress. No slip is specified at the solid surface and all velocities are initially zero.

Measurements by Bon (see figure 8-1) demonstrated that the steady-state concentration of dissolved hydrogen in the vicinity of a hydrogen evolving electrode decreases exponentially with distance from the electrode. The following equation, based on data from Bon, is an estimate of the concentration profile produced by a current density of 1 mA/cm^2 :

$$C^*(x) = \exp(-1.5x^*) \qquad (16)$$

where $C^* \equiv$ dimensionless concentration and
$x^* \equiv$ dimensionless distance from electrode.

The dimensionless concentration ranges from a value of 1 at the electrode surface (x = 0) to 0 far from the surface. A dimensionless distance of 1 corresponds to an average hydrogen bubble diameter of 50 μm. The dissolved gas concentration also decreases as a function of the distance from the bubble because of diffusion. Based on the results of Dukovic[11] the dimensionless concentration profile surrounding a bubble with a diameter of 1 unit is approximated as

$$C^*(r) = 1-\exp\left[-9\left(r^*-0.5\right)\right] \qquad (17)$$

where r is the dimensionless radial distance from the center of the bubble. Equations (16) and (17) were combined to specify the arbitrary but plausible initial concentration field shown in figure 10-4. Figure 10-4 is a cross section of a gas bubble submerged in a liquid near a solid surface. The bubble is located slightly above the surface. The gravitational vector is oriented vertically pointing downward.

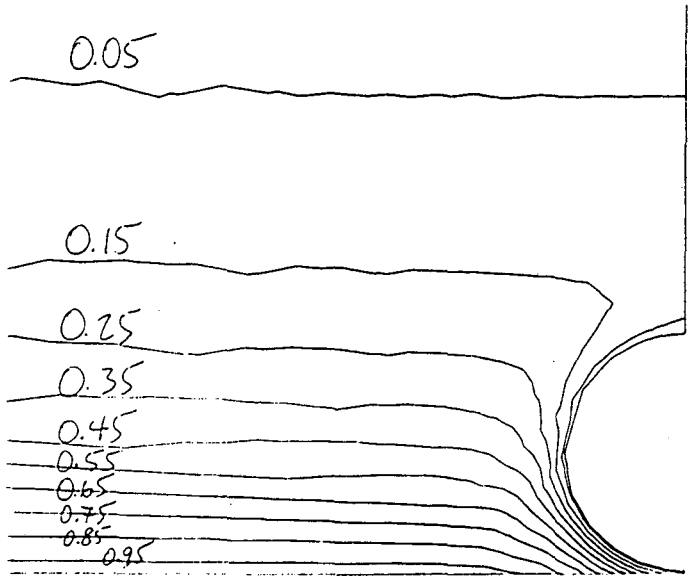

Figure 10-4. Initial concentration field around a bubble near a solid surface. The right border represents an axis of symmetry, the lower border represents the surface. Lines of constant dimensionless concentration are shown.

Equations (10) through (15) were solved with FIDAP version 7.52, which is a general-purpose finite element program by Fluid Dynamics International[12]. The program was run on a Hewlett Packard Model 715 work station with an HP-UX version 9.03

operating system. A user-supplied input file specifies the equations to be solved, the boundary conditions, the solution technique, and how the domain is to be meshed. The initial concentration field was specified with a user-supplied subroutine. The input file and subroutine are presented in Appendix III. The meshed problem domain is shown in figure 10-5. The intersection points of the lines in figure 10-5 are node points for the finite element algorithm. To solve free surface problems, FIDAP uses a deforming spatial mesh. Nodes originally located on boundaries stay on boundaries. Mesh lines perpendicular to the surface shorten or lengthen to accommodate the motion of the surface. Nodes located on the perpendicular lines move along the lines.

The simulation of bubble departure was carried out on a 50-μm bubble in a 1.07 cSt, 73.5 dyne/cm liquid. A species diffusivity of 1.0×10^{-5} cm^2/s was used. These conditions

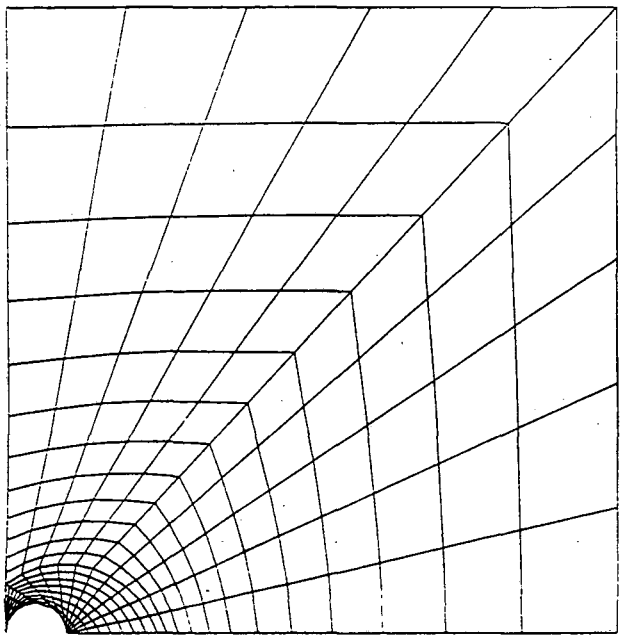

Figure 10-5. Full problem domain. The right border is the axis of symmetry, the left, top and bottom borders represent solid surfaces.

are typical for hydrogen evolved in 1M H_2SO_4. Length, time, and mass were scaled in the problem specification such that the surface tension, liquid density, and unit length used in the problem were unity. This scaling was done to minimize round-off errors. All boundaries were specified to be zero flux boundaries.

The results of the simulation are shown as a series of frames in figure 10-6. Movement of the bubble away from the solid surface alters the concentration profile in the region beneath the bubble. The space left by a bubble when it departs from a surface is not filled by bulk concentration liquid as assumed in the surface renewal model. Rather, it is replaced by liquid with a dissolved gas concentration similar to the concentration in the liquid near the surface. The concentration contours at a radial distance of 1/4 of the bubble radius from the bubble or more do not change significantly during the simulation.

This simulation has shown that the departure of a single bubble does not substantially alter the concentration of dissolved gas at an electrode surface. As a result, the dissolved gas concentration at the electrode surface is higher than assumed in the surface renewal model. Incomplete renewal of the electrolyte could explain the difference between the predictions of the surface renewal model and the experimental data shown in figure 10-2.

Partial renewal - Equation (9) was modified to approximately account for the replacement of departing bubbles with supersaturated rather than saturated electrolyte by substituting an unspecified replacement concentration, C_{ss}, for the bulk electrolyte concentration, C_∞:

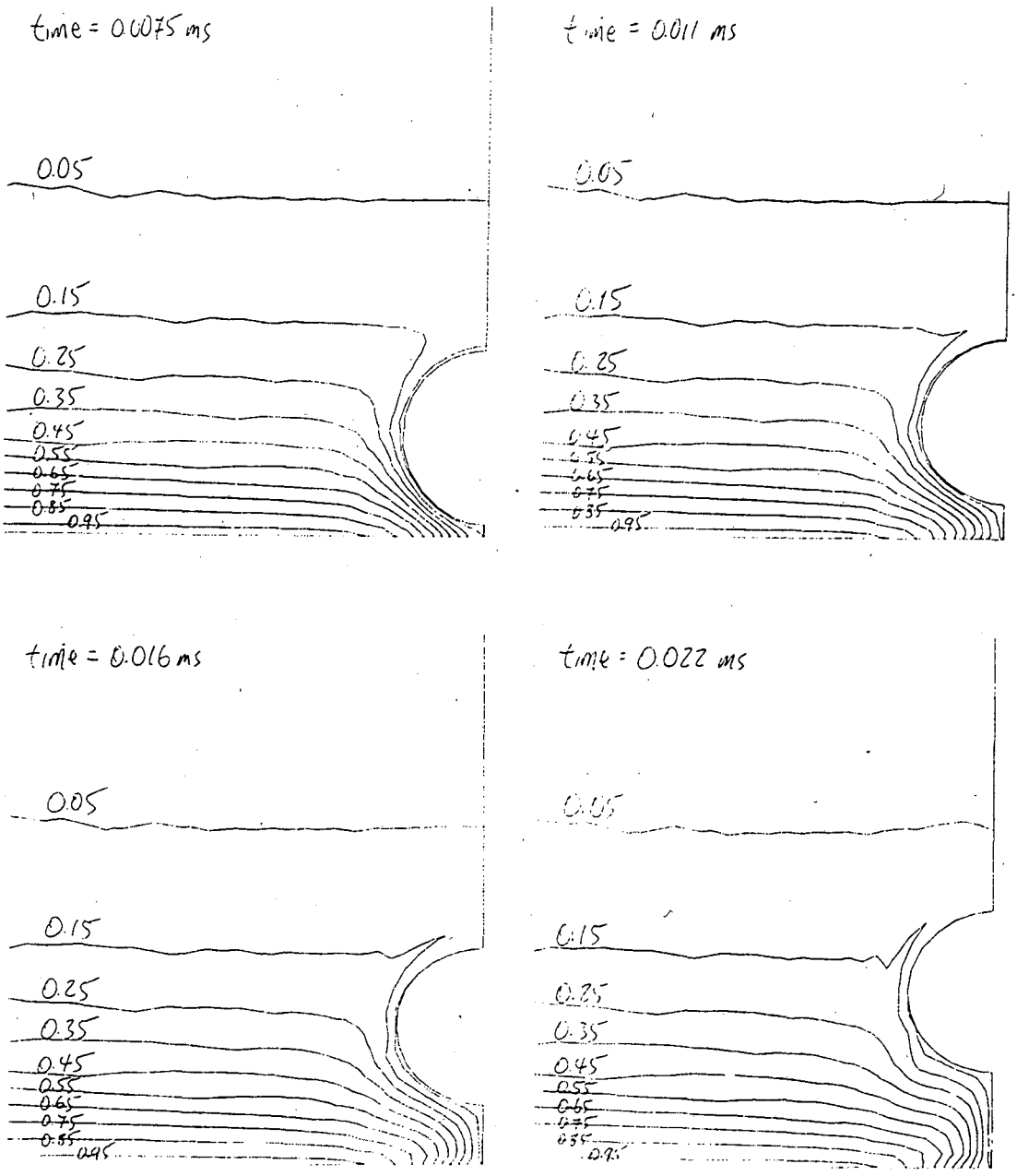

Figure 10-6. Simulation results: impact of bubble detachment on concentration field. The right border represents in each frame represents and axis of symmetry, the lower border represents a solid surface. Contours of constant concentration are shown around a 50-μm bubble departing from the surface. Contours more than 1/4 radius away from the bubble are not affected by the movement of the bubble.

$$C_o = C_{ss} + 0.614\left(\frac{d\,i}{nFD\nu(1-\theta)}\right)^{\frac{1}{2}} \qquad (18)$$

The replacement concentration, approximated as a fixed fraction of the measured supersaturation concentration, was treated as an adjustable parameter. Equation (18), which accounts for partial renewal of the electrolyte adjacent to the surface, is plotted with the experimentally measured supersaturation data in figure 10-7. A replacement concentration of 78% of the measured supersaturation concentration at each current density gave a good fit of equation (18) to the experimental results. Figure 10-7 shows that partial renewal of the electrolyte adjacent to the electrode could be the mechanism by which departing bubbles affect gas supersaturation at a gas-evolving electrode.

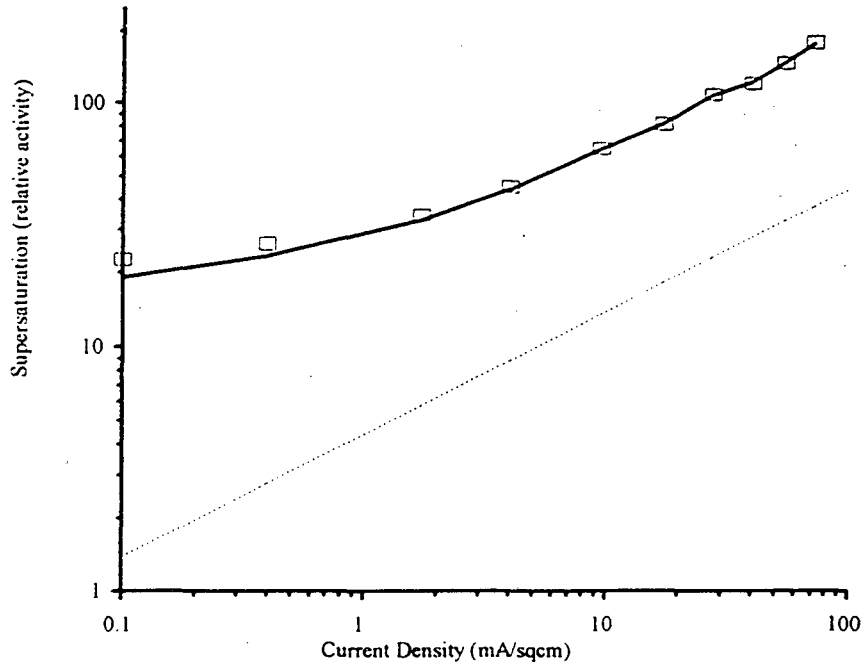

Figure 10-7. Partial renewal model. Experimental data (□) is shown with the surface renewal model of equation (9) (dashed line) and the partial renewal model of equation (18) (solid line). For the replacement concentration, a value of 78% of the measured supersaturation concentration was used to fit equation (18) to the experimental results.

References

1. Forest, T.W. and Ward C.A., *J. Chem. Phys.*, **66**, 2322 (1977).
2. Dapkus, K.V. and Sides, P.J., *J. Coll. Interface Sci.*, **111**, 133 (1986).
3. Ibl, N., *Chemic-Ingenieur-Technik*, **35**, 353 (1963).
4. Cottrell, F.G., *Z. Physik. Chem.*, **42**, 385 (1903).
5. Carslaw, H.S. and Jaeger, J.C., Conduction of Heat in Solids, Oxford, p.63 (1959).
6. Dukovic, J. and Tobias, C.W., *J. Electrochem. Soc.*, **134**, 331 (1987).
7. Venczel, J., Über den Stofftransport an Gasentwickelnden Elektroden. Diss. ETH Zürich (1961).
8. Westerheide, D.E. and Westwater, J.W., *A.I.Ch.E Journal*, 7, 357 (1961).
9. Venczel, J., *op.sit.*.
10. Janssen, L.J.J., and Hoogland, J.G., *Electrochimica Acta*, **15**, 1013 (1970).
11. Dukovic, J., *op.sit.*, p.331.
12. FIDAP is a trademark of Fluid Dynamics International, Inc. 500 Davis St., Suite 600, Evanston, IL, 60201 (U.S.A.).

Chapter 11. CONCLUSIONS

Hydrogen gas supersaturation at a smooth horizontal platinum electrode was measured by two independent means. Supersaturations ranged from relative activities of 26 to 178 as a function of applied current densities in the range of 0.4 to 72 mA/cm^2. The supersaturation values were consistently higher than those at a coarse electrode (rough surface) or at a vertically oriented non-recessed electrode. These results indicate that bubble nucleation and mass transfer in the bulk electrolyte are more restricted by the electrode texture, orientation, and geometry in the present work than those reported in other supersaturation experiments.

The presence of even a highly polished surface provides sites for bubble nucleation that lower gas supersaturation. Homogeneous electrolytic gas bubble nucleation does not occur because the necessary supersaturation levels are not achieved. Compared to the hypothetical limiting condition of mass transport by diffusion only, the supersaturation results were lower at high current densities, which indicate that bubble formation reduces supersaturation. However, higher supersaturations were measured at lower current densities than predicted for the limiting condition of no bubble formation, indicating that contaminants accumulate on the surface and may increase the effective current density.

Finally, a simulation showed that bubble departure does not reduce the dissolved gas concentration at an electrode surface to the extent assumed in the surface renewal model of Ibl. A proposed partial renewal model, which reflects the replacement of departing bubbles with supersaturated electrolyte, fits the experimental results.

APPENDIX III. FIDAP Input File

This is the user supplied input file and initial condition subroutine for the bubble departure simulation.

```
FI-GEN
/ Domain specification and mesh generation.
point(add, coor)
 0 0 0
 0.01 0 0
 1.01 0 0
 2.5 0 0
 10. 0 0
 10. 10. 0
 0 10. 0
 0 0.8 0
 0.51 0.5 0
 1.1 1.11 0
point(select, id)
 1
 2
 3
 4
 5
 6
 7
 8
 1
curve(add, line)
point(select, id)
 2
 9
 3
curve(add,arc)
point(sele,id)
 8
 10
 4
curve(add,arc)
point(sele,id)
 9
 8
curve(add,line)
```

```
curve(sele,id=9)
point(sele,id=9)
curve(spli)
/
curve(sele,id=1)
medge(add,lstf,inte=8,rati=0)
curve(sele,id)
 11
 3
medge(add,lstf,inte=8,rati=0)
curve(sele,id=12)
medge(add,lstf,inte=6,rati=2)
curve(sele,id=8)
medge(add,lstf,inte=6,rati=0.49)
curve(sele,id=13)
medge(add,lstf,inte=10,rati=0.02)
curve(sele,id=10)
medge(add,lstf,inte=10,rati=0)
curve(sele,id)
 6
 5
medge(add,lstf,inte=5,rati=0)
curve(sele,id=7)
medge(add,lstf,inte=12,rati=0.1)
curve(sele,id=4)
medge(add,lstf,inte=12,rati=10)
/
curve(sele,id)
 1
 8
 11
 12
mface(wire)
curve(sele,id)
 11
 10
 3
 13
mface(wire)
curve(sele,id)
 7
 6
 5
```

```
 4
 10
mface(wire,edg2=2)
mface(sele,id)
 1
 2
 3
mface(mesh,map,entity="water")
/
medge(sele,id=1)
medge(mesh,map,enti="sym1")
medge(sele,id)
 3
 11
medge(mesh,map,enti="sym2")
medge(sele,id)
 5
 10
 8
 9
medge(mesh,map,enti="vessel")
medge(sele,id)
 4
 6
medge(mesh,map,enti="surface")
end

FIPREP
/ Problem and solution technique specification
problem(axi-symmetric,free,nonlinear,transient,species=1)
PRESSURE(MIXE,discontinuous)
execution(newjob)
option(stress)
solution(q.n.=10)
print(none)
post(nblock=1)
1,90,1
time(dt=1.e-3,nsteps=28,trap,vari=0.004,tsta=0.,nofix=5)
/
surfacetension(set="1",const=1.)
viscosity(set="1",const=0.02224)
density(set="1",const=1.0)
diffusivity(const=2.21e-5)
```

```
bodyforce(const,fzc=-1.0,factor=1.323e-4)
entity(surface,name="surface",msurf="1",depth=13,ang1=90.,ang2=-90.)
entity(fluid,name="water",mvisc="1",mdens="1")
entity(plot,name="sym1")
entity(plot,name="sym2")
entity(plot,name="vessel")
icnode(spec=1,entity="water",subroutine)
bcnode(velocity,zero,enti="vessel")
bcnode(UY,zero,enti="sym1")
bcnode(UY,zero,enti="sym2")
end
create(fisolv)
end

      SUBROUTINE USRICI (NDF,X,Y,Z,NODE,VALI,CONS,NCONS,IERR)
C
C     USER SUPPLIED SUBROUTINE FOR THE DEFINITION OF BOUNDARY
NODAL VALUES
C     CALLED FROM FIPREP
C
C     INPUT:
C     =====
C     NDF    DEGREE OF FREEDOM
C     X      X COORDINATE
C     Y      Y COORDINATE
C     Z      Z COORDINATE
C     NODE   NODE NUMBER
C     CONS   USER SPECIFIED CONSTANTS
C     NCONS  NO. OF USER SPECIFIED CONSTANTS
C
C     OUTPUT:
C     ======
C     VALI   VALUE OF INITIAL CONDITION AT NODE (X,Y,Z)
      INCLUDE 'IMPLCT.COM'
      INCLUDE 'TAPES.COM'
      INCLUDE 'NUMBRS.COM'
      DIMENSION CONS(*)
      IERR = 0
      NDF = 5
      VALI = (1-exp(-9*(((x-.51)**2+y**2+z**2)**.5-.5)))*exp(-1.5*x)
      RETURN
C
      END
```

Ernest Orlando Lawrence Berkeley National Laboratory
One Cyclotron Road | Berkeley, California 94720

Prepared for the U.S. Department of Energy under Contract No. DE-AC03-76SF00098